Measurement of charm production in two-photon processes using inclusive lepton events at TRISTAN

Tsukasa Aso
Course of Fundamental Science and Technology
Graduate School of Science and Technology
Niigata University

March 24, 1996

Abstract

Measurements of open charm production in photon-photon collisions made with the AMY detector at TRISTAN are reported. We have analyzed the untagged hadronic events with final state leptons, $e^+e^- \rightarrow e^+e^-\ell^{\pm}X$, where neither of outgoing electron nor positron are detected. Charmed hadrons were identified by detecting the high momentum muons or electrons from their semileptonic decays. The data sample corresponds to an integrated luminosity of 275 pb^{-1} at an average center of mass energy of 58 GeV. Results are presented in the form of cross sections of inclusive leptons from charm for both muons and electrons.

The measured cross sections were compared with the theoretical predictions based on the direct and photon-gluon fusion processes, including the corrections for next-to-leading order QCD. The measured corss section is 1.8 standard deviations higher than the theoretical predictions, where the mass of charm quark is assumed to be 1.6 GeV/c^2. Theoretical predictions are examined in terms of the effects due to lighter mass of charm quark and harder fragmentation, and also compared with our measurements.

The measured inclusive electron corss section from charm has compared with the results of electron inclusive cross section given by TOPAZ. Our cross section is 30% smaller than that of TOPAZ, but consistent within one standard deviation.

Acknowledgements

This thesis is the result of the dedicated effort of all members of the collaboration and contribution of the talented engineering and technical staff. I would like to thank the TRISTAN staff for the excellent operation in running the accelerator and maintaining the storage ring, which provides the base for all the experiments done with the AMY detector.

I would like to thank Prof. K. Miyano for the guidance and encouragement.

I wish to express my deepest thanks to Prof. H. Miyata, my adviser, for providing an opportunity to work on this experiment and guiding me.

I am quite thankful to Dr. T. Sasaki, who providing me many technical supervision about software and two-photon physics.

I especially wish to thank to Prof. T. Nozaki, who has been giving suggestive advice to me and introduced two-photon physics to me.

Also, I wish to thanks Drs. B.J.Kim and R. Tanaka, who analyzed and developped a hadronic two photon analysis in AMY.

I wish to thanks Profs. K. Abe and Y. Sakai, they provide me continous encouragement about analysis and experiences of hardware.

I would like to thank Dr. L.Y.Zheng and Prof. C.Rosenfeld, for their support in maintenance of the triggers.

I woukd like to thank, Dr. S.K.Sahu, Messrs. D.Y.Kim, K.B.Lee, H.S.Ahn, D.K. Cho, and Y.S. Chung. I have enjoyed my stay in KEK with them.

I am gratefull to members of high energy physics laboratory in Niigata University: Miss N. Takashimizu, Mr. T. Ishizuka, Misses M. Shirai, H. Okazawa, N. Nakajima, M. Satou, Messrs. K. Sakurakichi, and S. Kenmochi.

I wish to thank Profs. S. Olsen and A. Maki and all members of AMY in the world, for their kindness and collaboration.

This work was only made possible with the support and love of my family and parents. I owe special thanls to my parents. They have always accepted my decisions and strongly supported me.

Contents

List of Tables

List of Figures

Chapter 1

Introduction

1.1 Physics Motivation

Cross section measurements of the pair production of charm quarks in untagged photon-photon collisions at PEP and PETRA experiments [1, 2] are higher than predictions based on the Born approximation for the direct quark-parton model (QPM) process $\gamma\gamma \rightarrow c\bar{c}$. Recently, the theoretical prediction has been improved by the inclusion of radiative QCD corrections and contributions from resolved photon processes [4]. ("Resolved photon interactions" are hard scattering processes involving the partonic structure of the photon, i.e. the quarks and gluons in the photon [5].) With these inclusions, the theoretical predictions are consistent with the latest experimental results for D^* production at PEP/PETRA [4].

More recently, the VENUS and TOPAZ experiments at TRISTAN have reported measurements of charm production in two-photon processes [6, 7, 8]. The TOPAZ results, using both inclusive electron events and D^* events, indicate an excess of charm at high transverse momentum, although both the TOPAZ and VENUS results at low transverse momentum are consistent with the predictions. In the Table 1.1, the summary of measurements analyzed by other experiments are shown from their publications. Figs. 1.1$\sim$ 1.3 show the results measured by experiments at TRISTAN as a function of transverse momentum of tagged particles. From Figs. 1.1$\sim$ 1.3, we see that the descripancy of measurements with theoretical predictions occurs at high transverse momentum (high-p_t) region. But the statistics is very poor at high-p_t region for all the experiments.

Theoretical predictions for charm production are less ambiguous than those for lighter quarks. Among the many different resolved photon processes that contribute to light quark production, only the photon-gluon fusion process gives a sizable contribution to charm production [4]. At TRISTAN energies, the contribution from twice-resolved photon processes to charm production are negligibly small. Moreover, vector meson dominance

Experiment	Tagged particle	E_{beam} (GeV)	Cross section (pb)	
			Measured	QPM LO (m_cGeV/c^2)
TPC/2γ[2]	$D^{*\pm}$	14.5	74±32	43(1.6)
JADE [3]	$D^{*\pm}$	17	(19±7.6ev.)	(3.4±11.4ev.)(1.5)
TASSO [1]	$D^{*\pm}$	17	97±29	40±3 (1.6)
TOPAZ [8]	$D^{*\pm}$	29	32±10.3	8.5(1.5)
TOPAZ [8]	π_{soft}	29	20.0±5.7	8.5(1.5)
TOPAZ [7]	$e^{\pm}$	29	19.3±3.4	5.8(1.5)
VENUS [6]	$e^{\pm}$	29	(68.4±12.7ev.)	(29.4±2.0ev.)(1.6)
ALEPH [9]	$D^{*\pm}$	45	155±39	100±20 (1.3-1.7)NLO

Table 1.1: Summary of results which are measured by other experiments. The theoretical predictions are shown only for the QPM prediction based on leading order (LO) calculation here, although TOPAZ, VENUS, and ALEPH have showed the expectation from resolved photon process. One must pay attention, in the comparison between measurements, since the covering region of mesurements are different.

processes (VMD) [10] are also negligible, and theoretical ambiguities associated with the phenomenological parameter P_t^{min} separating the soft and hard scattering processes do not occur. Furthermore, in the high transverse momentum region, the photon-gluon fusion process is largely suppressed and ambiguities relevant to the photon-gluon fusion process, such as the gluon density in the photon, are less important. Similarly, the uncertainty in the charm quark mass has a small effect on the predicted high transverse momentum cross section.

Here, we report a measurement of the cross section for open charm production in untagged two-photon collisions using the AMY detector at TRISTAN. The measurement of open charm production made at PEP/PETRA and TRISTAN mainly used the D^* reconstruction method. In this analysis, charmed quarks were identified by their semileptonic decay to high momentum muons or electrons. Almost all the charmed hadrons can decay finally in semileptonic modes directly or indirectly via one of $D^{\pm}$, D^0, $D_s^{\pm}$, and Λ_c. The average branching ratio for semileptonic decays is relatively large about 10%, where the production ratio of vector to psedoscalar charmed meson is 3:1, that 81% of these will be $c\bar{u}$ or $c\bar{d}$ rather than $c\bar{s}$, and 50% each neutral and charged meson production were assumed. This thesis is concerned with studies of open charm production in two-photon interactions using $e^+e^- \rightarrow e^+e^-\ell^{\pm}X$, where both of the outgoing beam electrons are scattered at very small angles and neither of them are detected in our detector.

We have analyzed a data sample corresponding to an integrated luminosity of 275 pb^{-1} and have observed more inclusive high momentum leptons than any of the other TRISTAN experiments. Our higher statistics indicate some excess over theoretical predictions at high

transverse momenta.

1.2 Thesis Overview

This thesis will present a measurement of charm production in two-photon processes using inclusive lepton events, $e^+e^- \rightarrow e^+e^-\ell^{\pm}X$, observed by the AMY detector at TRISTAN e^+e^- collider.

This thesis is organized as follows:

In Chapter 2, the theory of two photon processes will be described. The theoretical background and history will be reviewed briefly.

In Chapter 3, the TRISTAN accelerator and details of each component of the AMY detector are described.

In Chapter 4, the Monte Carlo programs we used will be also explained in detail.

In Chapter 5, the selection procedure of hadronic two photon events will be described.

In Chapter 6 and 7, the analysis of inclusive lepton events will be presented. The method of lepton identication and the estimation of backgrounds are described.

In Chapter 8, the inclusive lepton production cross section will be presented for both muon and electron.

In Chapter 9, Results of our measurement are discussed with the theoretical uncertainty and the comparison with TOPAZ measurements.

Finally, we summarize our analysis in Chapter 10.

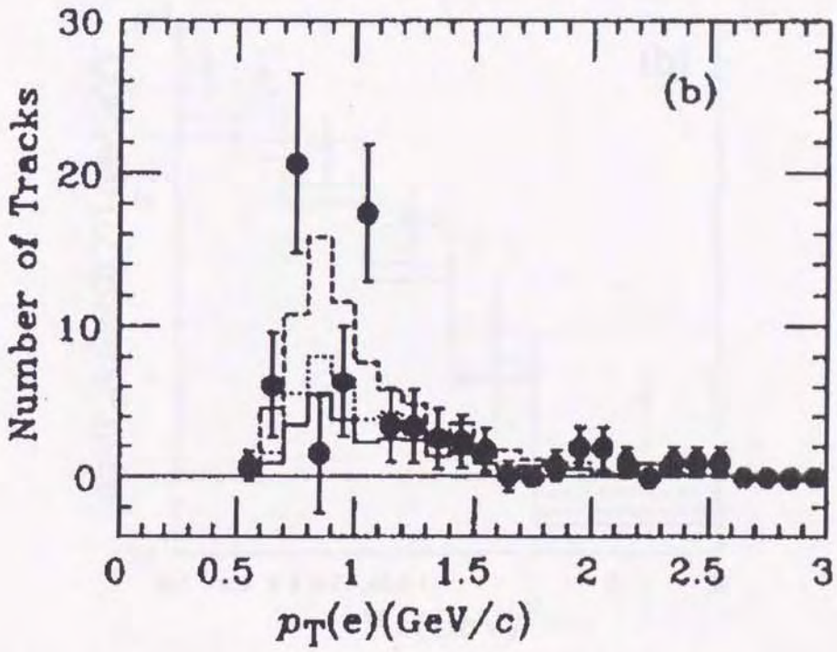

Figure 1.1: The result of inclusive electron events analyzed by VENUS group at TRISTAN. The closed cricle shows the experimental data. The solid and dashed lines show the direct and direct+resolved photon process with LAC1 parton density, where next-to-leading order (NLO) QCD corrections are included.

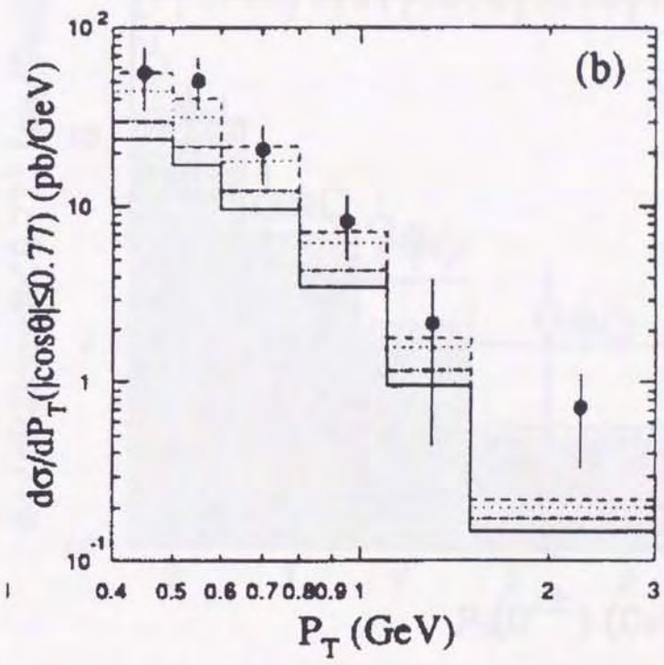

Figure 1.2: The result of inclusive electron events analyzed by TOPAZ group at TRISTAN. The closed circles show the experimental data. The solid and dotted lines are the direct and direct+resolved photon process with LAC1 parton density, where m_c =1.5 GeV/c^2 was taken. The dashed lines are direct+LAC1 with a m_c=1.3 GeV/c^2.

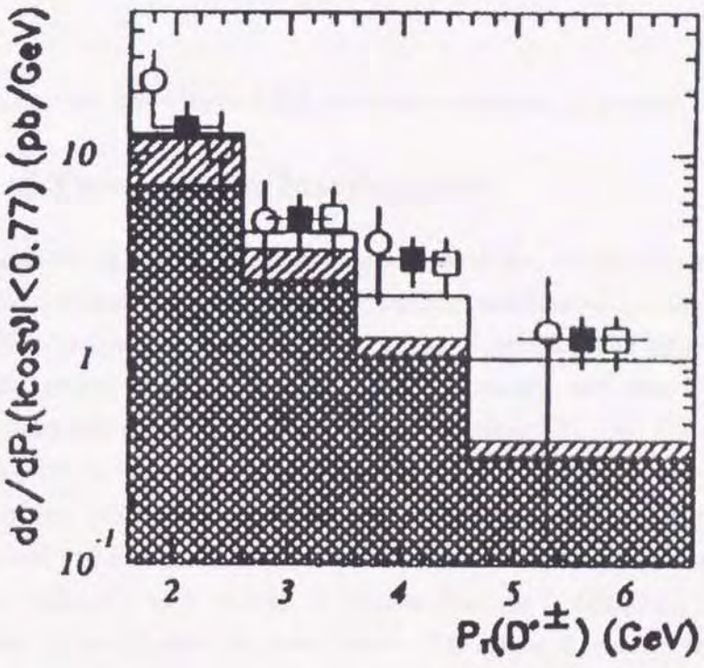

Figure 1.3: The result of $D^{*\pm}$ events analyzed by TOPAZ group at TRISTAN. The open circle and open square show the result from full reconstruction and soft pion analysis, respectively. The closed square shows the combined result of thoes two analysis. The cross-hatched area is the direct process, the singly-hatched area the resolved photon process (LAC1), and the open area $\tilde{t}$ pair production.

Chapter 2

Theory of Two-Photon Interactions

In this Chapter, current knowlege of the hadronic structure of photon is reviewed.

2.1 Bases of Two-Photon Interactions

The analysis of scattering reactions of elementary particles, particulary elastic and inelastic electron scattering had introduced us invaluable understandings about the structure of matter. Usually electron scattering is interpreted as probing the target by virtual photons. The photon is one of gauge bozons so that massless and structureless. However the uncertainty principle predictes that a photon of energy E_γ can fluctuate into pair of charged particles with the mass m_{pair} for a short period of time as shown in Fig. 2.1. Such intermediate state has lifetime $\Delta\, t \approx 2E_\gamma/m^2_{pair}$, where $\hbar = c = 1$ are used. Whenever the liftime of the virtual state exceeds about 10^{-25} s, a corresponding characteristic energy or momentum scale is about 1 GeV or less. It implies that the (virtual) $q\bar{q}$ pair has sufficient time to evolve into a complicated hadronic state. Therefore it is expected that the study of two-photon interacrtions will probe the structure of hadronic interactions.

A study of hadron production by photons opens ways for investigating a number of fundamental processes in strong interaction physics and also in QED. The importance of two-photon process hadron production in e^+e^- colliding beam experiments was first studied in 1969 [11]. The study of two-photon reactions in order to test the quark-parton model (QPM) through measurements of the photon structure function was suggested in Ref. [12]. Witten's observation [13] shows that the quark and gluon content of the photon is completely calculable in QCD under the ayamptotic limit of infinit Q^2. It pointed out that a measurement of the photon structure function F_2^γ will not just test QPM but will serve as an important roll to test QCD. The photon-photon interaction can be used to study both perturbative and non-perturbative aspects of strong interactions. In spite of

the higher order process $\alpha^4_{\rm QED}$, the two-photon channel of particle production is one of the main source for colliding e^+e^- beams. For example, the total cross section for dimuon production are shown in Fig. 2.2 as a function of center of mass energy $\sqrt{s}$ with that of annihilation process via virtual photon exchange (see also Appendix A). Recently, two-photon processes are considered to be one of the serious background at future linear colliders, so that the corresponding cross section should be estimated.

Electron colliding beams ($e^{\pm}e^-$) have been the main instrument for the study of the hadron production in two photon processes. The e^+e^- storage ring can provide enough energies and fluxes of photons since the electron goes into an electron photon state by the quantum fluctuation. In the Table 2.1, the some of the beam facilities used for studies of hadron production in two-photon processes are listed.

Facilities	PETRA (DESY)	PEP (SLAC)	TRISTAN (KEK)	LEP (CERN)	HERA (DESY)
Physics start date	1978	1980	1987	1989	1990
Physics end date	1986	1990	1995	–	–
Particle collided	e^+e^-	e^+e^-	e^+e^-	e^+e^-	e^-p
Maximum beam energy (GeV)	23.4	15	32	55	e^-: 26 p: 820
Luminosity ($10^{30}cm^{-2}s^{-1}$)	24 at 17.5 GeV	60	35	11	16
Circumference (km)	2.304	2.2	3.02	26.66	6.336

Table 2.1: Partial list of colliding beam facilities used for studies on hadronic interactions of photons.

There are three categolies in the photon-photon reactions. Those are interactions of a real and virtual photon ($\gamma\gamma^*$), of two real photons ($\gamma\gamma$), and of two virtual photons ($\gamma^*\gamma^*$). These categolies correspond to "single tagged", "untagged (anti-tagged)", and "double tagged" two photon events in the experiment. Scattered electrons are detected (or not detected positively) to ensure the vairtuality of the radiated photon. If an electron is detected at large angle, the virtuality of radiated photon is expected to be high. On the other hand, if scattered electron is not detected since it escape into the beam pipe, the radiated photon is expected as almost real. The word "tagged" is usually used to represent the conditions of scattered electrons in the experimental analysis of two-photon physics, and corresponds to the virtualities of photons. In this thesis, we have analyzed the two-photon processes with untag condition.

2.2 Kinematics

The basic diagram of the two photon reactions in the e^+e^- colliding facilities is shown in Fig. 2.3. The figure contains the kinematic symbols used later in this thesis.

The two incoming electrons and positrons radiate a photon at small angles. These two photons react and produce the final state X. In the general case, the amplitude for the reaction shown in Fig. 2.3 is written as;

$$T = \frac{e^2}{q_1^2 q_2^2} j_\mu j_\alpha R^{\mu\alpha}. \tag{2.1}$$

Here $j_{\mu,\alpha}$ is the electromagnetic current of the electrons. $R^{\mu\alpha}$ is connected to the $\gamma\gamma \rightarrow X$ helicity amplitude $R_{\lambda_1\lambda_2}$ via

$$R_{\lambda_1\lambda_2} = \varepsilon_\mu(\lambda_1)\varepsilon_\alpha(\lambda_2)R^{\mu\alpha} \ , \tag{2.2}$$

$\varepsilon_\mu(\lambda)$ is the polarization four vector of a photon that helicities are $\lambda(= -1, 0, +1)$. In the case of hadron production, $e^+e^- \rightarrow e^+e^-X$, the amplitude T has to be squared and integrated over all final states. The differentical cross section for two-photon production can be expressed in terms of the $R^{\mu\alpha}$ amplitudes as follows [14, 15],

$$d\sigma = \frac{(4\pi\alpha)^2}{q_1^2 q_2^2} \rho^{\mu\nu} \rho^{\alpha\beta} R^{*\nu\beta} R^{\mu\alpha} \frac{(2\pi)^4 \delta(q_1 + q_2 - Px) d\Gamma}{4\left\{(p_1 p_2)^2 - m_1^2 m_2^2\right\}^{1/2}} \frac{d^3p_1' d^3p_2'}{2E_1 2E_2 (2\pi)^6} \ , \tag{2.3}$$

where $d\Gamma$ stands for an interval of the Lorentz invariant phase space of the particle in the final state X. The matrix ρ_i refers to the vertex, and represents a density matrix for the virtual photon at the vertex. $Px = q_1 + q_2$ is the total momentum of the produced system with mass $W=\sqrt{q_1^2 + q_1^2}$.

The total cross section obtained from the integtation contains a hadronic tensor,

$$W^{\nu\beta\mu\alpha} = \frac{1}{2} \int R^{*\nu\beta} R^{\mu\alpha} (2\pi)^4 \delta(q_1 + q_2 - P_X) d\Gamma \tag{2.4}$$

$$= \sum_i I_i^{\nu\beta\mu\alpha} A_i \ , \tag{2.5}$$

where the tensors I_i are constructed from the vectors q_1, q_2 and the metric tensor $g_{\mu\nu}$. A_i is the "structure functions" or "generalized cross-sections" and have to be measured or calculated in a theory of strong interaction. They only depend on the photon masses q_i^2 and the invariant mass of the final state $W^2 = (q_1 + q_2)^2$.

Eq. 2.3 is a general expression of the differential cross section for hadron production. It is usually approximated by phenomenological expressions and equivalent photon approximation under the kinematical limitations.

As one of the examples, Budnev et al give the most intuitive interpretation of Eq. 2.3. It express the differential cross section in terms of the cross sections σ_{TT}, σ_{TL}, σ_{LT}, and σ_{LL} for hadron production by scattering of two-photons with the four combinations of transverse (T) and longitudinal (L) polarization. It is also convenient to separate the two-photon reaction into two pieces; 1) the generaion of the luminosity function $\mathcal{L}_{\gamma\gamma}$ for the scattering between the transverse photons coming from the clouds around the colliding electron and positron beams, and 2) the generation of final state from the photon-photon collisions. Then the cross section for the production of a state X is assumed to factorize [16],

$$\frac{d^6\sigma}{dv_1 \ldots dv_6} = \sum_{ij} \frac{d^6\mathcal{L}^{ij}_{\gamma\gamma}}{dv_1 \ldots dv_6} \sigma_{ij}(W^2, q_1^2, q_2^2) \ . \tag{2.6}$$

i,j represents a polarity of photons and σ_{ij} is the cross section for process $\gamma\gamma \rightarrow$X as Budnev's expression. $\mathcal{L}_{\gamma\gamma}$ is the luminosity function. Of cource interference terms are taken into consideration when the summamation is performed. If the beams are unpolarized and fixed, the quantities are expressed in terms of six basic variables, for example: energy and polar angle of scattering leptons θ_i, E'_i, azimuthal angle betwen the two scattering leptons φ, and the azimuthal angle of one of scattered leptons ϕ.

In the case of real $\gamma\gamma$ collisions, namely under the condition q_1^2, $q_2^2 \rightarrow 0$, so photons are only transeversaly polarized, Eq. 2.6 become simple by dropping off the term relevant to longitudinal photons,

$$\frac{d^6\sigma}{dv_1 \ldots dv_6} = \frac{d^6\mathcal{L}_{\gamma\gamma}}{dv_1 \ldots dv_6} \sigma_{\gamma\gamma}(W^2, q_1^2, q_2^2) \ , \tag{2.7}$$

where $\sigma_{\gamma\gamma} = \sigma_{TT}$ and the luminosity function is given by [16],

$$\begin{aligned} \frac{d^5\sigma}{dydzd\theta_1 d\theta_2 \varphi} &= \frac{\alpha_2}{32\pi} \xi \cot\frac{\theta_1}{2} \cot\frac{\theta_2}{2} \\ &\times \left\{ \frac{K - 2(z + Q^2_{n,2})}{\xi^2} + 1 - \frac{4m_e^2}{sQ^2_{n,2}} \right\} \\ &\times \left\{ \frac{K - 2(y + Q^2_{n,1})}{\xi^2} + 1 - \frac{4m_e^2}{sQ^2_{n,1}} \right\} \ , \end{aligned} \tag{2.8}$$

where

$$K = u^2 + Q^2_{n,1} + Q^2_{n,2} \tag{2.9}$$

$$\xi^2 = K^2 - 4Q^2_{n,1}Q^2_{n,2} \ . \tag{2.10}$$

Here y and z are energies of two photons divided by $\sqrt{s}/2$. $Q^2_{n,i}$ is defined as Q^2_i/s and are scaled invariant mass squared of each of the two interacting photons. The variable $u = W_{\gamma\gamma}/\sqrt{s}$ is scaled invariant mass of the $\gamma\gamma$ system.

2.3 Property of Photon

There are three different two-photon processes for hadron production. Those are 1) vector-meson-dominance, 2) direct-partonic, and 3) resolved photon processes.

2.3.1 Vector Meson Dominance Model

For low photon energies, the hadronic properties of the photon can be explained by the vector meson dominance model, in which the photon is converted into one of the low-lying vector mesons that scatters diffractively (Fig. 2.5). The resultant transverse momentum distribution are limited and shows $\sim e^{-Ap_T}$ dependence. The total cross section for $\gamma\gamma \to V_1V_2 \to X$ is simply given by

$$\sigma(\gamma\gamma \to V_1V_2 \to X) = \frac{2\alpha^2}{(f_1^2/4\pi)(f_2^2/4\pi)}\sigma(V_1V_2 \to X) \tag{2.11}$$

where $f_i(i = 1, 2)$ is the vector meson dominance coupling constant for V_i, and $\sigma(V_1V_2 \to X)$ is the total cross section for $V_1V_2 \to X$.

The Q^2 dependence is given by the fully factorizing form

$$\sigma_{\gamma\gamma}(W^2, Q_1^2, Q_2^2) = \sigma_{\gamma\gamma}(W) \cdot F_\rho(Q_1^2) \cdot F_\rho(Q_2^2) \tag{2.12}$$

with

$$F_\rho(Q^2) = \frac{m_\rho^2}{m_\rho^2 + Q^2} \,. \tag{2.13}$$

Here only the dominant part ρ is used.

The most elaborate version of the VDM has been worked out by Sakurai and Schildknecht [17], which is known as the generalized vector meson dominance model (GVDM). The form factor includes the sum over the mesons ρ, ω, ϕ, and the higher resonances and the continuum are approximated by a pole term $\sim (1 + Q^2/m_0^2)^{-1}$,

$$F(Q^2) = \sum_{\rho,\omega,\phi} r_V \left(\frac{m_V^2}{Q^2 + m_V^2}\right)^2 + 0.22\frac{m_0^2}{Q^2 + m_0^2} \,, \tag{2.14}$$

where $m_0 = 1.4$ GeV/c^2. The r_V are given by 0.65, 0.08, and 0.05 for ρ, ω, and ϕ, respectively.

TPC/Two-Gamma group [18] modified the factorization of form factor as

$$F(Q^2) = \sum_{\rho,\omega,\phi} \frac{r_V}{0.78 \cdot \left(1 + \frac{Q^2}{m_V^2}\right)^2} , \tag{2.15}$$

in order to avoid double counting between GVMD and QPM.

The term $\sigma_{\gamma\gamma}(W)$ was estimated by Regge model to be

$$\sigma_{\gamma\gamma}(W) = 240 + \frac{270}{W(\mathrm{GeV}/c^2)}(\mathrm{nb}) . \tag{2.16}$$

2.3.2 Quark Parton Model

In the direct process, two photons directly produce a pair of quark and antiquark (Fig. 2.6), which in turn hadronize. As a result, the entire energy of both photons goes into the hard subprocess, and produce high p_T jets in the final state. The total cross section for $\gamma\gamma \to q\bar{q}$ at the total center of mass energy squared of $s_{\gamma\gamma}$ is simply given, to the zeroth order of strong interactions, by [19]

$$\sigma(\gamma\gamma \to q\bar{q}) = \frac{12\pi\alpha^2 e_q^4}{s_{\gamma\gamma}} \left[\left(1 + r - \frac{1}{2}r^2\right) \ln\left(\frac{1+\beta}{1-\beta}\right) - \beta(1+r)\right] \tag{2.17}$$

where α is the fine structure constant, e_q and m_q are the quark charge and mass, respectively, and $r = 4m_q^2/s_{\gamma\gamma}$ and $\beta = (1-r)^{1/2}$ which is the velocity of the quark. The p_T distribution in QPM process is a relatively flatter than VMD's. It shows the p_T^{-4} dependence characteristic for high-p_T jet production.

2.3.3 Resolved Photon Processes

In the single-resolved-photon process, either one of the quark and antiquark produced by the one resolved photon is scattered by the other photon. Subsequently, the produced quark and antiquark (and gluons) hadronize (Fig. 2.7). In the double-resolved photon process, either one of the quark and antiquark (and gluons) produced by the one resolved photon is scattered by either one of the quark and antiquark (and gluons) produced by the other resolved photon, due to the exhange of gluons (Fig. 2.8). Since the parton distribution function in the photon are $\mathcal{O}(\alpha/\alpha_s)$, contributions of resolved photon processes are the same order of the direct process in coupling constants.

The total cross section for jet production by photon-photon reactions in e^+e^- colliders is given by using the Weizsäcker-Williams approximation,

$$\begin{aligned}\frac{d\sigma(jj)}{dp_T} &= 2p_T \int_{4p_T^2/s}^1 dx_1 f_{\gamma/e}(x_1) \int_{4p_T^2/x_1 s}^1 dx_2 f_{\gamma/e}(x_2) \\ &\times \int_{4p_T^2/x_1 x_2 s}^1 dx_3 q_i^\gamma(x_3) \int_{4p_T^2/x_1 x_2 x_3 s}^1 dx_4 q_j^\gamma(x_4) \\ &\times \frac{d\hat{\sigma}_{i,j\to k,l}(\hat{s},\hat{t},\hat{u})}{dp_T^2} ,\end{aligned} \tag{2.18}$$

where p_T denotes the transverse momentum of the jets, and $\hat{s} = x_1x_2x_3x_4s$ is the squared invariant mass going into hard scattering subprocesses that are described by the cross section $\hat{\sigma}$. $f_{\gamma/e}(x_i)$ terms are the photon flux factors and q_i^γ are the parton densities inside the photon. The photon flux factor $f_{\gamma/e}$ is given by [15]

$$f_{\gamma/e}(z) = \frac{\alpha}{\pi z}\left[\left\{1+(1-z)^2\right\}\ln\left(\frac{2E(1-z)}{m_e z}\sin\frac{\theta_{max}}{2}\right) - 1 + z\right] \tag{2.19}$$

where E is the beam energy. Eq. 2.19 is the same as the single tag photon flux factor.

In other expression, the differential cross section is give in terms of rapidity distribution. This is because the rapidity distribution is strictly related to the parton densities at fixed x value. For the case of resolved photon process, it is given by [20],

$$\frac{d^3\sigma(jj)}{dp_T d\eta_1 d\eta_2} = 2p_T y_m z_m \sum_{i,j,k,l} f_{i/e}(y_m) f_{j/e}(z_m) \frac{d\hat{\sigma}_{i,j\to k,l}}{d\hat{t}}(\hat{s},\hat{t},\hat{u}) \tag{2.20}$$

$$\begin{aligned}&= 2p_T y_m z_m \int_{y_m}^1 \frac{dy}{y} f_{\gamma/e}(y) q_i^\gamma\left(\frac{y_m}{y}\right) \int_{z_m}^1 \frac{dz}{z} f_{\gamma/e}(z) q_j^\gamma\left(\frac{z_m}{z}\right) \\ &\times \frac{d\hat{\sigma}_{i,j\to k,l}}{d\hat{t}}(\hat{s},\hat{t},\hat{u}) ,\end{aligned} \tag{2.21}$$

where

$$y_m = \frac{1}{2}x_T(e^{\eta_1} + e^{\eta_2}) \tag{2.22}$$

$$z_m = \frac{1}{2}x_T(e^{-\eta_1} + e^{-\eta_2}) \tag{2.23}$$

with (2.24)

$$x_T = \frac{2\sqrt{p_T^2 + m_q^2}}{\sqrt{s}} \tag{2.25}$$

$$\hat{s} = y_m z_m s \tag{2.26}$$

$$\hat{t} = \frac{\hat{s}}{2}\left(\frac{2m_q^2}{\hat{s}} - 1 \pm \sqrt{1 - \frac{4(p_T^2 + m_q^2)}{\hat{s}}}\right) . \quad (2.27)$$

η_1 and η_2 are rapidities of two high p_T jets, $\hat{s}$, $\hat{t}$, and $\hat{u}$ are Mandelstam variables in the hard scattering subprocesses. if $i = j = \gamma$, then the formula Eq. 2.21 shows direct contribution. The cross sections of subprocesses are given in Appendix B.

2.4 Heavy Flavour Production

As discussed in the Section 1.1, the production of heavy quarks has two theoretical advantages than the production of light quarks,

1) The large mass ($m_c \gg \Lambda_{QCD}$) makes QCD perturbation theory applicable in all of phase space.

2) Contributing diagrams are only the direct and photon-gluon fusion processes at the TRISTAN energies.

The leading-order cross-section is obtained exactly from the calculation, but there are uncertainties in the higher order corrections and in the value of m_c to be used.

Drees et al. has included full next-to-leading order QCD (NLO QCD) corrections to leading-order diagrams. Fig. 2.9(a)-(c) are diagrams of the Born term direct process and its NLO QCD corrections. Fig. 2.9(d)-(f) depicted diagrams of the photon-gluon fusion processes and its NLO QCD corrections. The largest part of the resolved photon process is given by the photon-gluon fusion process, and the other diagrams are negligible at TRISTAN energy.

The total cross section for direct process, including virtual and soft gluon corrections and a hard gluon radiation is [4]:

$$\sigma_{\text{direct}}\left(\gamma\gamma \to Q\bar{Q}(g)\right) = \frac{4\pi\alpha^2 e_Q^4 N_c}{s_{\gamma\gamma}}\beta\left\{1 + \frac{4\alpha_s}{3\pi}\left[\frac{\pi^2}{2\beta} - \left(5 - \frac{\pi^2}{4}\right) + \mathcal{O}(\beta)\right]\right\} \quad (2.28)$$

$$= \frac{\alpha^2 e_Q^4}{m_Q^2}\left(c_{\gamma\gamma}^{(0)} + 4\pi\alpha_s c_{\gamma\gamma}^{(1)}\right) \quad (2.29)$$

where $s_{\gamma\gamma}$ denotes the total $\gamma\gamma$ energy squared and $\beta = (1 - 4m_Q^2/s_{\gamma\gamma})^{1/2}$ is the velocity of the quark. Here $c_{\gamma\gamma}^{(0)}$ describes the Born level (QPM) prediction, while $c_{\gamma\gamma}^{(1)}$ introduces an effect of NLO QCD corrections. $c_{\gamma\gamma}^{(0)}$ and $c_{\gamma\gamma}^{(1)}$ depend on $r = s_{\gamma\gamma}/4m_Q^2 - 1$ as shown in Fig. 2.10. The corrections for direct process are very large and positive close to threshold

of the invariant mass, because of the Coulomb singularity, and dominated by soft gluon exchange diagram. The K factor for QCD correction is given by

$$K(r) = \frac{\sigma\left(\gamma\gamma \to Q\bar{Q}(g)\right)}{\sigma_0\left(\gamma\gamma \to Q\bar{Q}(g)\right)} \tag{2.30}$$

$$= \frac{c_{\gamma\gamma}^{(0)} + 4\pi\alpha_s c_{\gamma\gamma}^{(1)}}{c_{\gamma\gamma}^{(0)}} = 1 + 4\pi\alpha_s \frac{c_{\gamma\gamma}^{(1)}}{c_{\gamma\gamma}^{(0)}} . \tag{2.31}$$

The corrections for the resolved photon process are gluon emission from the initial state such as g→gg or q→gq. The dominated contribution come from $\gamma q \to c\bar{c}q$ process (Fig. 2.9(f)), where q is a light quark (u, d, s). Gluon emission from the initial state is partly included in the leading order contribution such as momentum scale dependence of the gluon density. LO gluon density usually assigns zero transverse momentum to the partons in the initial state. However the gluon emission in γq process can provide nonzero transverse momentum to the $c\bar{c}$ system. As a result, the distribution of transverse momentum for the charm quark becomes harder than LO one. Therefore the correction for including $\gamma q \to c\bar{c}q$ process is given in the form of depending on the transverse momentum of charm quark. It is given by the function $K(p_T^c)$ [8, 21] in a good approximation

$$K(p_T^c) = \left(\frac{d\sigma^{NLO}}{dp_T^c}\right) / \left(\frac{d\sigma^{LO}}{dp_T^c}\right) \tag{2.32}$$

$$= N \cdot (0.48 p_T^c + 0.52). \tag{2.33}$$

p_T^c is the transverse momentum of the charm quark in GeV/c and N is the normalization factor that is determined to be from fits of the NLO cross section for the resolved photon process to maintain the continuous connection to the low transverse momentum region. The integration of the cross section ratio $K(p_T^c)$ of NLO to LO in the range $p_T^c \geq 1.2$ GeV/c is 1.55. Here, the charm quark mass(m_c) and the renormalization scale(μ) are taken as 1.6 GeV/c^2 and $\sqrt{2}m_c$, respectively. Eq. 2.33 is only valid in the transverse momentum region beyond 1.2 GeV/c. For the low transverse momentum region, NLO QCD corrections are very complicated due to Coulomb corrections, soft gluon exchange between the initial gluon and final quark, and final state gluon emission. If the all transverse momentum regions are taken into account, K should be 1.12. In the whole discussion, $W_{\gamma\gamma} \geq 2m_{D^*} =$ 4 GeV/c^2 was imposed. The formulae for low transverse momentum region are shown in Appendix C.

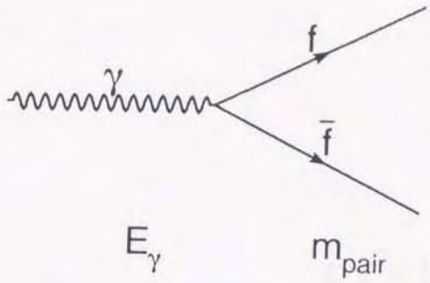

Figure 2.1: Quantum fluctuation of a photon into pair of charged particles.

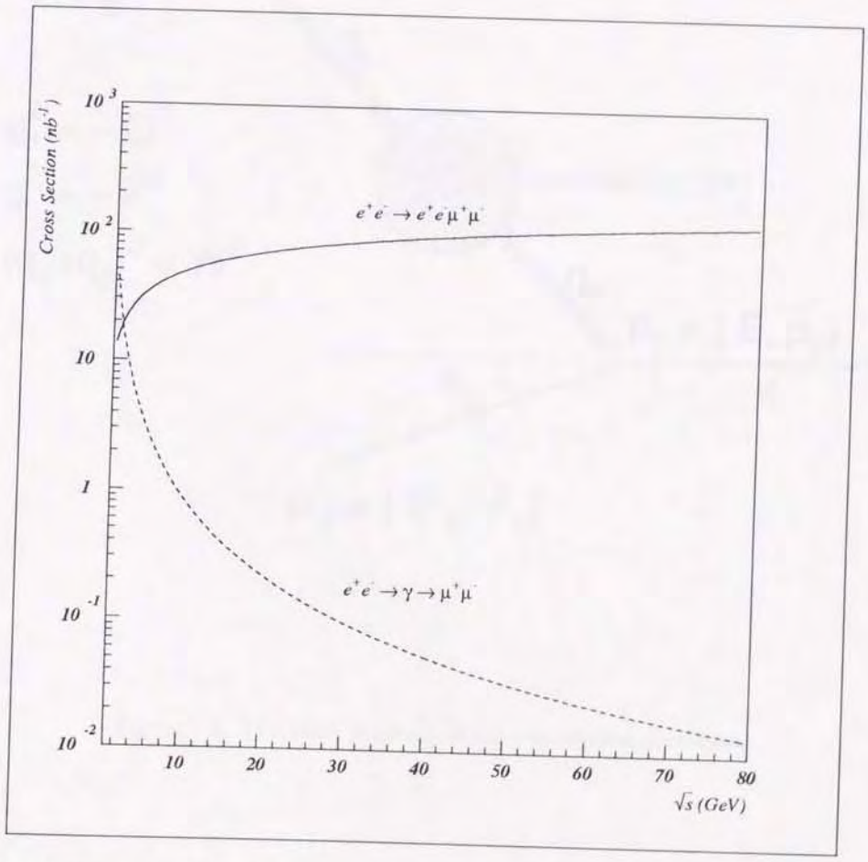

Figure 2.2: Total cross sections for the process $e^+e^- \rightarrow \mu^+\mu^-$ and $e^+e^- \rightarrow e^+e^-\mu^+\mu^-$ as a function of the centre-of-mass energy of an electron-positron collider.

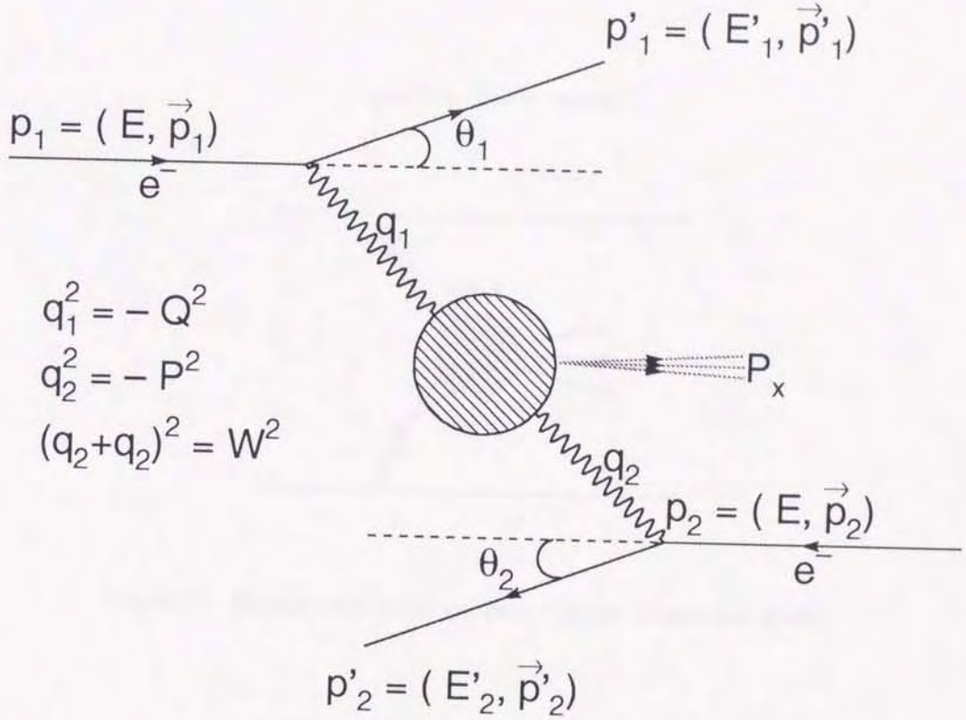

Figure 2.3: The basic diagram of the two-photon processes.

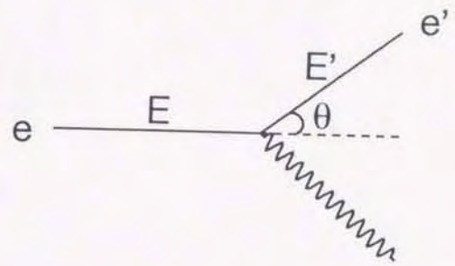

Figure 2.4: The eγ vertex.

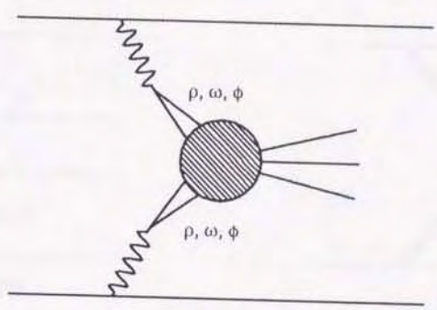

Figure 2.5: Hadron production via Vector Meson Dominance Model.

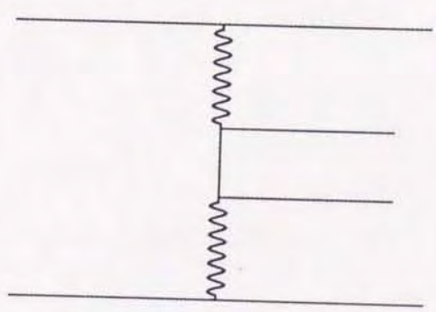

Figure 2.6: Hadron production via Quark Parton Model.

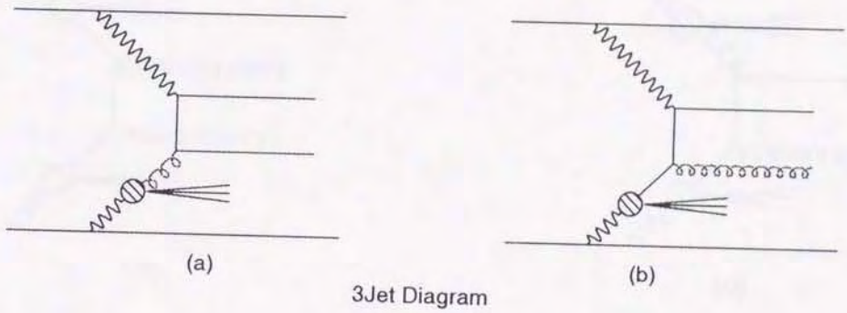

Figure 2.7: One resolved photon process.

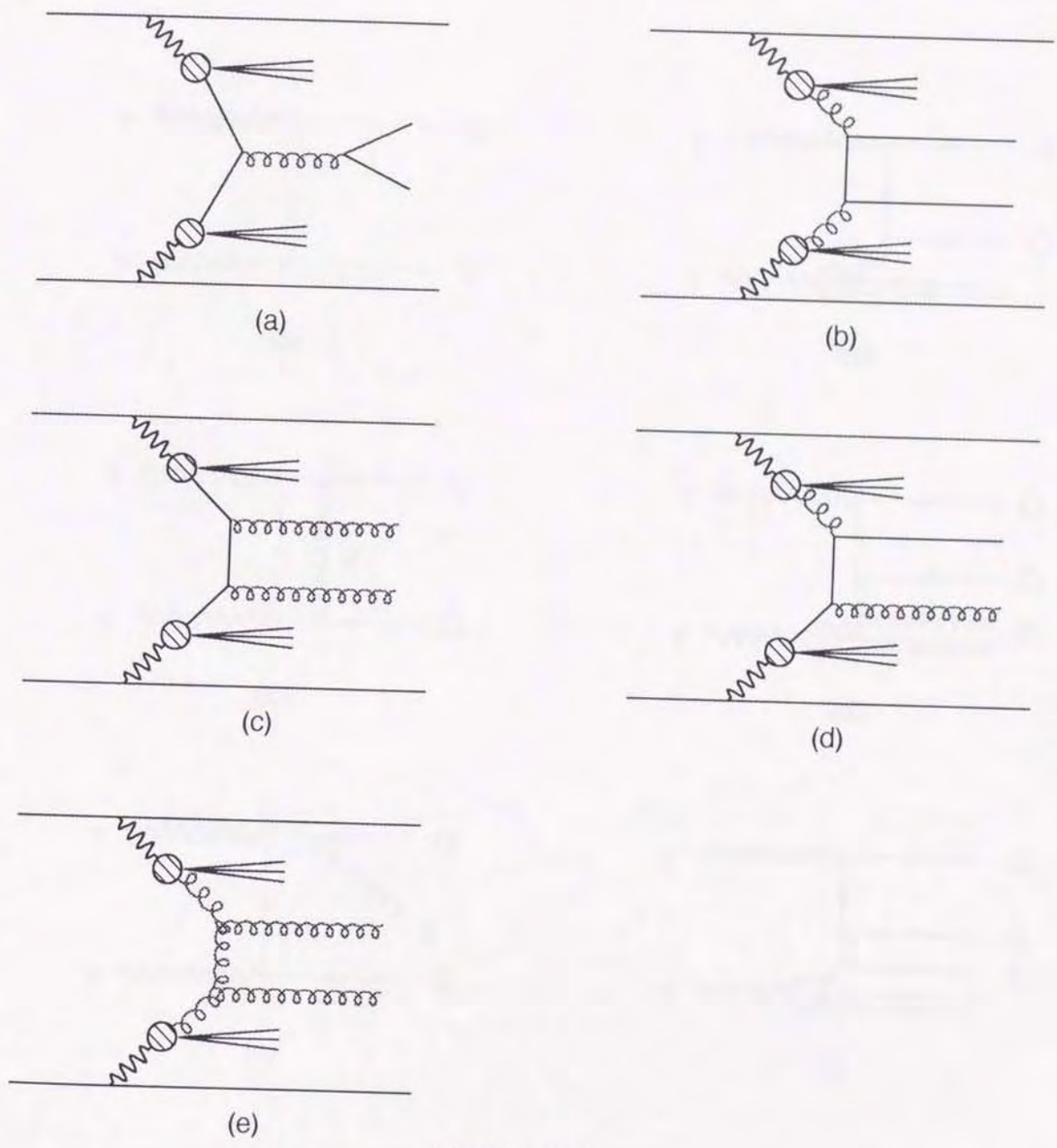

Figure 2.8: Twice resolved photon process.

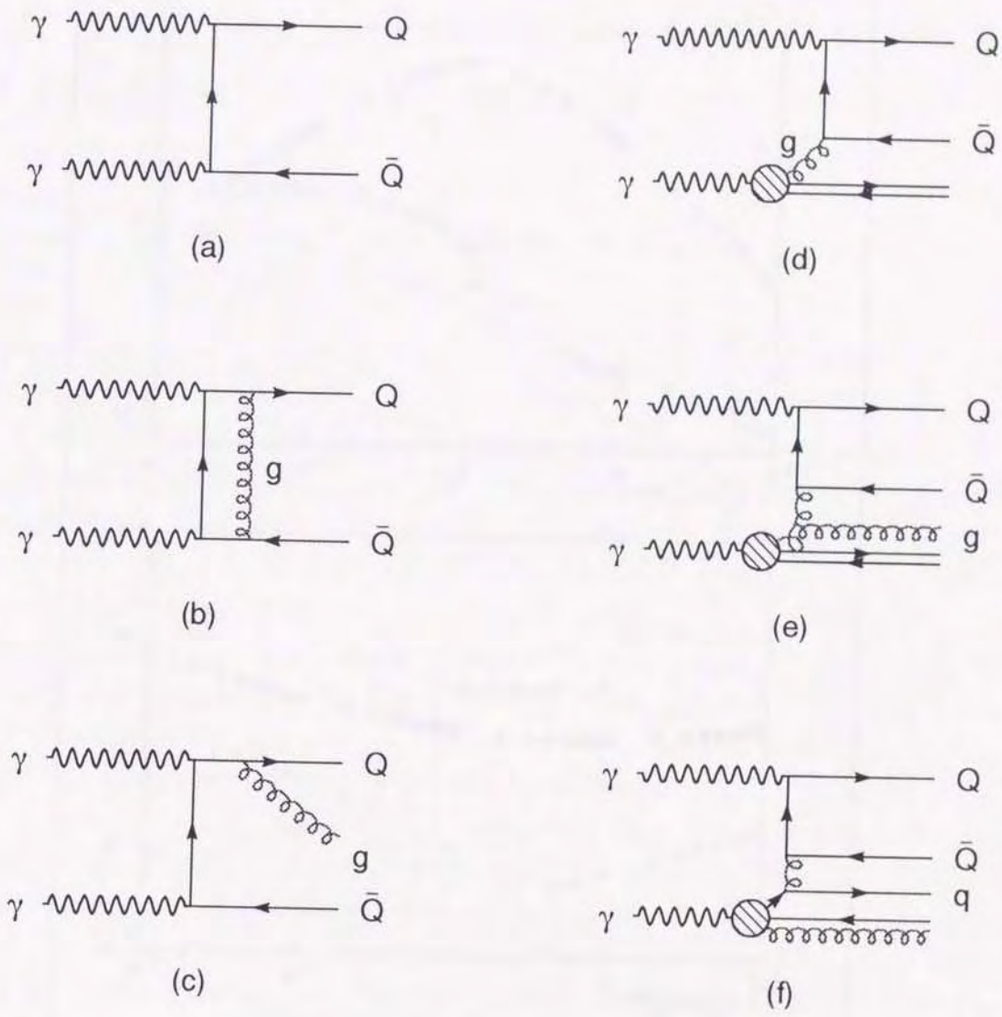

Figure 2.9: The diagrams for heavy quark production in $\gamma\gamma$ collisions.

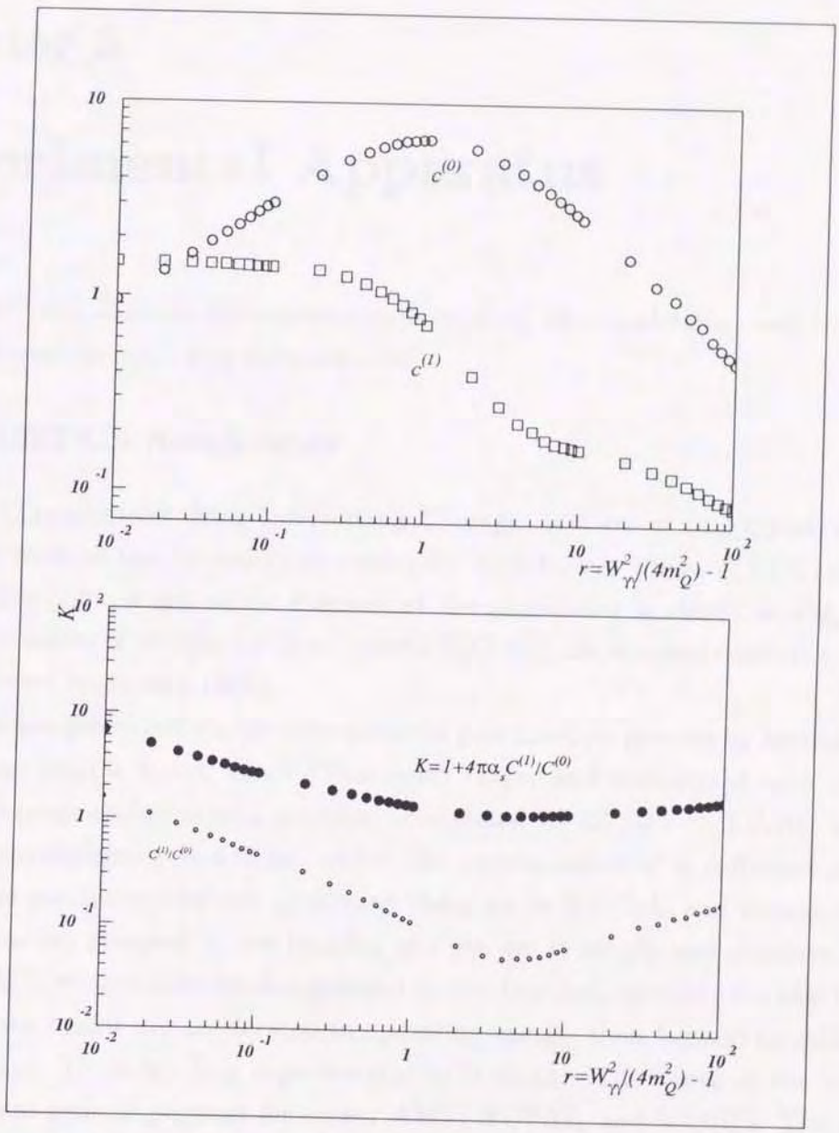

Figure 2.10: The value of term c^0,c^1 and the QCD correction factor (K) as a function of r for the direct process.

Chapter 3

Experimental Apparatus

This chapter will describe the experimental facilites, the accelerator, and the detector, which were used to make this measurement.

3.1 TRISTAN Accelerator

TRISTAN (Transposable Ring Intersecting STorage Accelerator in Nippon) is an e^+e^- storage ring built on the National Laboratory for High Energy Physics (KEK) in Tsukuba Scientific City [22]. A schematic diagram of the accelerator is shown in Fig. 3.1. The accelerator consists of an injector linac system (LINAC), an accumulation ring (AR), and a main colliding beam ring (MR).

Positrons are generated via electron-positron pair creation process by bombarding 200 MeV electron onto a heavy metal (Tantalum) target and transferred into the 400 m LINAC. Electrons and positrons are then accelerated to 2.5 GeV in LINAC and fed to AR whose circumference is 377 m. After the accumulation of a sufficient number of electrons and positrons, the AR accelerate them up to 8.0 GeV and injects them into MR. Electrons are grouped in two bunches of a few cm in length and circulate clockwise around the MR, while positrons also grouped in two bunches, circulate counter clockwise. In the MR, the beams are accelerated to operating energy, then focused to collide at the collision points. There are four experimental halls on the MR. Three of the interaction regions contain general purpose detectors, AMY, TOPAZ, and VENUS. The MR with circumferences of 3 km can accelerate and store electrons and positrons at about 30 GeV, providing e^+e^- collisions with a center of mass energy of $\sim$ 60 GeV. Parameters of the TRISTAN storage ring are shown in Table 3.1

Since 1990, the high luminosity run has started with the center of mass energy of 58 GeV for the purpose of high precision measurements. The integrated luminosity and daily

TRISTAN	
Location	KEK Tsukuba, Japan
Start	November 1986
End	March 1995
Beam energy	25 – 32 GeV
Beam energy spread (σ_E/E)	0.164%
Circumference	3018.1 m
Average MR radius	480.3 m
Beam crossing frequency	198.7 kHz
Beam spread in x (σ_x)	0.367 mm
Beam spread in y (σ_y)	0.023 mm
Beam spread in z (σ_z)	11.7 mm
Number of $e^+(e^-)$ bunches	2(2)
bunch cross section (vertical×horizontal)	$23\mu m \times 367\mu m$
Number of interactions	4
Luminosity (peak)	$1\times10^{31}cm^{-2}s^{-1}$
Luminosity (average)	$2\times10^{30}cm^{-2}s^{-1}$
RF Frequency	508.6MHz (at $\sqrt{s}$ = 58 GeV)

Table 3.1: Parameters of the TRISTAN storage ring and collision beams.

luminosities, collected by AMY detector from the beginning of 1987 are shown in Fig. 3.2.

3.2 AMY Detector

The AMY detector [23] is located in the OHO experimental hall which is one of the four interaction points in TRISTAN e^+e^- collider. The overview of the AMY detector is shown in Fig. 3.3.

The central feature of AMY is a compact, high-resolution detector based on a 3 Tesla supper conducting solenoid [24] and optimized for lepton identification. This aspect distinguishes it from other storage ring detectors. The high field affords excellent momentum resolution, particularly for those particles which have momentum below about 1 GeV/c. In addition the high field allows us to keep the size of the detector small providing for superior muon identification. In this section, a brief description of characteristics of the AMY detector is given which is essential for this analysis.

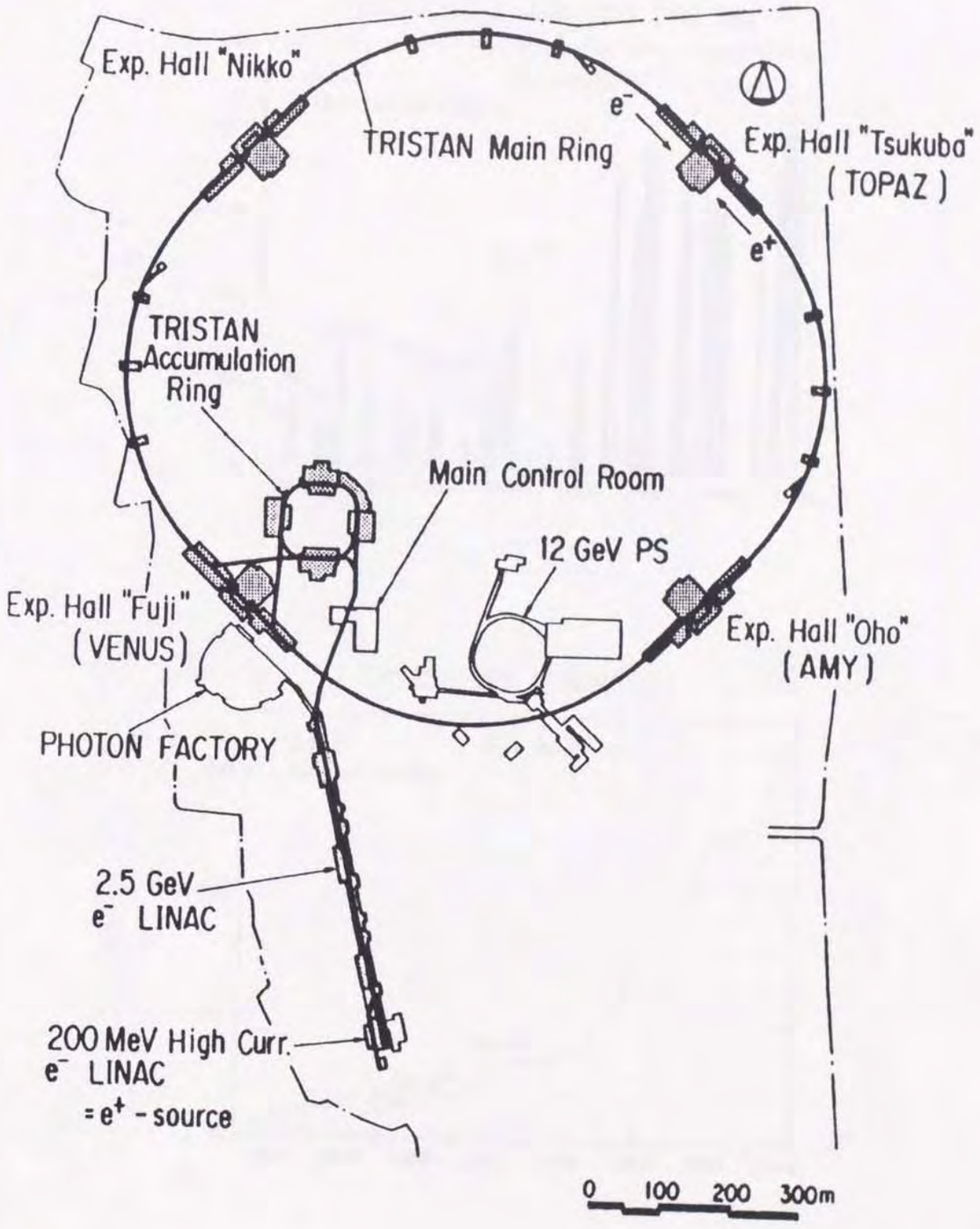

Figure 3.1: Overview of the TRISTAN accelarator.

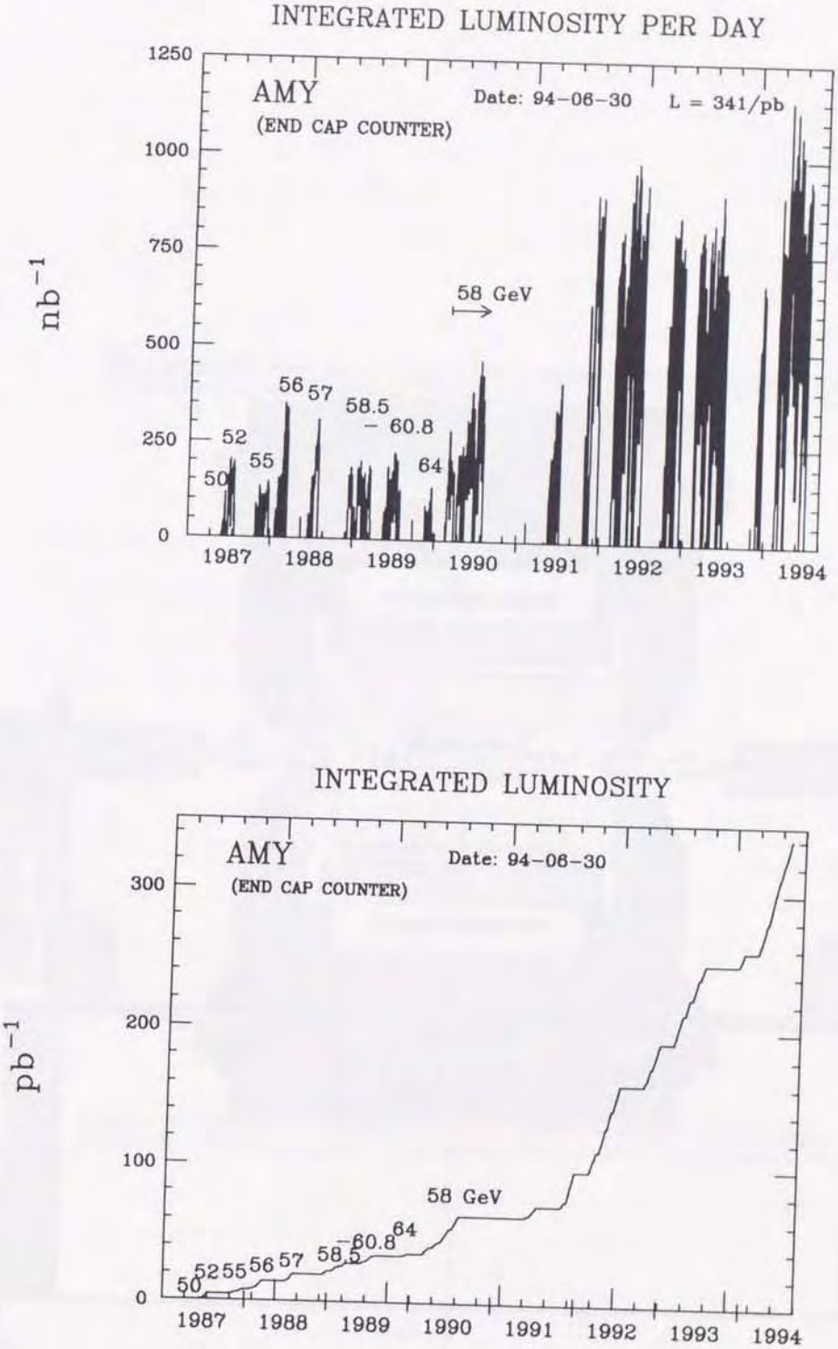

Figure 3.2: Average integrated luminosities per one day and integrated luminosity achieved by the AMY detector from 1987 to end of data taking.

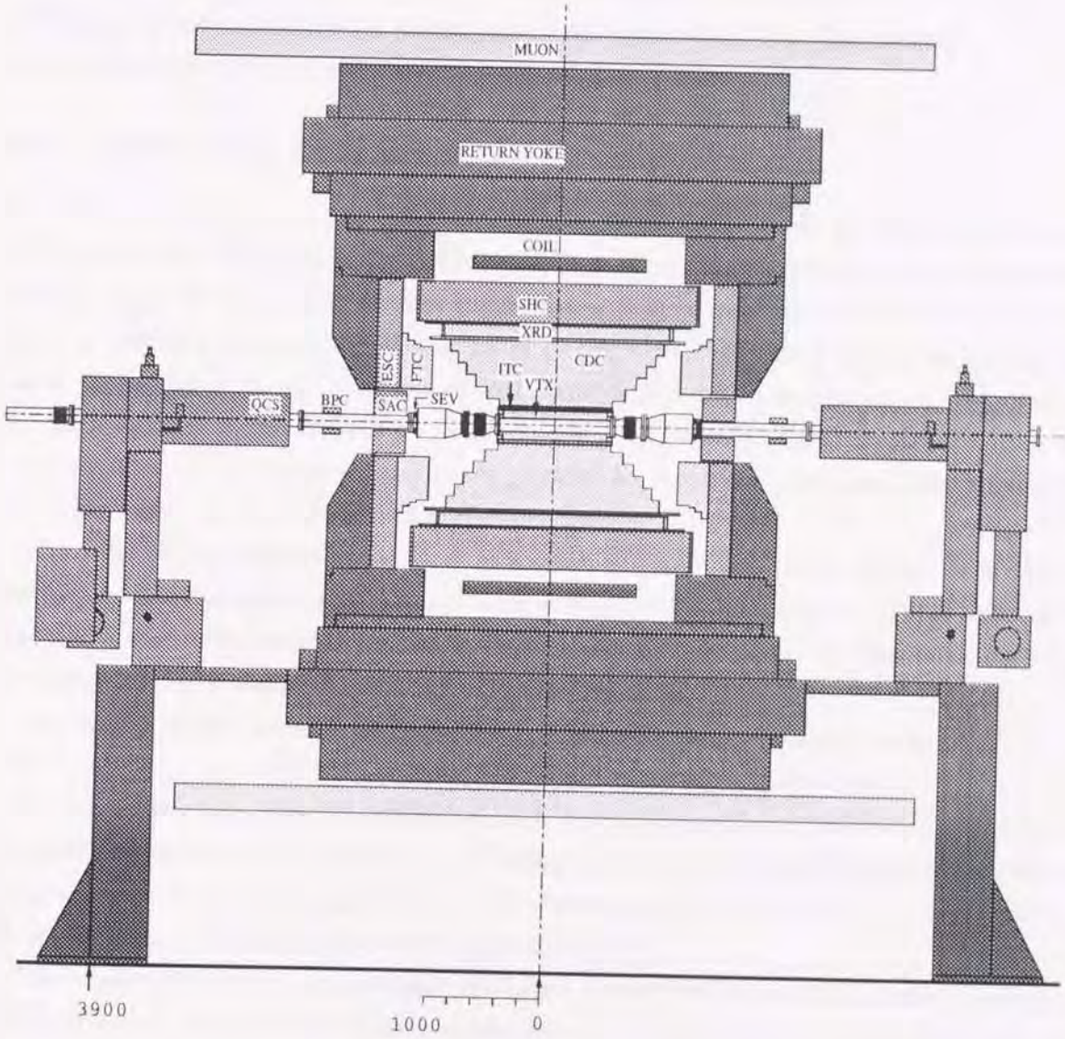

Figure 3.3: The AMY detector.

3.2.1 Inner Tracking Chamber

The inner tracking chamber lies in the inner part of the AMY detector. It provide information on the vertex of charged particles and to make fast and efficient trigger signals. With the ITC information, background from beam gas and cosmic ray events are rejected efficiently by reconstructing its vertex. The ITC is a drift chamber with four layers of cylindrical plastic tubes with aluminum coated on the inside. Fig. 3.4 shows a cross sectional view of the ITC tubes. Tubes of 3 mm in radius of 12.2 cm and outer radius of 14.2 cm. Signals are read out by TDC (Time to Digital Convertor)'s and ADC (Analog to Digital Convertor)'s through preamplifiers and discriminators. The position resolution determinated from the Bhabha tracks is 85 μm in r-ϕ plane.

3.2.2 Central Drift Chamber

The reconstruction of charged particle tracks is mainly performed by using signals from the Central Drift Chamber (CDC). The CDC is a cylindrical ring form with an inner and an outer radii of 16 cm and 65 cm, respectivery (Fig. 3.5). The chamber consists of 6 bands of different lengths. The inner band of the drift chamber is 93 cm in length and extend to radius of 20 cm. The outermost band is 180 cm in length and a radius of 65 cm. Each band is strung between two 2.5 cm thick end-plates. CDC consists of 40 layers of wires. The 25 layers have axial wires parallel to the beam direction (the z-axis) for measuring the r$-\phi$ coordination of trajectory points.

The other 15 layers have stereo wires at a small angle about 4° with respect to the beam direction to provide small angle stereo measurements of z-coordinates. Total number of axial and stereo cells are 5616 and 3424 respectively. The chamber is filled with HRS gas (Ar 89%, CO_2 10%, CH_4 1%) at atomospheric pressure.

The length of each band is increased with increasing radius so that the angular region $|\cos\theta|<0.87$ is covered. Because of this band structure, independent track vectors (position and direction) are determined at each band. This makes possible to provide quick estimation of multiplicity and momenta of charged particles for triggering and functioning fast the whole data acquisition system. This needs to measure efficiently and precisely the tracks in complicated events with high multiplicity.

The current spatial and momentum resolution of the CDC is $\sigma \sim 170$ μm and $\Delta p_t/p_t \sim 0.7\% p_t$ (GeV/c), respectively. These resolutions are obtained by analyzing Bhabha scattering events ($e^+e^- \rightarrow e^+e^-$).

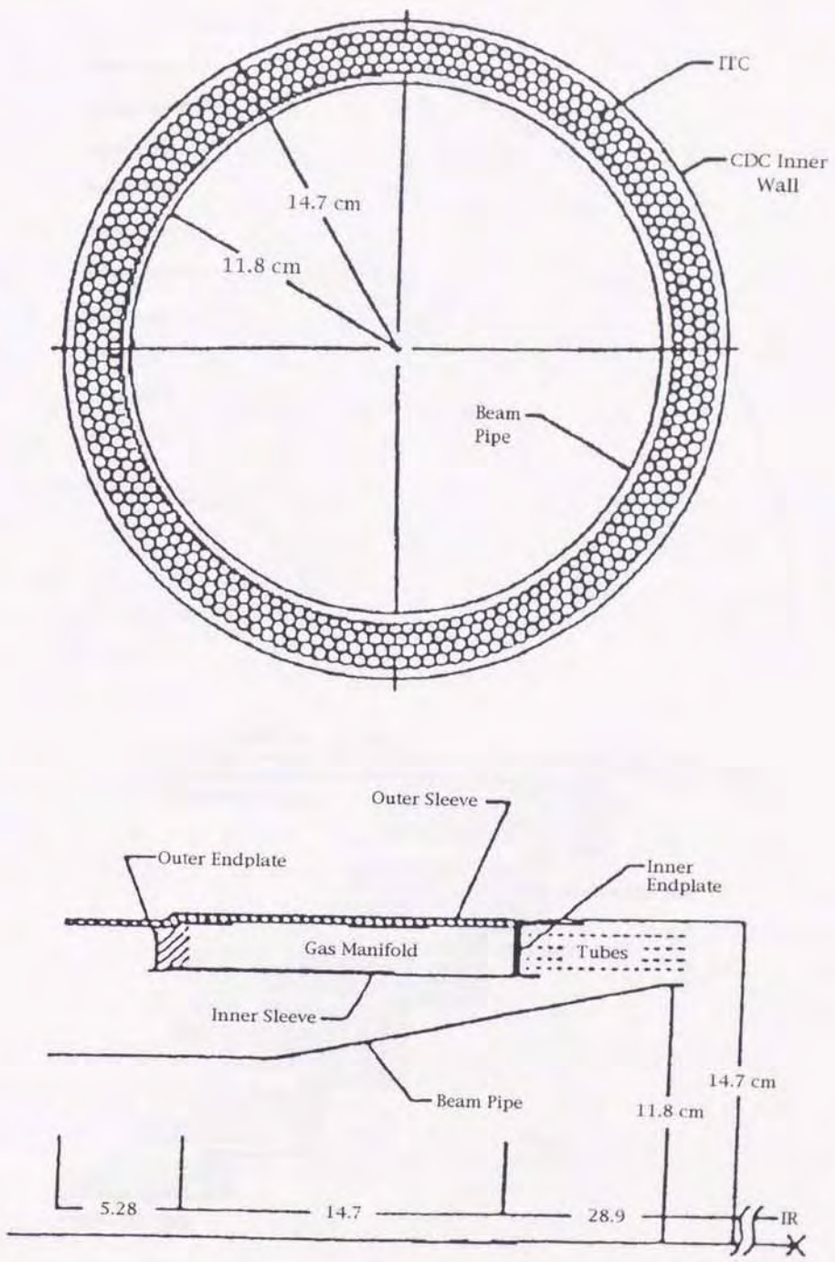

Figure 3.4: The Inner Tracking Chamber

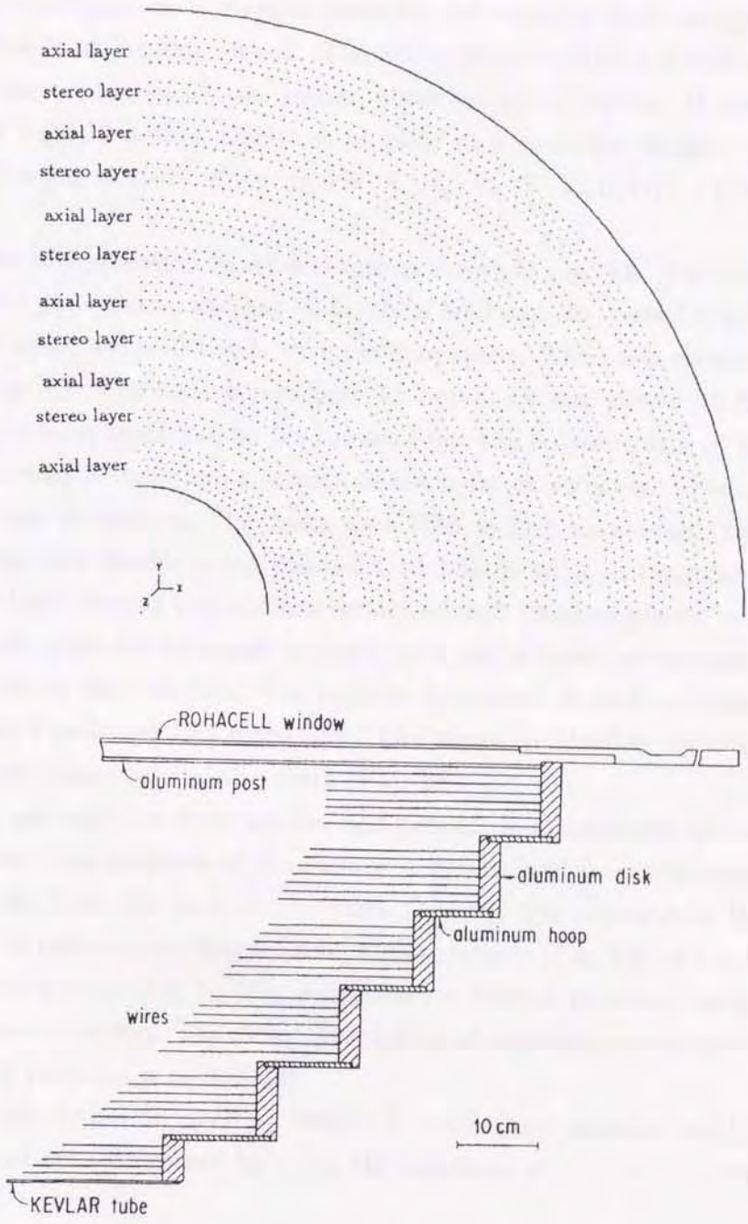

Figure 3.5: The Central Tracking Chamber

3.2.3 Electromagnetic Shower Counter

The barrel electromagnetic shower counter (SHC) [25] is designed to detect photons and identify electrons from other charged particles and measure their energies. The SHC is located just inside of the magnet coil. The active area is cylindrical shell with a length of 222 cm, an inner radius of 79 cm, and an outer radius of 110 cm. It covers the angular region $|\cos\theta| < 0.73$ with a thickness of $14.5/\sin\theta$ radiation length. The detector is operated with a gas mixture of Ar 49.3% , C_2H_6 49.3%, C_2H_5OH 1.5% at a voltage of 2150 volts.

The counter is constructed in six sextants as shown in Fig. 3.6. The each of sextants is a self-contianed gas volume, and has 20 layers of lead pannels, resistive plastic tubes, and cathode pads which are G10 boads with cathode strips. The basic structure of one layer is shown in Fig. 3.7. The basic layers have 3.5 mm thick lead sheets (0.625 X_0) in each layer. The innermost layer has no lead sheet since the bottom plate of the sextant (2.4 mm stainless steal) is mounted as a part of the support structure. Following this layer are 15 of the basic structures. The layers from 17th to 20th have double thickness of lead.

Cathode pads are double sided printed G10 boards with rectangular cathode strips and placed on both the top and bottom surface of each resistive plastic tube. The etched strips in cathode pads are arranged to make up θ and ϕ tower structures relative to the interaction point of the detector. The angular increment of each cathode tower is 13.5 mrad (0.77°) for θ pads and 16.4 mrad (0.93°) for ϕ pads in the first eight layers and twice wider than these values beyond the ninth (Fig. 3.8).

The signals are read out from anodes and two kinds of cathodes which are called θ-pads and ϕ-pads. The position of the shower is determined from the signals of cathode pad. The signals from the pads in the same tower of the consecutive layers are combined together to make up five lognitudinal segmentations (Fig. 3.9) of the shower conter. The signal division according to this segmentation scheme provided an optimized electron/hadron discrimination. The detail description of determining energies and positions of the showering particles is in Ref.[26].

The energy resolution of $\sigma_E/E \sim 23\%/\sqrt{E} + 6\%$, and position resolution of σ_ϕ=4 mrad, σ_θ=3 mrad are determined by using the reactions, $e^+e^- \rightarrow e^+e^-$, $e^+e^- \rightarrow \gamma\gamma$, and $e^+e^- \rightarrow e^+e^-\gamma$.

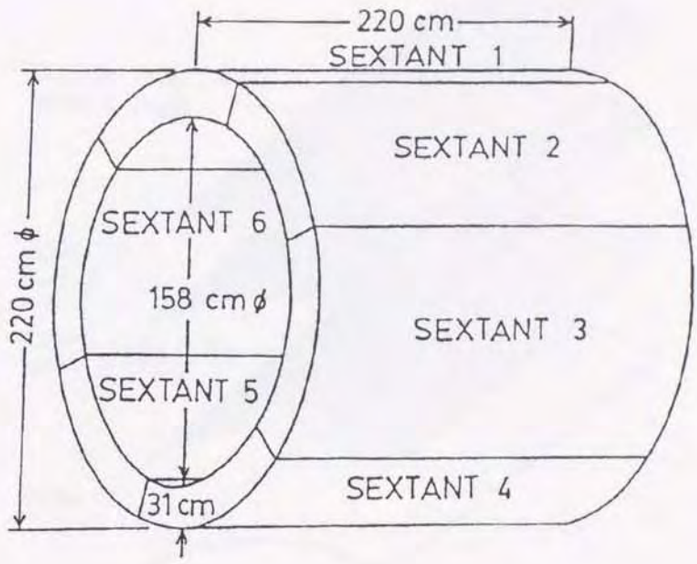

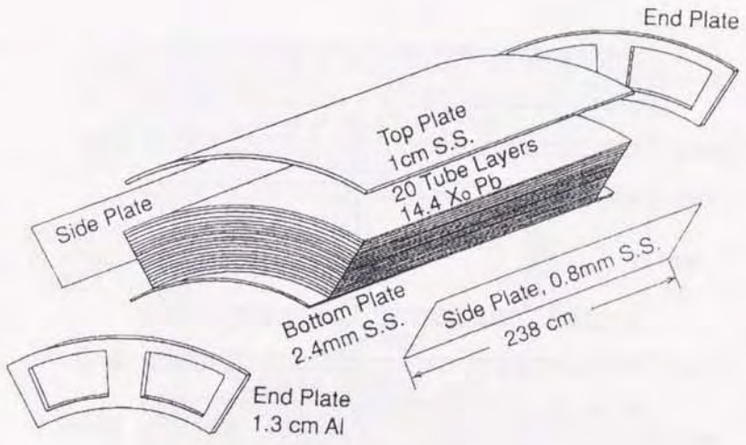

Figure 3.6: The Electromagnetic Shower Counter with the overall dimensions, and an exploded view of one sextant.

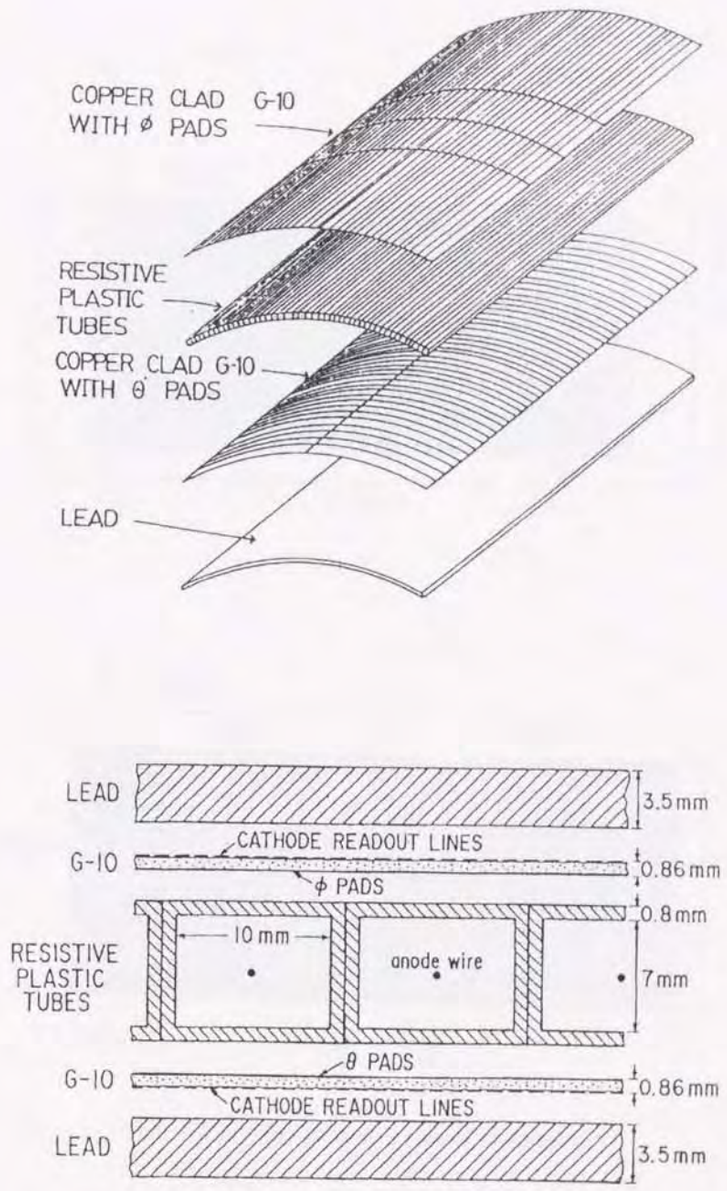

Figure 3.7: The components of a basic layer.

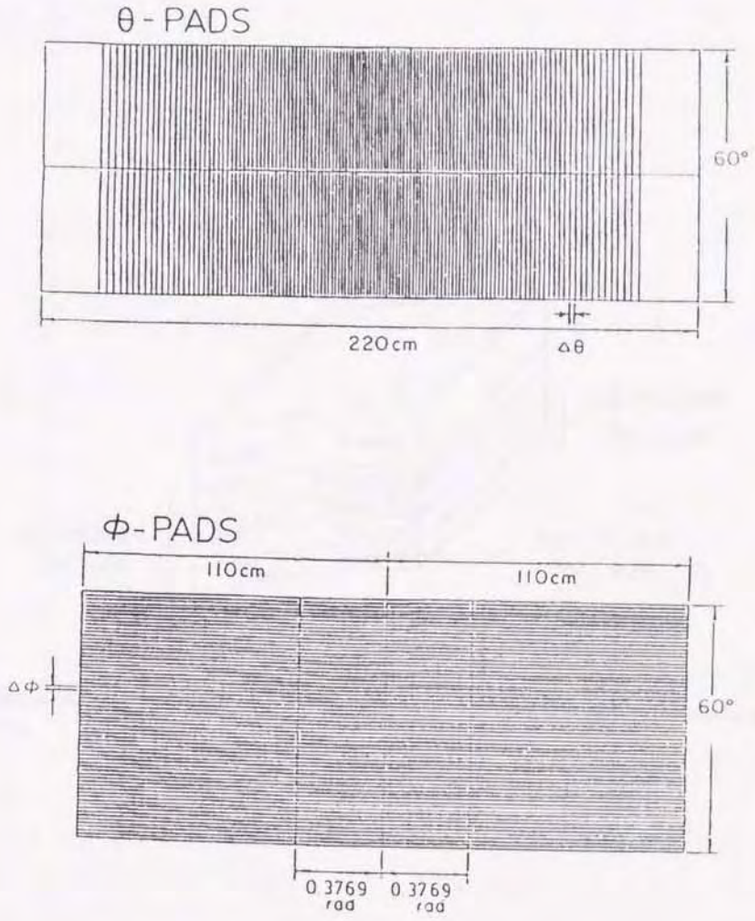

Figure 3.8: The cathode strips of a sextant.

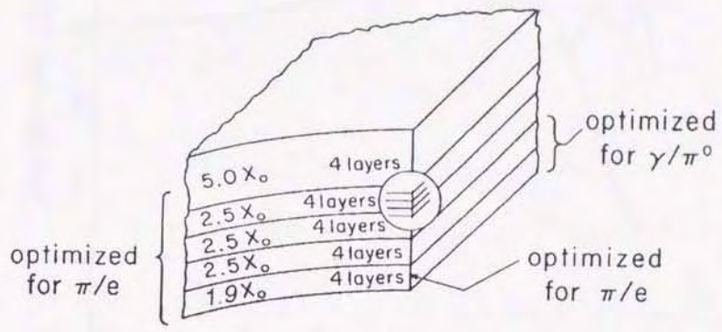

Figure 3.9: Longitudinal segmentation of SHC. 4 layers are combined together to make up one of logitudinal segmentations.

3.2.4 Muon Identifire

Muons are identified by their penetration through the meterial of the SHC, the superconducting solenoid, and the magnet iron. The average thickness of these absorbers is an equivalent to 1.65 m of iron which corrsponding to ~ 9 nuclear absorption length(λ_a). It is thick enough to reduce the number of the penetrating hadrons. For muons to reach the drift tube chambers for being tagged they have to travel these absorbers. The thickness of the absorbers are shown in Fig. 3.10

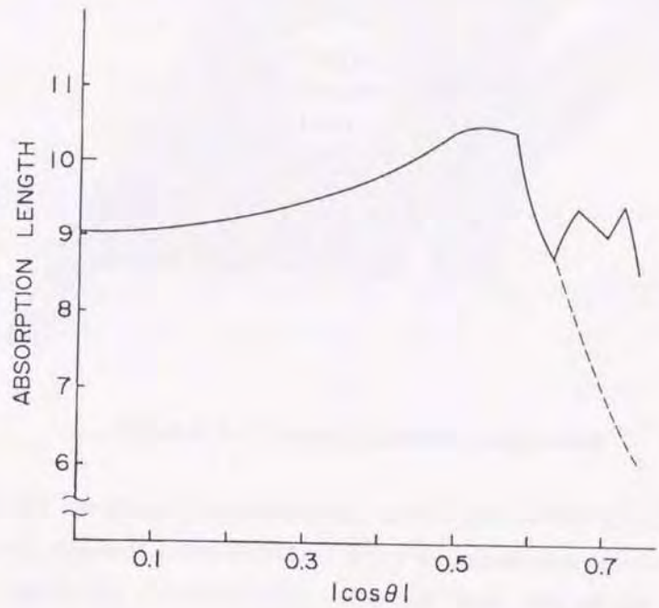

Figure 3.10: The thickness of the hadron absorber.

The muon system consists of two orthogonal double layer planner drift chambers to measure the exit location of muons from the iron and scintillation counters providing the time of flight of the muons. The chambers and sintillation counters for muon indentification are situated outside of the iron return yoke as seen in Fig. 3.11. It covers the angular region $|\cos\theta| < 0.74$.

The muon drift chamber is an assemble of eight-cell aluminum modules. Each cell has dimension of 5 cm $\times$ 10 cm. The cells of a module are arranged in two layers with a half cell stagger to assure high efficiency as shown in Fig. 3.12. The staggering serves to resolve the left-right ambiguty. The spatial resolution is typically a few mm. All modules are glued togather in 6 chambers, one for each of the six faces of magnet iron parallel to the beam. Each chambers has two layers of modules, one with axial direction and 290

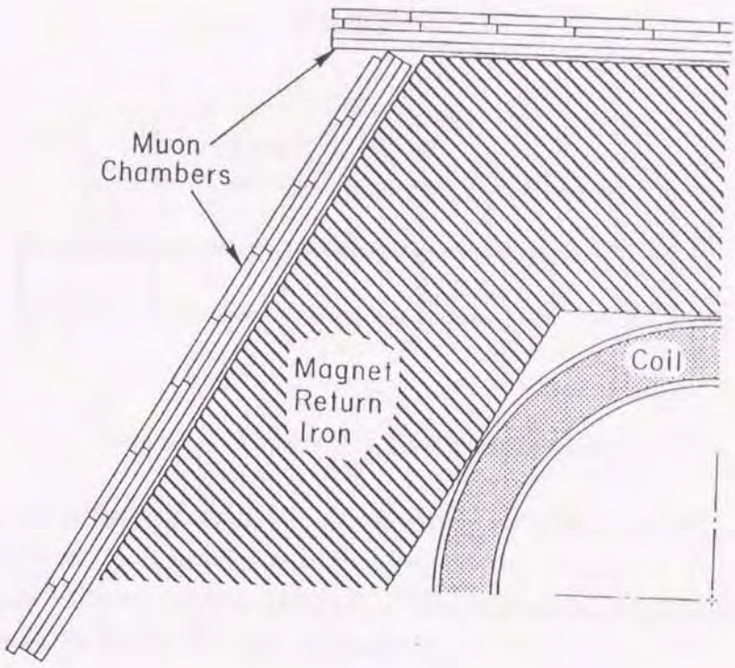

Figure 3.11: The muon chamber configuration.

cm, 360 cm, or 410 cm (two chambers each) in the azimuthal direction. The combined system has a track segment reconstruction efficiency that is greater than 98%.

The muon scintillation counter is located outer most side of the detector. The main function of this counter is to measure the time of penetrating particles relative to the beam crossing time with a precision of about 3 ns. The timing information provided from muon counter is used mainly to descriminate against backgrounds from cosmic rays of which timings are randomly distributed.

3.2.5 Endcap Detector

The Endcap Shower Counter (ESC) measures the energy of electron and photons, and position of charged particles. The ESC is used for luminosity measurement. It covers the angular range from 10° to 40° with respect to the beam axis.

The ESC has three main component which are proportional chambers sandwiched by two electro-magnetic calorimeters. The front calorimeter is made of 5 lead sheets and plastic-scintillators, of which thickness are 5 mm. This corresponds to 4.5 radiation

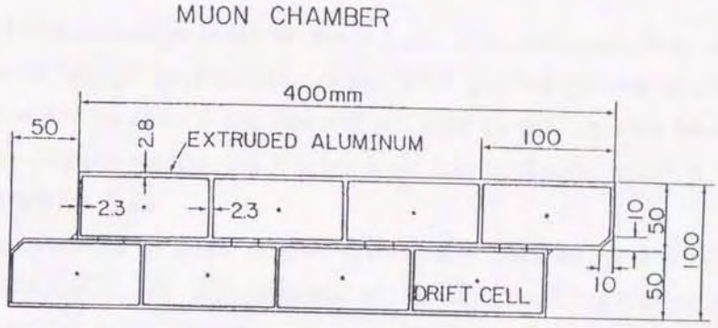

Figure 3.12: Endview of a muon chamber module.

length. The rear calorimeter is made of 10 lead sheets and plastic-scintillators each which thickness are 5 mm both. It has 8.9 radiation length.

The energy resolution is $\sigma_E/E \simeq 15\%/\sqrt{E} + 5\%$. The position resolution is about 2.4 mrad and 8.0 mrad for θ and ϕ angles, respectively.

3.2.6 Trigger System

At TRISTAN, beam crossings occur in every 5 μs. The maximum data acquisition rate is 3~4 Hz because of limited performance of the VAX 11/780 system which serves the data acquisition. In order to reduce the acquisition rate to manageable level and keep high efficiency for the physics events, the trigger logic has to decide whether the event should be taken or not within 5 μs.

The main components of AMY trigger system are track triggers (ITC and CDC) and energy triggers (SHC)[27, 28]. The principle of the CDC tracking trigger involves counting the number of radial track segments in each CDC band and classify them into event types (Multi-track, 3-4 track, 2 track event etc..) using these band tallies together with information from the shower counter. The CDC tracking trigger uses hit information of axial layers which are called "super-layers". One super layer consists of 4 layers of axial wires. There are 4 "super-layers" corresponds to disk(band) 2-4. Identification of radial track segments is accomplished by memory mapping in 16K $\times$ 1 bit RAMs whose memory is preloaded so that it gives output "1" only if the section has at least one track pattern corresponding to "radial" track. Each RAM covers a field of 14 adjacent wires in one band (referred to as a sector). Field of adjacent sectors overlap by six wires each neighbor (Fig. 3.13). Track recognition RAMs are mounted on printed circuit boards. The identified track segments are tallied using MAjority Logic Units (MALU) to produce a summed current, followed by a flash ADC stage. The numbers of track segments for super-layers 2 to 6 are fed into two Memory Look Up (MLU) modules which give the event type class (class 0-15) according to patterns of numbers of track segments in each super-layer.

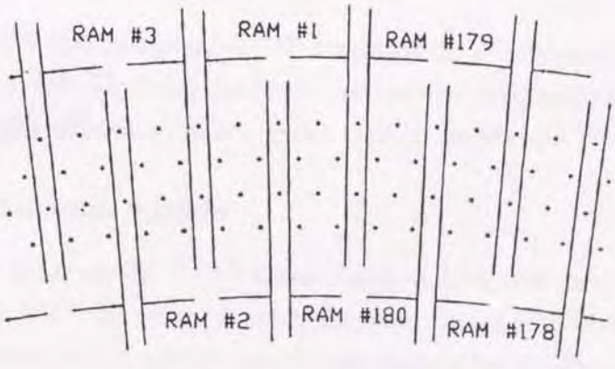

Figure 3.13: CDC RAM sectors.

The philosophy and firmware for SHC trigger is quite similar to CDC trigger. 48

summed signals each for outer 4 layers and inner 16 layers are fed into 16-channel latching descriminators which provide the analog majority output proportional to number of inputs. Signals from inner layers are split into 2 sets of discrimenators which have different threshold levels, i.e High and Low energy thresholds. Majority outputs of each 48 inputs are fed into FADC and MLU which counts number of clusters for minimum ionizing, high and low energy thresholds, and then classify events just in the same way as CDC trigger case. Outputs from each component are combined together and final triggers are formed. At this point, the several MLU are used for the final triggers. The total processing time is about 1.2 μs. The Fig. 3.14 shows diagram of the first stages CDC trigger.

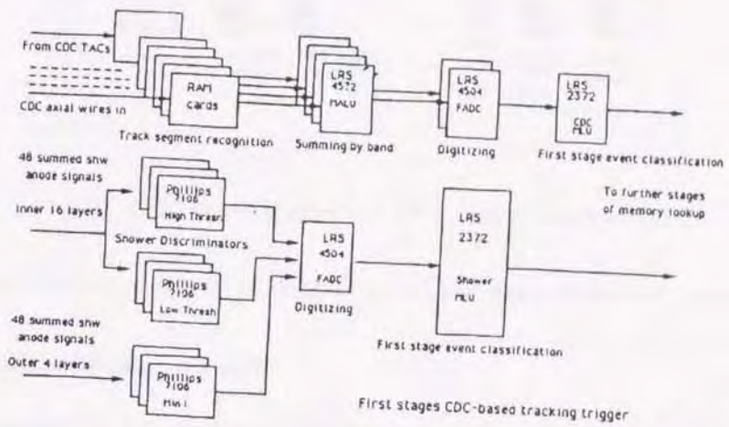

Figure 3.14: CDC first stages trigger.

The AMY detector has independent 32 combination of triggers. The trigger system summarized in Table 3.2. They are designed more or less independent and give redundant triggers so that trigger efficiency for the given type of events can be calculated.

3.2.7 Data Acquisistion System

A VAX 11/780 and the man TRISTAN computer(FACOM) are used as the data acquisition computer of the AMY detector. A computer-controleled FASTBUS/CAMAC system of electronics digitaizes analog signals and timing signals from each detector components for each event. Data are accumulated into the VAX11/780 through the FPI (VAX FASTBUS Processor Interface) temporarily, and transfered to the FACOM (M780) through a fast optical link. The data are stored in a cassette tape library for offline analysis.

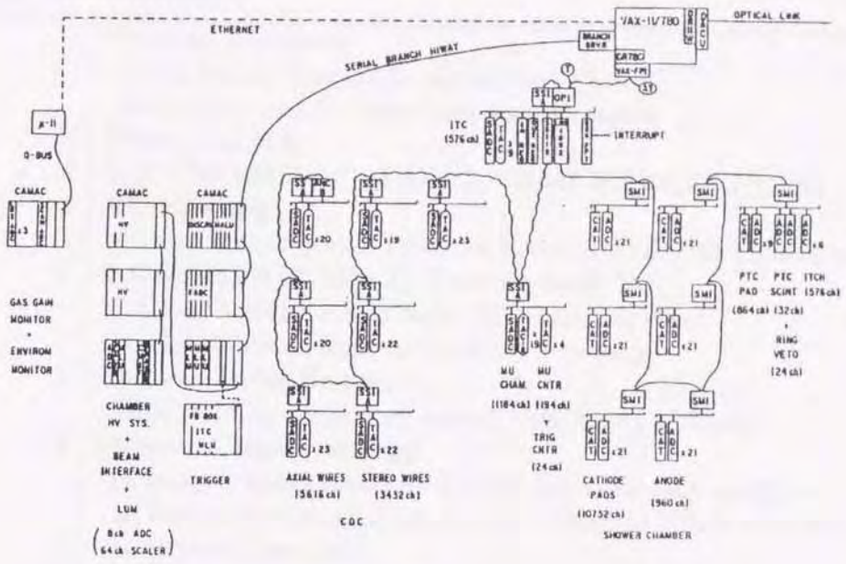

Figure 3.15: A schematic diagram of AMY data acquisition system.

Fig. 3.15 shows schematic diagram of data flows of the data acuisition system.

3.2.8 Lumonosity Measurement

A luminosity is measured by counting Bhabha events by calorimeters (ESC) siuated at forward and backword region of the AMY detector. The observed number of Bhabha events are compared with the Monte Carlo simulation based on the calculation up to $\mathcal{O}(\alpha^3)$. The systematic error of the luminosity measurements is estimated to be 1.46% in total. The source of systematic errors are listed in Table 3.3. The integrated luminosities for each run period collected AMY1.5 detector are shown in Table 3.4.

Trigger Bit	Definitions
1	**Endcap Dimuons** [(Fuji Front/Rear)⊗(Tsukuba Front/Rear)] with clean and straight back-to-back signal.
3	**Prescaled BX**
4	**(≥2 CDC RT)⊗(≥ 1 CDC/SHMI RT)⊗(ITC CSS)**
5	**EC Bhabha** [(Fuji Front/Rear)⊗(Tsukuba Front/Rear)] with high-threshold.
6	**2 CDC/(SHW Min I) back-to-back RT** 2 CDC/SHMI back to back RT which are ether straight back-to-back or slant back-to-back.
8	**Shower Total Energy** Sum of 16 layers in each tower, then tower summed.
9	**Shower Cluster energy** (4 ganged layers made by first 16 layers in each sextant) ⊗(2 successive ganged layers have "hits" in either sane sextant or adjacent sextant).
11	**ESC two photon + CDC** (Fuji/Tsukuba Front and Rear with high-threshold) ⊗(≥ 2 CDC tracks with low quarity).
12	**BPC BhaBha (Prescaled)**
13	**(≥ 2 ITC Tracks)⊗CDC⊗(SHW Min I)** (≥2 ITC tracks better than wimpty)⊗(CDC ≥ 5 segments in Disk4-6)⊗(SHW shower Min I).
14	**(ITC 2 Tracks back-to-Back)⊗CDC** CDC ≥ 4 segments in Disk2 and Disk3.
15	**(ITC 2 Track)⊗CDC⊗(SHW Low Majority 1)**
16	**ITC MultiTrack** ITC ≥ 7 tracks better than wimpy.
17	**CDC Multi Track** (CDC ≥ 5 segments in ≥ one of Disk2-6) ⊗(≥ 4 segments in ≥ four of Disk2-6) ⊗(≥ 3 segments in ≥ all of Disk2-6)
18	**(CDC Looser MultiTrack)⊗(Sh Min I)** (CDC ≥ 5 segments in ≥ 1 of Disk2-6) ⊗(≥ 4 segments in ≥ 3 of Disk2-6) ⊗(≥ 3 segments in ≥ 4 of Disk2-6) ⊗(SHW shower Min I).
19	**Shower Cluster** (Shower High-Majority 1 and Shower Low Majority 2) ⊕(Shower Low Majority 3)
20	**(Looser SHW cluster)⊗CDC⊗NOT(T19)** (CDC ≥ 1 segment in ≥ 4 of Disk2-6) ⊗(SHW shower majority 2 or High Majority 1) ⊗(Not Tigger 19).

Trigger Bit	Definitions
21	**(CDC 2 Track)⊗ITC⊗(SH Min I)** (ITC CSS)⊗(CDC 2 segments in ≥ four of Disk2-6) ⊗(≥ 1 segments in all of Disk2-6) ⊗(≤ 4 segments in all of Disk2-6)
22	**CDC 3 or 4 Track** (CDC ≥ 1 segments in Disk1) ⊗(≥ 1 segment in each of Disk2-6) ⊗(≥ 3 segments in two of Disk2-6) ⊗(≤ 7 segment in each of Disk2-6) ⊗(≤ 2 departures from monotonically nondecreasing number of segments counting from Disk2-6).
23	**(ITC 2 Tracks)⊗MU** (ITC 2 tracks better than wimpy) ⊗(CDC ≥ 5 segments in Disk4-6) ⊗(MUO 2 hits MUO scintilators in different 12th layers).
24	**(ITC 2 Track)⊗CDC⊗(Sh Min I)** (ITC 2 tracks better than wimpy) ⊗(CDC ≥ 5 segments summed in Disk2-6) ⊗(SHW Shower Min I Majority 2).
26	**ESC⊗(CDC Dimuon)** (CDC pattern of segments in Disk2-6 is 22222/22221/22220/22210/22200/22100) ⊗[(ESC Fuji and Tsukuba clean back-to-back with majority 3) ⊕(ESC Fuji and Tsukuba clean slant back-to-back with majoity 4)].
27	**ESC⊗(FTC Dimuon)** (FTC ≥ 1 track segment in Fuji layer1) ⊗(≥ 1 track segment in Tsukuba layer1) ⊗(≤ 3 segments in Fuji and Tsukuba layer1) ⊗(ESC the same as in Trigger 26).
28	**SAC⊗CDC** (SAC one of 16 sectors)⊗(CDC ≥ Bachelor V)
29	**ESC 2 Photon (Prescal)**
30	**CDC Prefect 2 Track** (ITC CSS)⊗(CDC 2 segments in each of Disk1-6).
31	**CDC Perfect 1 Track or Bachelor V, later CDC perfect 1 track or Bachelor V or acoplanar 2 tracks** (ITC CSS)⊗(SHW Shower Min I Majority 1) ⊗[(CDC Prefect 1 track) ⊕(Bachelor V)].

		Definitions
CDC RT	:	CDC radial track $\geq$ 1 segments in either same or adjacent microsector in 4 disks of Disk2-6.
CDC/SHMI	:	CDC/SHMI radial tracks ($\geq$ 1 segments in either same or sdjacent microcector in 4 disks of Disk2-6) $\otimes$($\geq$ 1 Shower Min I in the same microsector as CDC track segment).
ITC CSS	:	ITC Cosmic Suppression Signal [(ITC HV)$\otimes$($\geq$ 1 ITC track segment)] $\oplus${(not ITC HV) $\otimes$[(CDC Disk1 HV)$\otimes$($\geq$ 1 CDC track segment in Disk1)] $\oplus$(not CDC Disk1 HV)}

Table 3.2: Summary of triggering definitions, where $\otimes$ and $\oplus$ means logical "AND" and "OR", respectively. Conditions may slitly vary between run period.

Source	Systematic Error (%)
Acceptance Estimation	0.48
Background Correction	0.04
Alignment	1.22
Miscellaneous	0.4
Higher order Correction	0.5
Total	1.46

Table 3.3: The source of systematic errors in the luminosity measurements.

Year	run period	$\sqrt{s}$ (GeV)	Integrated Luminosity (pb^{-1}) *(stat.)*	(PMT)	*(sys.)*
'90 Spring	8378-10896	58.0	26.73±0.10	–	±0.39
'91 Spring	10983-11805	58.0	8.10±0.06	±0.04	±0.12
'91 Fall	11821-12639	58.0	25.73±0.10	–	±0.38
'92 Spring	12650-14579	58.0	62.92±0.15	±0.12	±0.92
'92 Fall*	14594-15259	57.772	19.29±0.08	–	±0.28
	15260-15292	59.466	0.96±0.02	–	±0.01
	15293-15330	57.972	1.37±0.02	–	±0.02
	15331-15373	58.968	1.35±0.02	–	±0.01
	15375-15412	58.22	1.30±0.02	–	±0.02
	15413-15458	58.47	1.31±0.02	–	±0.02
	15459-15519	58.718	1.70±0.02	–	±0.03
	15520-15562	59.216	1.19±0.02	–	±0.02
	15563-15630	57.374	2.02±0.03	–	±0.03
'93 Spring	15657-17686	58.0	56.09±0.14	–	±0.82
'93 Fall	17722-18168	58.0	10.03±0.26	±0.33	±0.15
'94 Spring	18173-20160	58.0	89.11±0.09	±0.11	±1.30

Table 3.4: The list of integrated luminosities achieved by AMY1.5 detector for each of run periods. PMT indicates the error due to dead photo-tube correction. In this analysis, data during '91 spring and '91 fall have not used, since the trouble in CDC made momentum resolution wose especially for low monentum tracks. *)For '92 Fall run period, the correction of beam energy shift is included. Thoes are about $-0.4\%E_{beam}$ from nominal value and makes the integrated luminosities slightly decrease.

3.2.9 Detector Simulation

The AMY detector simulator (AMYSIM) simulates the response of the AMY detector.

AMYSIM makes charged and neutral particles swim through the various material in AMY detector in small steps. Many daughter particles are produced in the swimming steps by electromagnetic and hadronic processes and all of those particles should be tracked inside the detector.

Electromagnetic showers are computed by the program EGS4 [29] and hadronic interactions inside the detector are treated by Gheisha [30]. The simulated detector signals are converted into ADC (Analog to Digital Converter) or TDC (Time to Digital Converter) signals, and those data can be formatted in the same way as the experimental raw data. After AMYSIM, the Monte Carlo events can be processed by analysis program which is the same program used for the experimental data.

Chapter 4

Monte Carlo Simulation

4.1 Event Generator

The experimental results are compared with the theoretical predictions using Monte Carlo simulations. Events for both the direct and the photon-gluon fusion processes were generated with a Monte Carlo program based on the BASES and SPRING packages [31]. The differential cross section is integrated and a probability distribution is produced by BASES. SPRING generates four momentum vectors of events according to the probability distribution made by BASES. The produced quarks are fragmented in the JETSET7.3 program [32]. The generated events are then processed though a program that simulates the AMY detector. The procedure of Monte Carlo event generation is summarized in Fig. 4.1.

The direct process is modeled with a QPM event generator that incorporates all six first-order diagrams(Fig. 4.2) [33]. The contribution of the radiatve diagrams to the peripheral diagrams is about 4 %. Resolved photon events are generated according to the formulae given in Ref. [5]. Here, three different parameterizations—LAC1 [34], DG [35], and WHIT4 [36]—are used for the parton density in the photon.

In the BASES and SPRING stage, we take the charm mass to be 1.6 GeVc^2 in usual. We have also made another set of Monte Carlo events with charm mass of 1.3 GeV/c^2 in order to see the effect of the charm mass. The calculated corss sections relevant to the charm production are summarized in Table 4.1. In the calculation, the threshold was set at $2m_{D^*}$=4.0GeV/c^2 for the mass of $\gamma\gamma$ system.

4.2 Next-to-Leading Order QCD Correction

In this analysis, NLO QCD corections are taken into account to the direct and resolved photon processes.

In determing those corrections, we first remove the effects of hard gluon radiation from total NLO QCD correction [21, 8], since these are already included in our Monte Carlo generator by a parton shower scheme. The effects of hard gluon radiation appear only on the transverse momentum distribution, and makes it softer, because emitted gluon takes away energy and momentum from the charm quark. So far, the NLO QCD corrections for direct process are applied as a function of invariant mass of the $\gamma\gamma$ system $W_{\gamma\gamma}$. The correction factor K was derived from Eq. 2.29. The ratio of $c^{(1)}$ and $c^{(0)}$ was calculated by extracting the values as a function of r from Fig. 2.10. The obtained NLO QCD corrections as a function of $W_{\gamma\gamma}$ are shown in Fig. 4.3. The cross sections for each value of $W_{\gamma\gamma}$ are also shown in Fig. 4.4 and Fig. 4.5 for the different mass of charm quark.

In the case of resolved photon process, the factor of NLO QCD correction to LO cross section was calculated from Eq. 2.33. It is a p_T dependent correction factor, but the effects of hard gluon emission have already removed from the correction factor, so that it is possible to use Eq. 2.33 for NLO QCD correction with our Monte Carlo. The nomalization factor N is determined at $p_T^c > 1.2$ GeV/c and found to be 1.07.

Those effects are taken into account to our Monte Carlo by appropriately weighting the correction factors to the leading order predictions. The total cross sections with next-to-leading order corrections are also listed in Table 4.1.

Process	m_c (GeV/c^2)	Cross section (pb)		
		LO	NLO	K
Direct	$\gamma\gamma \to c\bar{c}$			
(QPM)	1.6	122.4	160.7	1.31
	1.3	150.3	187.9	1.25
1-Res.	$\gamma g \to c\bar{c}$			
(GRV) [37]	1.6	34.1	38.2	1.12
	1.3	42.6	–	–
(DG)	1.6	28.5	31.2	1.07
	1.3	36.2	–	–
(LAC1)	1.6	130.4	133.8	1.03
	1.3	172.7	–	–
(WHIT4)	1.6	94.2	–	–
	1.3	116.4	–	–

Table 4.1: The total cross section calculated by using Monte Catlo generator, where the $W_{\gamma\gamma} \geq 2m_{D^*}$=4.0 GeV/$c^2$ was applied as a threshold of charmed hadron production.

4.3 Fragmentation and Decay

The quarks are fragmented via the Lund string-fragmentation scheme. The direct process is evolved using a parton shower scheme. The fragmentation function of Peterson et al. [38],

$$f(z) = \frac{N}{z}\left(1 - \frac{1}{z} - \frac{\varepsilon_c}{1-z}\right)^{-2} \tag{4.1}$$

is used to describe the fragmentation of charm quarks. Here, $z = (E + p_{\parallel})_{hadron}/(E + p_{\parallel})_{quark}$, N is a normalization constant, and ε_c is the fragmentation parameter for charm quarks. We use $\varepsilon_c = 0.047$ [39].

The branching ratios for semileptonic decays of charmed mesons in the LUND decay table were adjusted to match the August 1994 update of the PDG Data Base [40]. The correction was performed in the following manner:

1) Use LUND default value if PDG does not give any value.

2) Replace it by PDG value, if the value given by PDG Data Base was different more than one standard deviation from the default value of LUND.

3) Adjust branching ratio of semileptonic decay channel Br(D$\rightarrow \ell$X) to PDG value, by multipling correction factor to Br(D$\rightarrow \ell$X).

Table 4.2$\sim$ 4.5 show the value of branching ratios refered from LUND default, PDG Data Base, and adopted values which were used in our Monte Carlo, for the all semileptonic decay channel. In Table 4.6, the correction factor for adjusting the ratio D$\rightarrow \ell^{\pm}$X are given for D_s, D^0, and D^+. The adopted branching ratios listed in Table 4.2$\sim$ 4.5 are multiplied by the factor given in Table 4.6. to match the PDG values of D $\rightarrow \ell^{\pm}$X. As an exception, the branching ratios $D^0 \rightarrow \ell^{\pm}$X were assumed to be 8.1% in total. PDG gives larger branching ratio for $D^0 \rightarrow \mu$X than that for $D^0 \rightarrow$ eX. Branching ratio for $D^0 \rightarrow \mu$X should be same or smaller than that for $D^0 \rightarrow$ eX due to strict phase space. Therefore, Br($D^0 \rightarrow \ell$X) was assumed by taking weighted average of the PDG values as

$$\overline{Br.} = \frac{\sum(x_i/\sigma_i^2)}{\sum(1/\sigma_i^2)} \tag{4.2}$$

where x_i and σ_i are value of branching ratio and its error given by PDG, and summation is done for eX and μX channel.

The other details of the Monte Carlo simulation are described in Ref. [41, 42].

We have generated the Monte Carlo events for the other processes in order to estimate the background contaminations in our event sample. The cross sections of those processes are shown in Table 4.3.

Decay Channel		Branching Ratio		
		Lund7.3	PDG '94	Adopted for MC
$D^{*+} \rightarrow$	$D^0\pi^+$	0.47	0.681 ± 0.013	0.681
	$D^+\pi^0$	0.34	0.305 ± 0.008	0.305
	$D^+\gamma$	0.17	$0.027^{+0.014}_{-0.007}$	0.027
$D^{*0} \rightarrow$	$D^0\pi^0$	0.52	0.636 ± 0.028	0.636
	$D^0\gamma$	0.48	0.364 ± 0.028	0.364
$D_s^{*+} \rightarrow$	$D_s^+\gamma$	1.00	1.00(dominant)	1.00

Table 4.2: Branching ratio of D^{*+}, D^{*0}, and D_s^{*+}.

Decay Channel		Branching Ratio		
		Lund7.3	PDG '94	Adopted for MC
$D_s^+ \rightarrow$	$\tau^+\nu_\tau$	0.010	–	0.010
	$e^+\nu_e\eta$	0.015	0.059	0.059
	$e^+\nu_e\eta'$	0.015	0.015	0.015
	$e^+\nu_e\phi$	0.017	0.0188 ± 0.029	0.0188
	$e^+\nu_e K^+K^-$	0.015	–	0.0015
	$e^+\nu_e K^0\bar{K}^0$	0.015	–	0.0015
	$\mu^+\nu_\mu\eta$	0.015	0.059	0.059
	$\mu^+\nu_\mu\eta'$	0.015	0.015	0.015
	$\mu^+\nu_\mu\phi$	0.017	0.0188 ± 0.029	0.0188
	$\mu^+\nu_\mu K^+K^-$	0.015	–	0.0015
	$\mu^+\nu_\mu K^0\bar{K}^0$	0.015	–	0.0015

Table 4.3: Branching ratio of D_s^+.

Decay Channel		Branching Ratio		
		Lund7.3	PDG '94	Adopted for MC
$D^0 \rightarrow$	$e^+\nu_e K^-$	0.015	0.038 ± 0.0022	0.038
	$e^+\nu_e K^{*-}$	0.020	–	0.020
	$e^+\nu_e \bar{K}^0\pi^-$	0.010	–	0.010
	$e^+\nu_e \bar{K}^-\pi^0$	0.010	$0.16^{+0.013}_{-0.005}$	0.010
	$e^+\nu_e \bar{K}^0\pi^-\pi^0$	0.004	–	0.004
	$e^+\nu_e K^-\pi^+\pi^-$	0.004	–	0.004
	$e^+\nu_e K^-\pi^0\pi^0$	0.004	–	0.004
	$e^+\nu_e \pi^-$	0.002	$0.0039^{+0.0023}_{-0.0012}$	0.002
	$e^+\nu_e \rho^-$	0.002	–	0.002
	$e^+\nu_e \pi^-\pi^0$	0.002	–	0.002
	$e^+\nu_e \pi^-\pi^0\pi^0$	0.002	–	0.002
	$e^+\nu_e \pi^+\pi^-\pi^-$	0.002	–	0.002
	$\mu^+\nu_\mu K^-$	0.015	0.032 ± 0.0004	0.032
	$\mu^+\nu_\mu K^{*-}$	0.020	–	0.020
	$\mu^+\nu_\mu \bar{K}^0\pi^-$	0.010	–	0.010
	$\mu^+\nu_\mu \bar{K}^-\pi^0$	0.010	–	0.010
	$\mu^+\nu_\mu \bar{K}^0\pi^-\pi^0$	0.004	–	0.004
	$\mu^+\nu_\mu K^-\pi^+\pi^-$	0.004	–	0.004
	$\mu^+\nu_\mu K^-\pi^0\pi^0$	0.004	–	0.004
	$\mu^+\nu_\mu \pi^-$	0.002	–	0.002
	$\mu^+\nu_\mu \rho^-$	0.002	–	0.002
	$\mu^+\nu_\mu \pi^-\pi^0$	0.002	–	0.002
	$\mu^+\nu_\mu \pi^-\pi^0\pi^0$	0.002	–	0.002
	$\mu^+\nu_\mu \pi^+\pi^-\pi^-$	0.002	–	0.002

Table 4.4: Branching ratio of D^0.

Decay Channel		Branching Ratio		
		Lund7.3	PDG '94	Adopted for MC
$D^+ \rightarrow$	$e^+\nu_e\bar{K}^0$	0.035	0.067±0.035	0.035
	$e^+\nu_e\bar{K}^{*0}$	0.030	0.048±0.005	0.048
	$e^+\nu_e\bar{K}^0\pi^0$	0.015	–	0.015
	$e^+\nu_eK^-\pi^+$	0.015	$0.042^{+0.009}_{-0.007}$	0.015
	$e^+\nu_eK^-\pi^+\pi^0$	0.044	–	0.044
	$e^+\nu_e\bar{K}^0\pi^+\pi^-$	0.022	–	0.022
	$e^+\nu_e\bar{K}^0\pi^0\pi^0$	0.022	–	0.022
	$e^+\nu_e\pi^0$	0.001	–	0.001
	$e^+\nu_e\eta$	0.001	–	0.001
	$e^+\nu_e\eta'$	0.001	–	0.001
	$e^+\nu_e\rho^0$	0.001	–	0.002
	$e^+\nu_e\omega$	0.001	–	0.001
	$e^+\nu_e\pi^+\pi^-$	0.001	–	0.001
	$e^+\nu_e\pi^0\pi^0$	0.001	–	0.001
	$e^+\nu_e\pi^+\pi^-\pi^0$	0.001	–	0.001
	$e^+\nu_e\pi^0\pi^0\pi^0$	0.001	–	0.001
	$\mu^+\nu_\mu\bar{K}^0$	0.035	0.067±0.035	0.035
	$\mu^+\nu_\mu\bar{K}^{*0}$	0.030	0.045±0.006	0.045
	$\mu^+\nu_\mu\bar{K}^0\pi^0$	0.015	–	0.015
	$\mu^+\nu_\mu K^-\pi^+$	0.015	0.032±0.017	0.015
	$\mu^+\nu_\mu K^-\pi^+\pi^0$	0.044	–	0.044
	$\mu^+\nu_\mu\bar{K}^0\pi^+\pi^-$	0.022	–	0.022
	$\mu^+\nu_\mu\bar{K}^0\pi^0\pi^0$	0.022	–	0.022
	$\mu^+\nu_\mu\pi^0$	0.001	0.0057±0.0022	0.0057
	$\mu^+\nu_\mu\eta$	0.001	–	0.001
	$\mu^+\nu_\mu\eta'$	0.001	–	0.001
	$\mu^+\nu_\mu\rho^0$	0.001	$0.002^+0.0015_{-0.0013}$	0.001
	$\mu^+\nu_\mu\omega$	0.001	–	0.001
	$\mu^+\nu_\mu\pi^+\pi^-$	0.001	–	0.001
	$\mu^+\nu_\mu\pi^0\pi^0$	0.001	–	0.001
	$\mu^+\nu_\mu\pi^+\pi^-\pi^0$	0.001	–	0.001
	$\mu^+\nu_\mu\pi^0\pi^0\pi^0$	0.001	–	0.001

Table 4.5: Branching ratio of D^+.

Decay Channel	Lund7.3 (%)	PDG '94(%)	Corr. Factor	Adopted for MC (%)
$D_s \rightarrow$				
eX	0.1287	< 20	1.	0.1287
μX	0.1287	–	1.	0.1287
Hadronic	0.8460		1.	0.8460
Total	1.1034			1.1034
$D^0 \rightarrow$				
eX	0.1000	7.7±1.2	0.8218	0.0822
μX	0.0940	10.0±2.6	0.8742	0.0822
Hadronic	0.8460		1.	0.8460
Total	1.0400			1.01035
$D^{\pm} \rightarrow$				
eX	0.2147	17.2±1.9	0.7534	0.1618
μX	0.2117	–	0.7641	0.1618
Hadronic	0.6160		1.	0.6160
Total	1.0424			0.9395

Table 4.6: The branching ratio of D$\rightarrow \ell$X and correction factor.

Process	Cross section (pb)
$e^+e^- \rightarrow e^+e^-bb$	0.474
$e^+e^- \rightarrow e^+e^-\tau^+\tau^-$	188.8
$e^+e^- \rightarrow \tau\tau(\gamma)$	37.9
$e^+e^- \rightarrow q\bar{q}$ (udscb)	163.2

Table 4.7: The cross sections for background process.

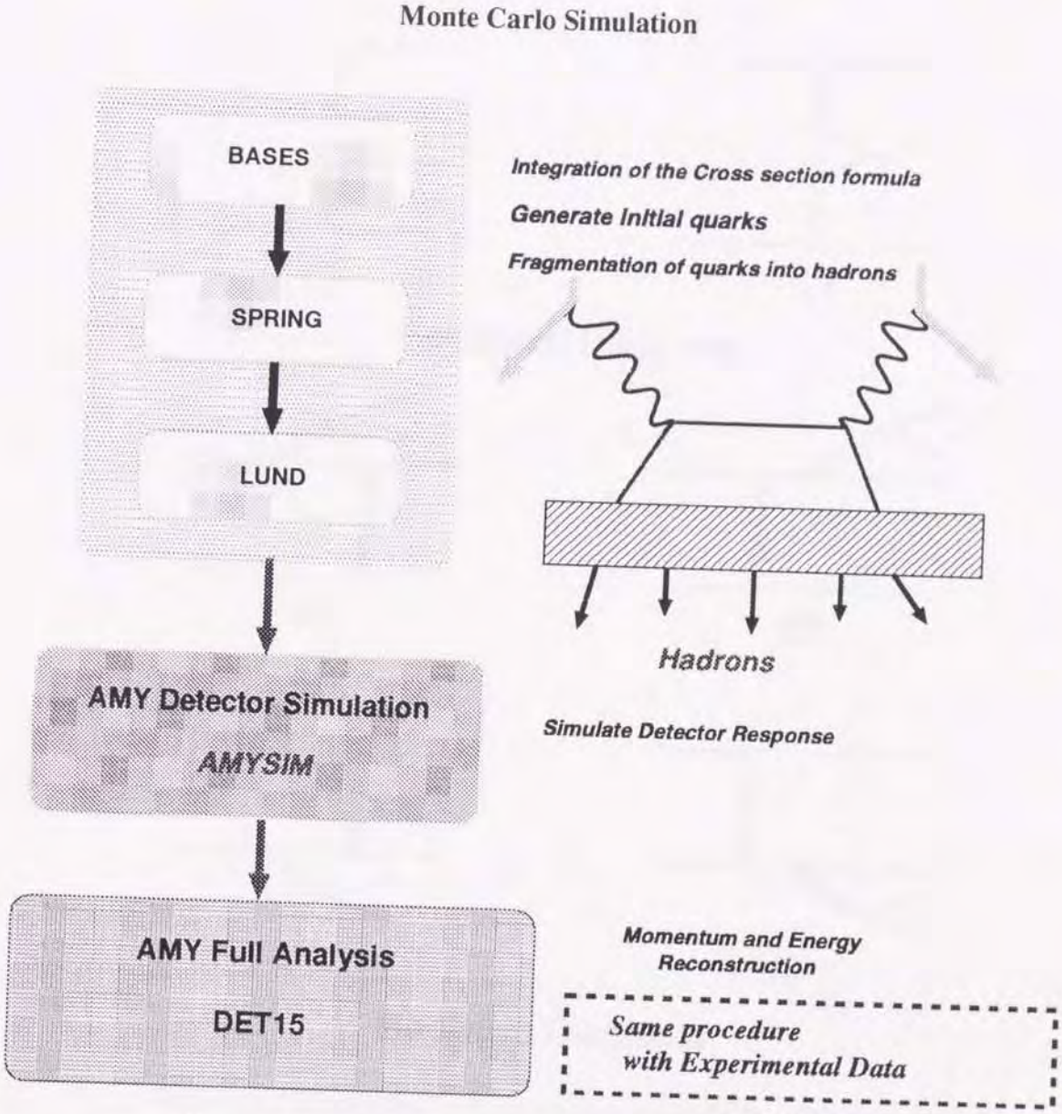

Figure 4.1: The basic procedure of the Monte Carlo Simulation.

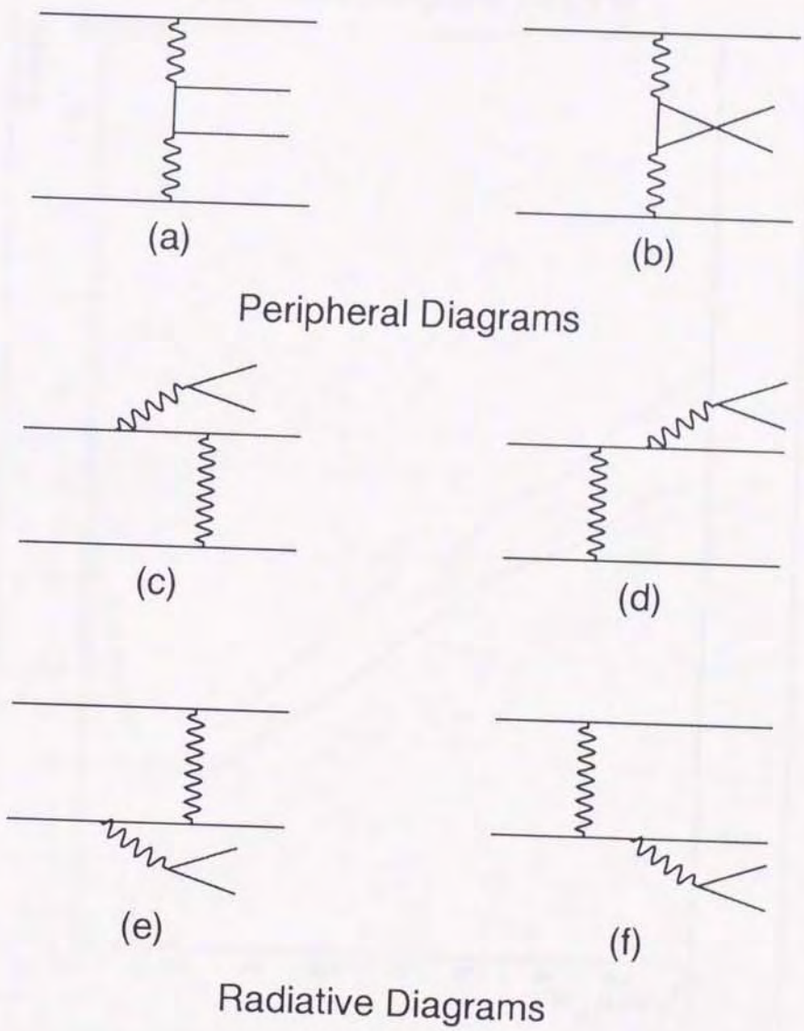

Figure 4.2: The peripheral and the radiative diagrams for QPM process.

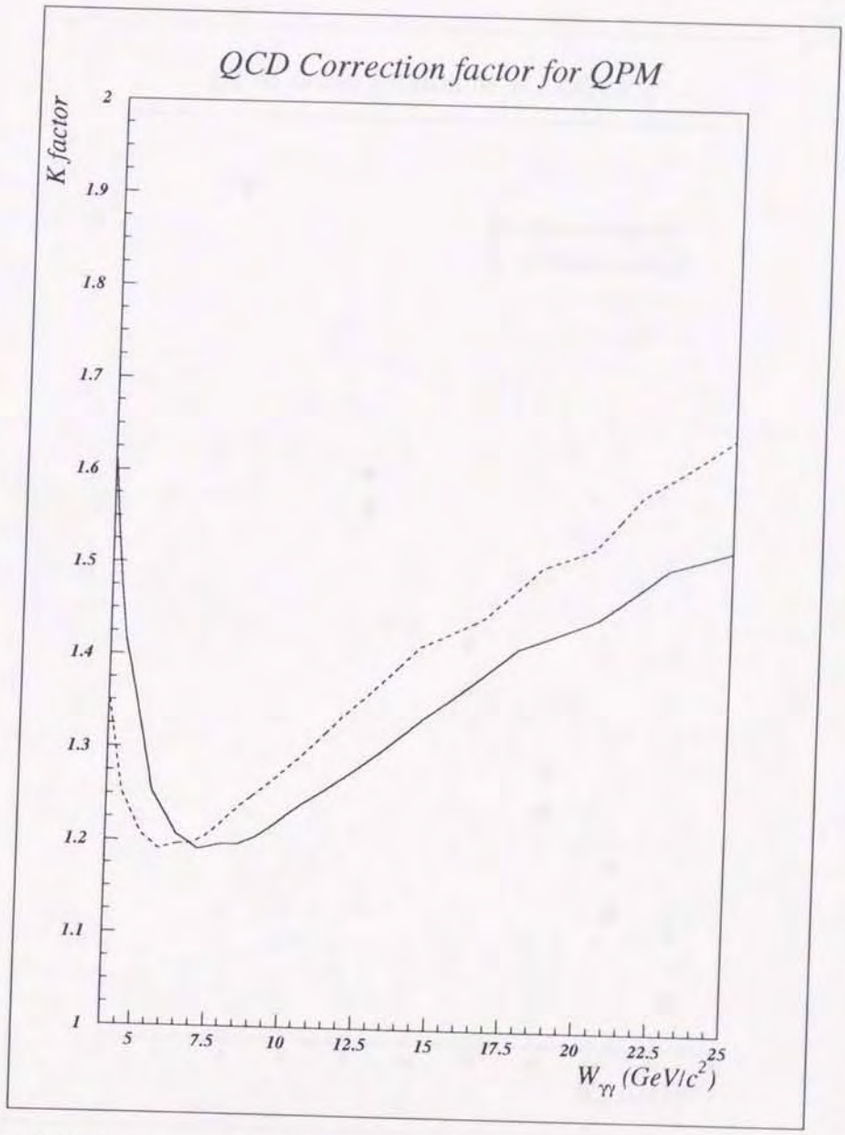

Figure 4.3: The NLO QCD correction factor (K) for direct process as a function of invariant mass of the hadronic system ($W_{\gamma\gamma}$). The solid and dashed lines show for 1.6 GeV/c^2 and 1.3 GeV/c^2 of charm mass, respectively.

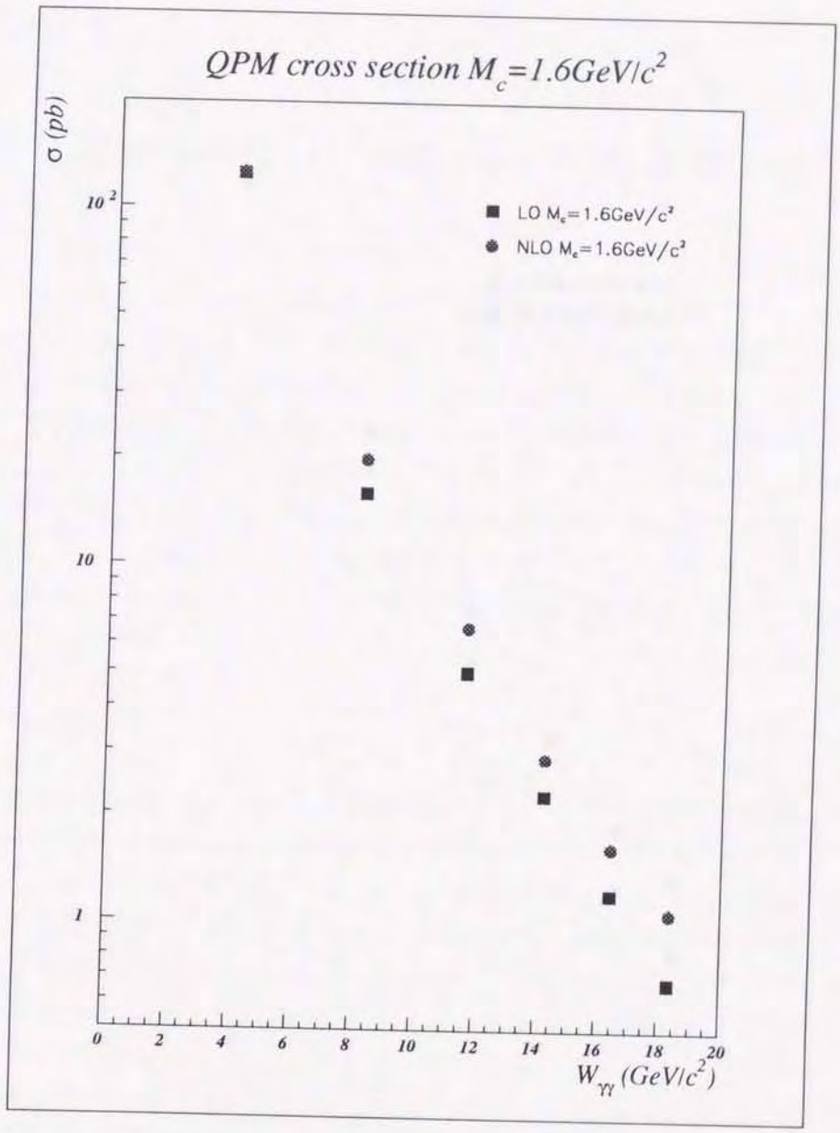

Figure 4.4: The cross section of direct process as a function of $\gamma\gamma$ invariant mass($W_{\gamma\gamma}$). The mass of charm quark is 1.6 GeV/c^2.

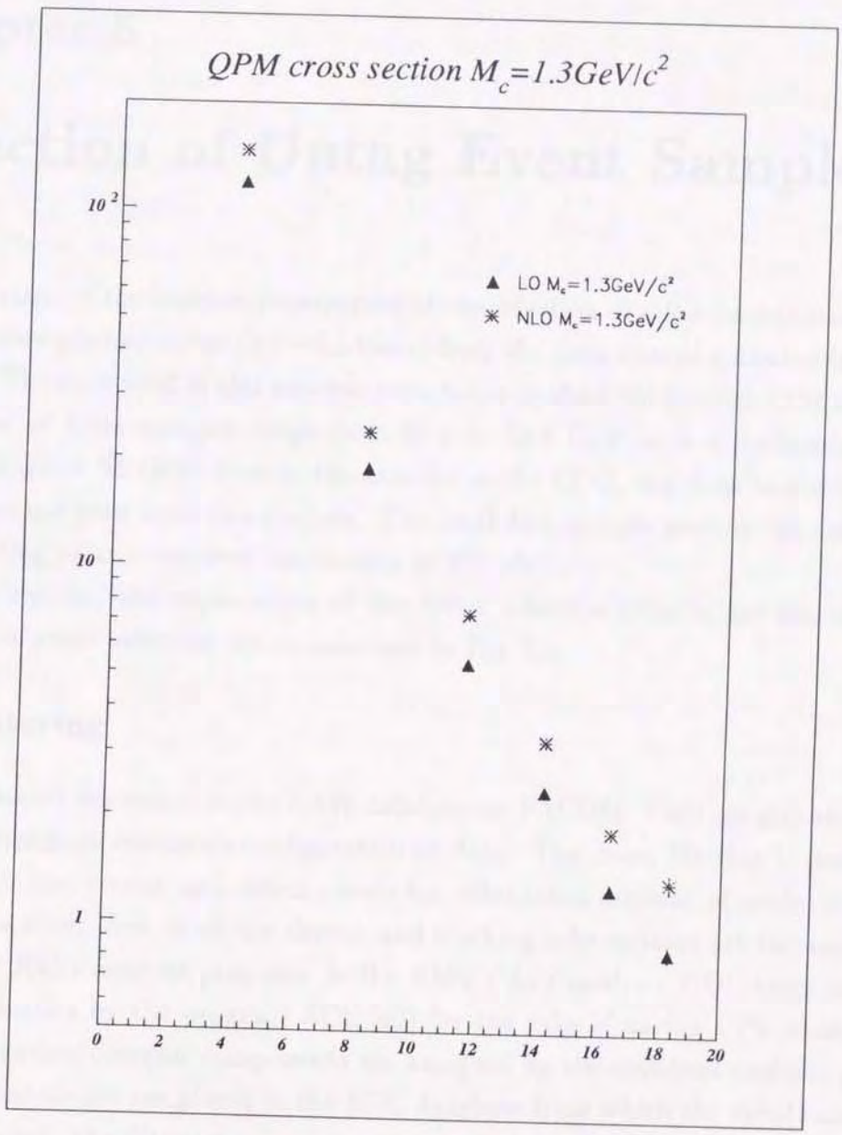

Figure 4.5: The cross section of direct process as a function of $\gamma\gamma$ invariant mass($W_{\gamma\gamma}$). The mass of charm quark is 1.3 GeV/c^2.

Chapter 5

Selection of Untag Event Sample

The first stage of the analysis constructed of the selection of a low background sample of untagged two-photon events ($\gamma\gamma \rightarrow$hadrons) from the data sample collected by the AMY detector. The data used in this analysis were taken in the 1990 through 1994 run periods. The center of mass energies range from 57.4 to 59.4 GeV with a luminosity-weighted average of $\sqrt{s} = 58$ GeV. Due to the trouble in the CDC, the data taken in 1991 run period were not used from this analysis. The total data sample used in this analysis, thus corresponding to an integrated luminosuty of 275 pb^{-1}.

In this section, the explanation of the event selection criteria are described. The procedure of event selection are summarized in Fig. 5.1.

5.1 Filtering

Triggered events are stored in the RAW database on FACOM. They are gigantically large and somtimes have erroneous configuration of data. The event filtering is performed to discard such bad events, and select events for substantial amount of analysis. In order to judge the event, first of all the shower and tracking informations are reconstructed by using AMY *FAST* analysis program. In the AMY *FAST* analysis, CDC tarck reconstruction is performed by the program ACE [43] for the sake of saving CPU time, and the signals from other detector components are analyzed by the standard analysis programs. Reconstructed events are placed in the REC database from which the events are selected and categolized. The filtering process is comprised of two stages.

The first stage event filter consists of vetoing events due to noisy signals and selecting events by *FAST* analysis results. Vetoing conditions are basically done by looking at fire channels in raw data. In the case of SHW which is the analysis for the reconstruction of shower cluster in SHC, if the energy deposit was too high in both of raw data and

reconstructed shower, the SHW signal is vetoed. The event selection at this stage is made by sets of combination of the flags, as which the signals of each detector compornents are roughly classified.

At the second stage event filter, the events passed the first stage event filter are categolized into five data samples, 1)HAD which contains events likely to arise from hadronic production, 2)LWM which contains events with a low multiplicity of charged tracks, 3)QED which contains events likely to arise from QED process, 4)ELW which contains events likely to arise from electroweak process, 5)PTC which contains events with large hits in the ESC. These data samples are partly overlapping. Any event selected for one or more of these data samples is also placed in DST (Data Summary Tape). The details of selection criteria of those data samples are tabulated in Table 5.1.

HAD
$N_{cdc} \geq 3$
with $\Delta R < 5$ cm
$\Delta Z < 10$ cm
$\chi^2 \leq 10000$
$E_{SHW} > 2.8$ GeV or $E_{ESC} > 3$ GeV

LWM
$N_{cdc}(p \geq 0.75\ \text{GeV}) \geq 2$
with $\Delta R < 2 + \cot\theta$ cm
$\Delta Z < 10 + 5\cot\theta$ cm
$\chi^2 \leq 75$

QED
$N_{cdc}(p > 5\text{GeV}) \geq 1$
$N_{cdc} \leq 10$
with $\Delta R < 2$ cm
$\Delta Z < 10$ cm
$N_{AX} > 9$
$N_{ST} > 6$
Not Cosmic
defined as $N_{MUO} < 1$ and ($t_\mu < -6$ or $t_\mu > 40$ns)
or $N_{SHW}(E_{SHW} > 3\ \text{GeV}) < 2$ and $N_{SHW}(E_{SHW} > 5\ \text{GeV}) < 1$

ELW
LWM
and $2 \leq N_{cdc}(p \geq 1.0\ \text{GeV}) \leq 6$
with $\Delta R < 3$ cm
$\Delta Z < 5$ cm
$N_{ST} \geq 3$

PTC
ESC back-to-back track
with $N_{ESC} \leq 15$
ADC(Front) > 100
ADC(Rear) > 100
ADC(Front+Rear) > 2000
$N_{ESC}^{Junk} \leq 8$
ADC(Front+Rear) > 4000

DST
HAD∪LWM∪QED∪ELW∪PTC

CDC		
Number of axial wire hits	N_{AX}	≥ 6
Number of stereo wire hits	N_{ST}	≥ 4
Chisquare of fitting to a helix	$\chi_{r-\phi}$	< 16
	χ_z	< 16
Dsitance between interaction point and track origin	ΔR	≤ 18.0 cm
	ΔZ	≤ 18.0 cm
Momentum of the tarck	p	$<0.8E_{beam}$
Polar angle of the track	$20° \leq \theta \leq 160°$	

Table 5.1: Definition of good charged track used in preliminary event selection.

5.2 Preliminary Event Selection

In order to get hadronic untagged two-photon events, we first selected events from DST by requiring the number of charged tracks in CDC to be greather than or equal to three. Here the definition of good charged tracks are shown in Table 5.1. The criteria applied in the preliminary selection is expected to reduce the size of event sample to manageable size while keeping selection efficiency high for the events with hadronic final states.

At the filtering stage, the *FAST* analysis program ACE was used for CDC to reconstruct charged tracks. However the analysis for reconstruction of tracks by the program DUET [44] is desirable. DUET can reconstruct charged tracks in CDC more precisely and efficiently than ACE does, while it takes more CPU time for the calculation. In the hadronic untagged two-photon events, the visible energy and multiplicity of produced hadrons are rather small, so that the efficiency of track reconstruction has to be high enough. This is because the events which passed preliminary event selection are then re-analyzed with the *FULL* analysis program. It perform DUET for CDC analysis, and the standard analysis program for other detector components.

The fully re-analyzed data is subjected to the hadronic two-photon event selection.

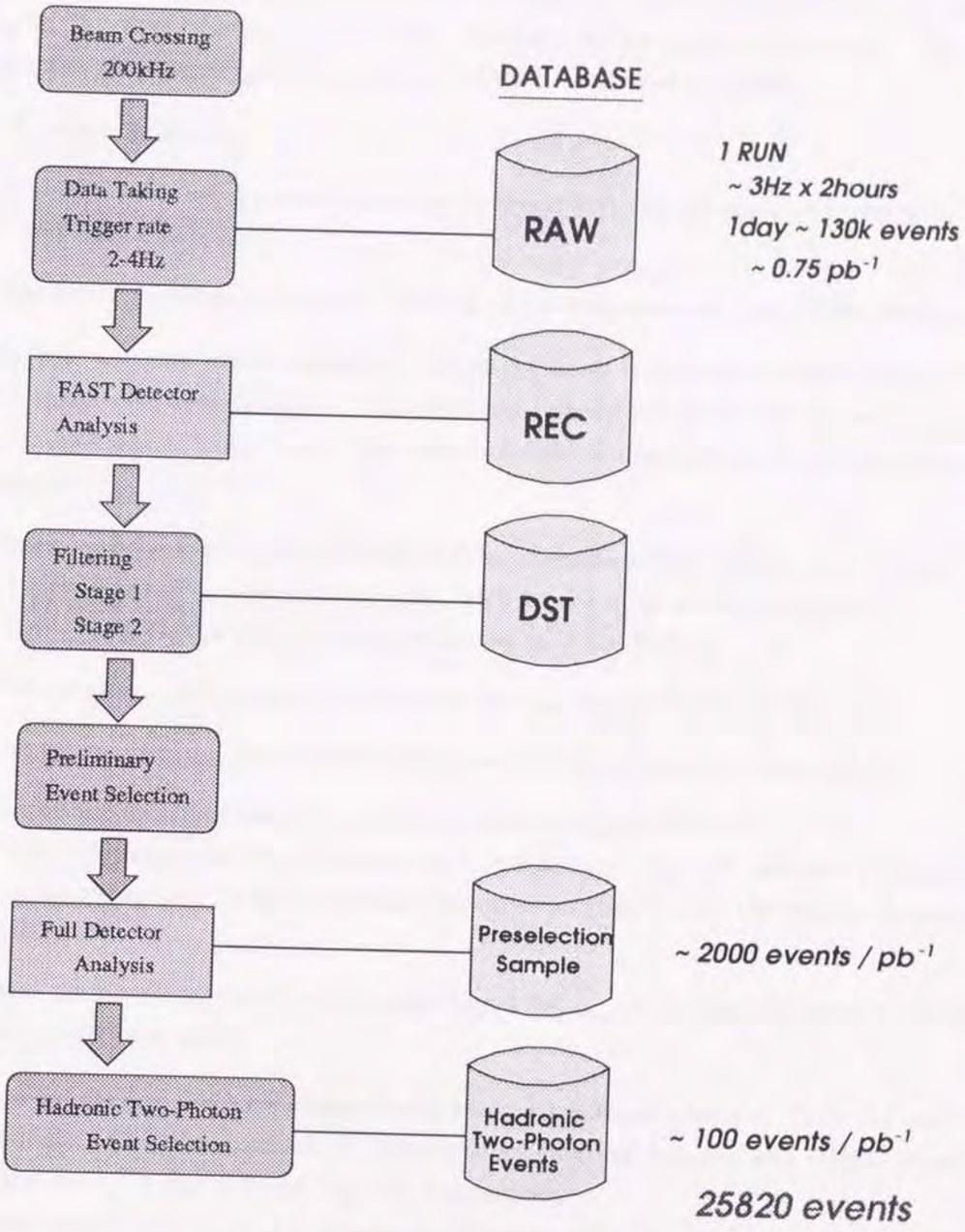

Figure 5.1: The procedure of event selection.

5.3 Event Selection of Hadronic Two-Photon events

A philosophy of the event selection for untagged two-photon hadronic events are very simple. It should belong to the event topology we are interested in now. The event topologies of the untagged two-photon hadronic events are as follows:

1) Hadronic final state.

2) A small visible energy since the outgoing beam particles are scattered very small angle and escape detection.

3) The beam particle, i.e energitic electron or positron, are not seen in the detector.

As well as these event topologies, the background from other physical channels has to be taken into consideration. The selection criteria are thus well-tuned to yeild the maximum signal to noise ratio. The selection criteria imposed to the pre-selection data sample are:

1) There must be five or more charged tracks originating from within r= 4 cm and $|z|$=10 cm of the interaction point, with two or more of these having $|p| \geq 0.75$ GeV/c and at least one having $p_t \geq 1.0$ GeV/c.

2) The net charge of the good tracks must have an absolute value of 2 or less.

3) The net momentum transverse to the beam direction must be ≤ 5.0 GeV/c.

4) The visible invariant mass W_{vis} must lie between 4 and 20 GeV.
The calculation of W_{vis} includes both charged and neutral particles measured by the barrel tracker (CDC), the barrel calorimeter (SHC), and the endcap calorimeter (ESC).

5) There are no clusters with energy exceeding $0.25E_{beam}$ in the electromagnetic calorimeters (SHC and ESC).

Here we defined the good charged and neutral tracks as shown in Table 5.2 and 5.3, respectively. The distributions of transverse momentum balance and visible invariant mass are shown in Fig. 5.2 and Fig. 5.3, respectively.

Requirement 1) is applied to ensure good trigger efficiency, since requirements of the major trigger for two-photon events are combination of ITC tracks, CDC tracks, and minimum ionizing particle in SHC (Trigger 13). Reqirement of charged multiplecity rejects QED-type events such as $e^+e^- \rightarrow e^+e^-\tau^+\tau^-$ (Fig. 5.4), where the final state τ's decay

into hadrons. Requirements 2) and 3) reduce the number of events coming from the interactions of beam particles with the residual gas in the vacuum chamber (beam-gas events) or the atomic nuclei of the material of the beam pipe (beam-wall events). Requirement 4) suppresses backgrounds from single-photon hadronic annihilations (Fig. 5.5). Finally, 5) ensures that the two interacting photons were almost real (anti-tag condition). This condition limits the corresponding polar angle for the scattered electron to be $|\cos\theta| \geq 0.97$. Basically, these criteria follow the one used in the analysis of hadronic photon-photon interactions done by AMY [42]. Our "untag event sample" contains the 25820 events that pass the above cuts. Fig. 5.6~ 5.10 shows examples of a typical hadronic events detected by AMY.

CDC		
Number of axial wire hits	N_{AX}	≥ 8
Number of stereo wire hits	N_{ST}	≥ 5
Chisquare of fitting to a helix	$\chi_{r-\phi}$	< 8
	χ_z	< 8
Distance between interaction point and track origin	ΔR	≤ 4.0 cm
	ΔZ	≤ 10.0 cm
Maximum momentum of the tarck	p	$<0.8E_{beam}$

Table 5.2: Definition of good charged track used in selection of untagged two-photon hadronic events.

SHC
• For the SHW cluster without matched CDC track within $2° \times 2°$ window.
$E_{Cluster} > 0.5$ GeV
$E^{Segment}_{Cathode} < 0.95E_{Cluster}$
• For the SHW cluster with matched CDC track.
$E_{Cluster} > 1.0$ GeV
$E^{Segment}_{Cathode} < 0.95E_{Cluster}$
$E^{layer}_{Anode} < 0.8 \sum E^{layer}_{Anode}$

ESC
$E_{Cluster} > 0.5$ GeV
ADC hits are presented on both front and rear sintillator.

Table 5.3: Definition of good neutral track used in selection of untagged two-photon hadronic events.

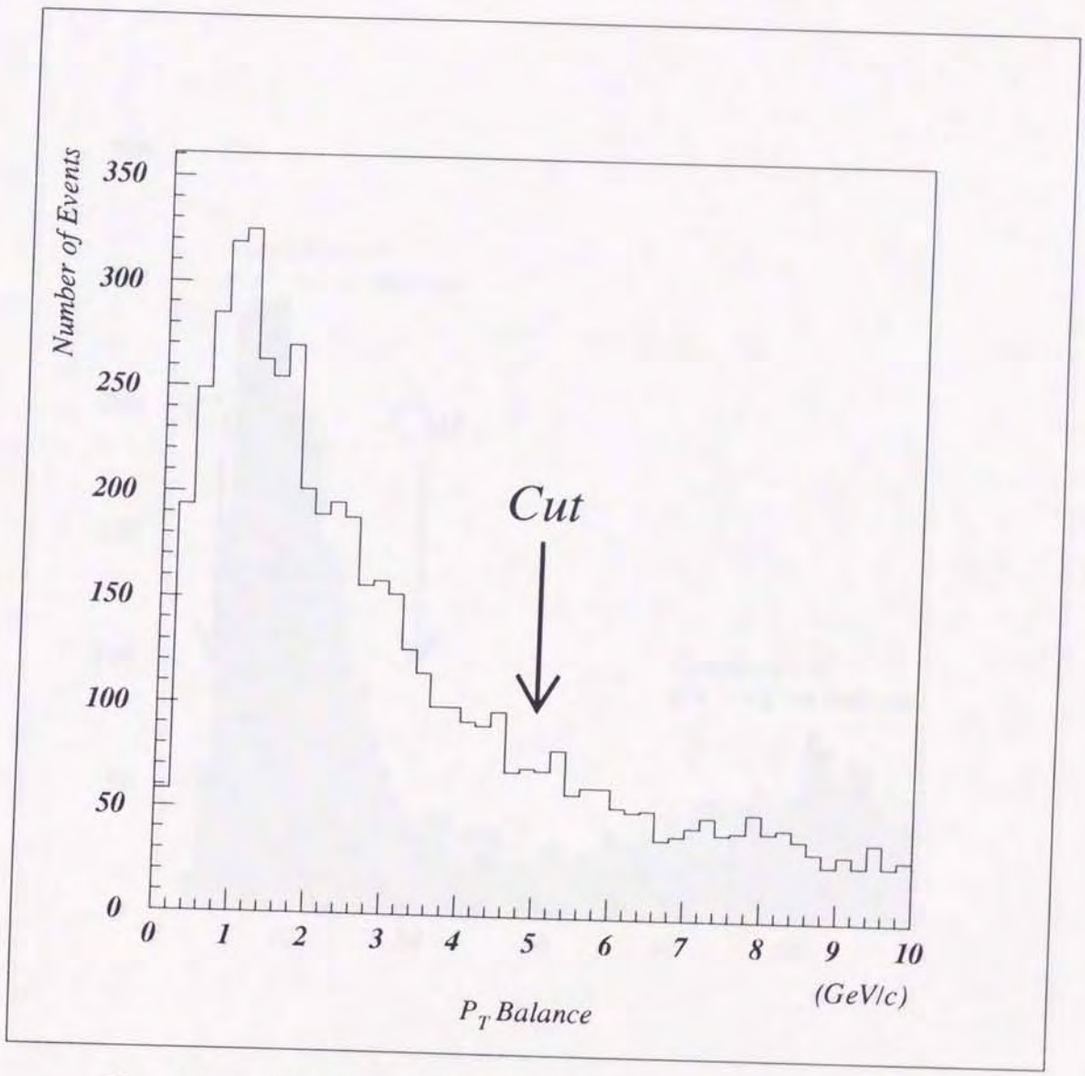

Figure 5.2: P_T balance distribution after requiring selection criteria 1) and 2).

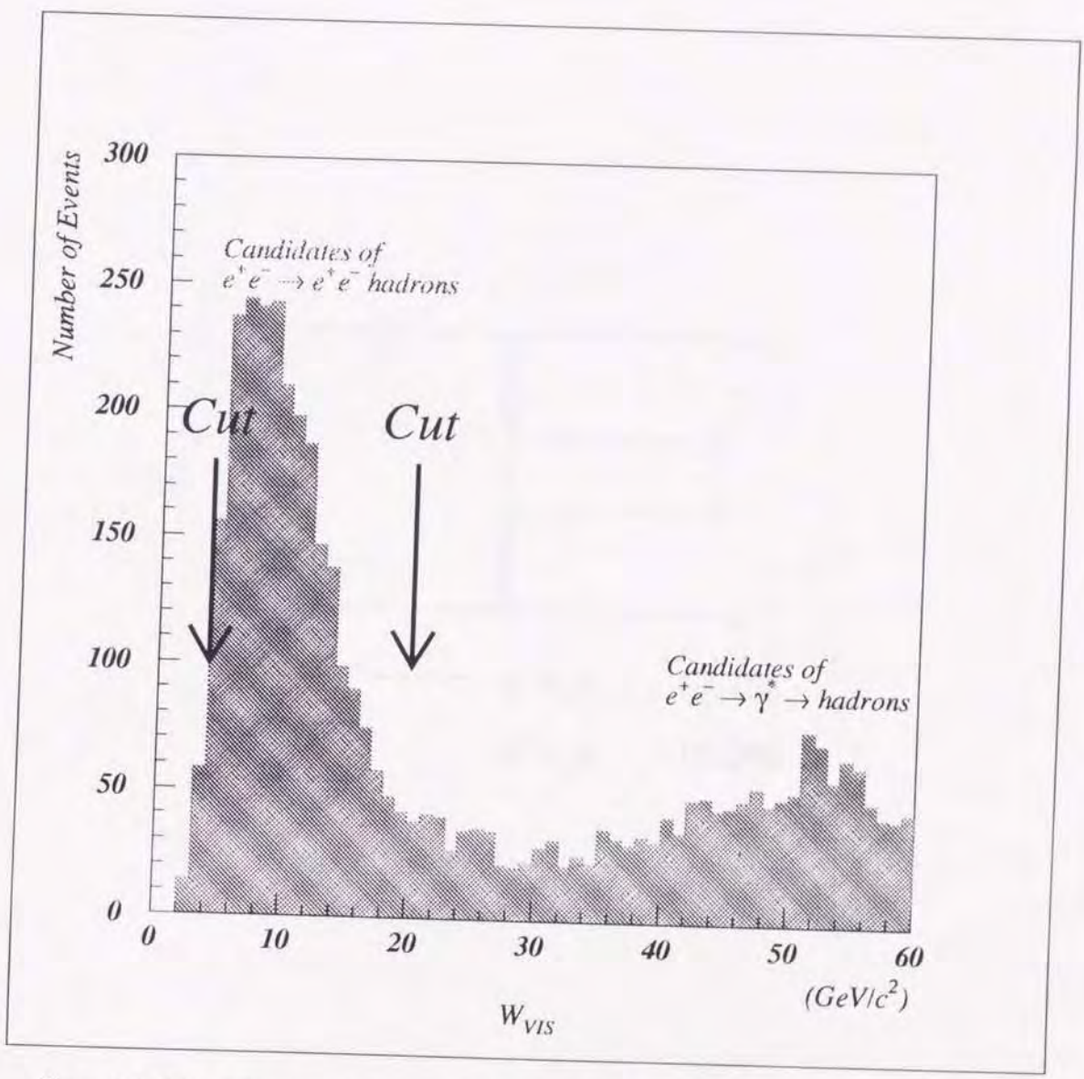

Figure 5.3: The visible invariant mass distribution after requiring selection criteria 1) $\sim$ 3).

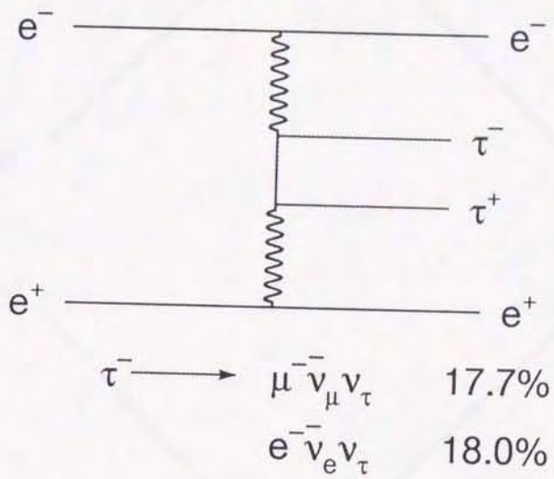

Figure 5.4: Diagram of $e^+e^- \to e^+e^-\tau^+\tau^-$ process.

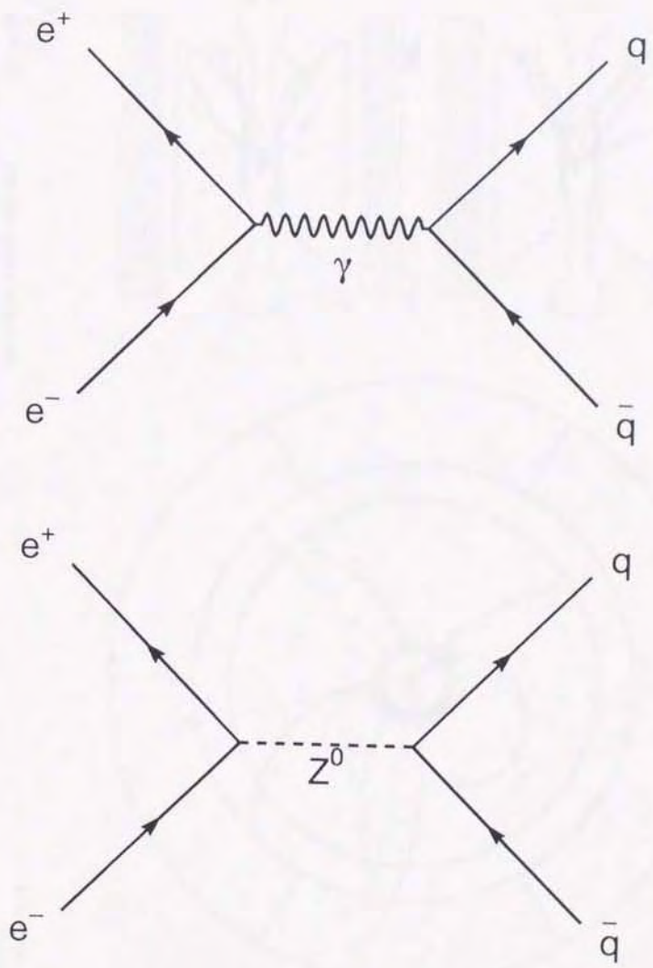

Figure 5.5: Diagrams of $e^+e^- \rightarrow q\bar{q}$ process.

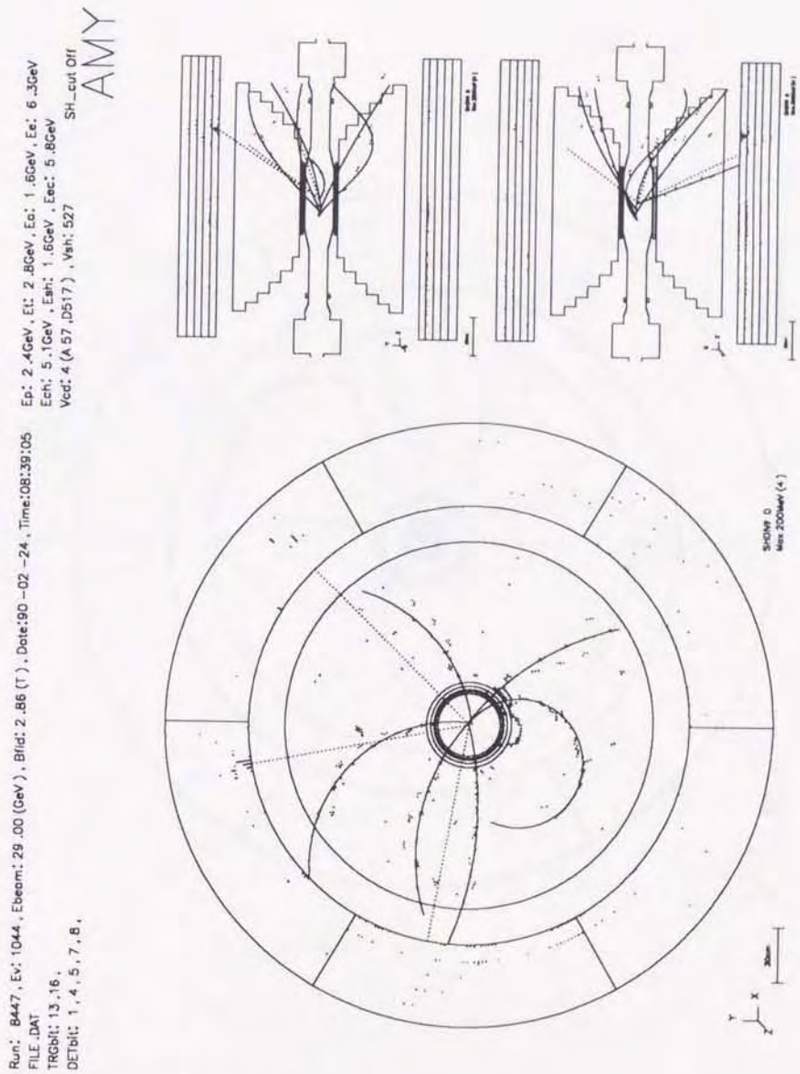

Figure 5.6: Untagged two-photon event.

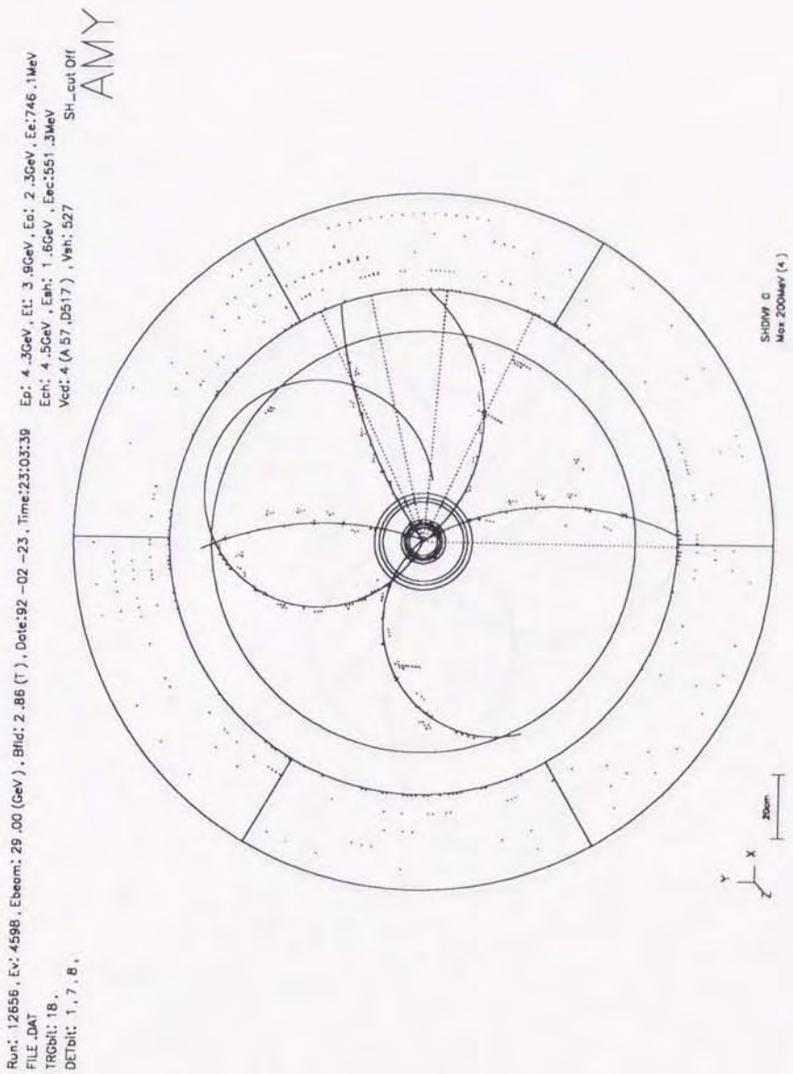

Figure 5.7: Untagged two-photon event.

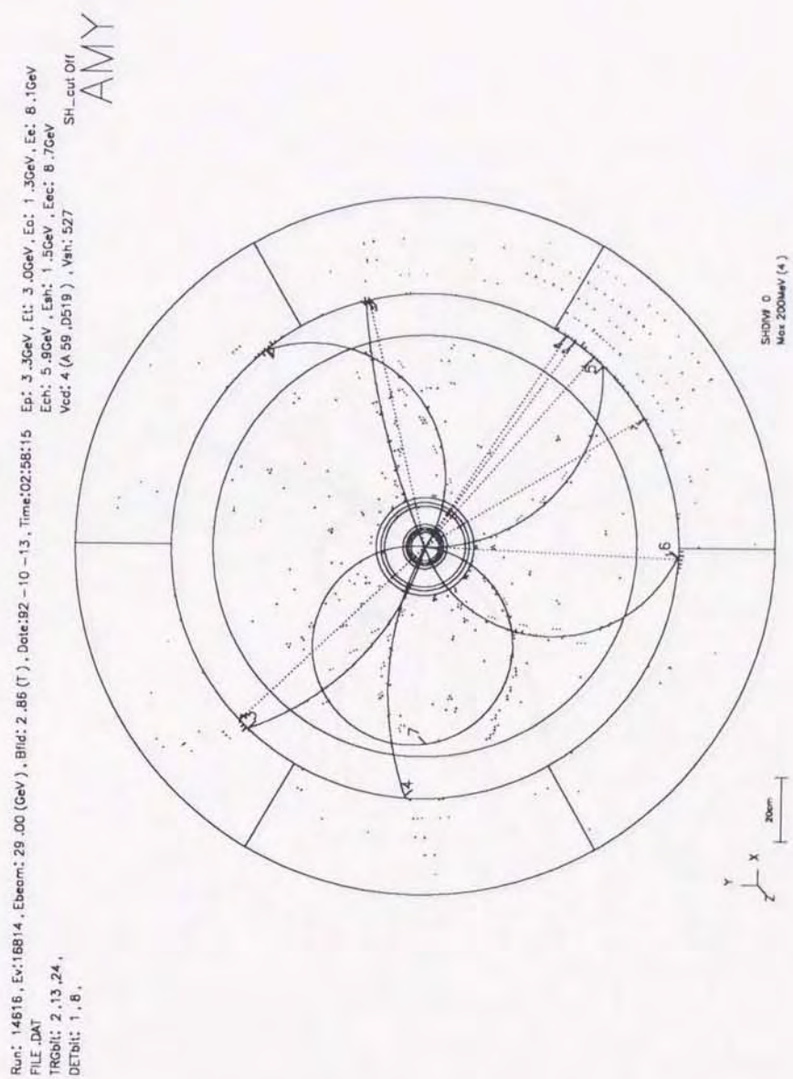

Figure 5.8: Untagged two-photon event.

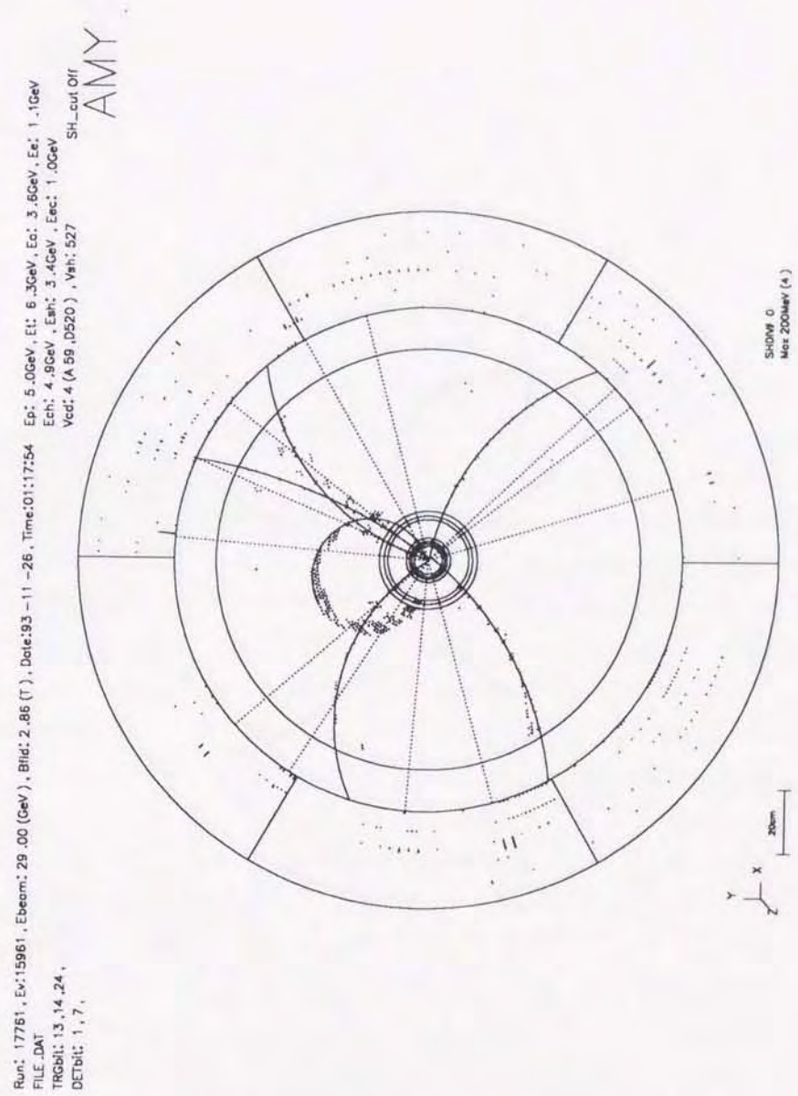

Figure 5.9: Untagged two-photon event.

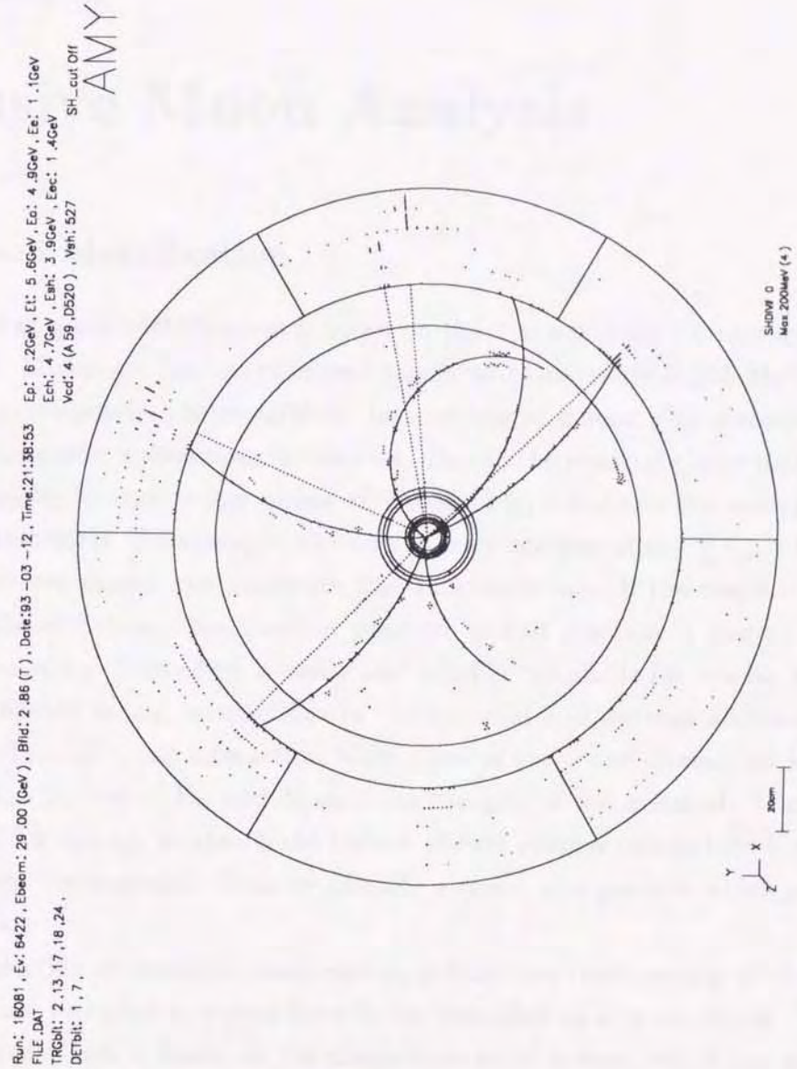

Figure 5.10: Untagged two-photon event.

Chapter 6

Inclusive Muon Analysis

6.1 Muon Identification

The method of muon identification is based on the characteristics of interaction of muons in meterials. Muons are leptons of second family and have mass of 105 MeV and lifetime of 2.197 μs corresponding to $c\tau$=659 m. Interactions of muons with materials occurs via only electromagnetic interactions in this case. Due to the relatively large mass, the energy loss is caused by ionization loss unlike electrons. Fig. 6.1 shows the energy loss rate in the various materials. For example, muons loss their energies about $\frac{dE}{dx}|_{\rm min}$=11.6 MeV/cm for Fe. Therefore muons can penetrate the thick materials. If the magnetic field is not presented, the deviation from incident position to exit position is due to the multiple Coulomb scattering. This effect is easily and reliably calculable for muons. On the other hand, the hadrons repeat interactions in the material and develop a shower via strong interaction. Typically, one interaction takes place in every one interaction length, which is about 17 cm in case of Fe, and deposits its energies in the material. Therefore, if the material is thick enough to absorb the hadron shower process completely, hadrons do not come out from the material. Thus we identify a muon as a particle which penetrate the thick material.

For the selection of inclusive muon events, at least one track among all charged tracks of the hadronic two-photon events have to be identified as a muon track. The method of muon identification is based on the characteristics of muons, which can penetrate the thick meterial without hadron interaction.

6.2 Muon Selection

We select muons in the momentum range $2.0 \leq p \leq 5.0$ GeV/c . They are identified as charged tracks in the CDC that match to hits in any three of the four muon

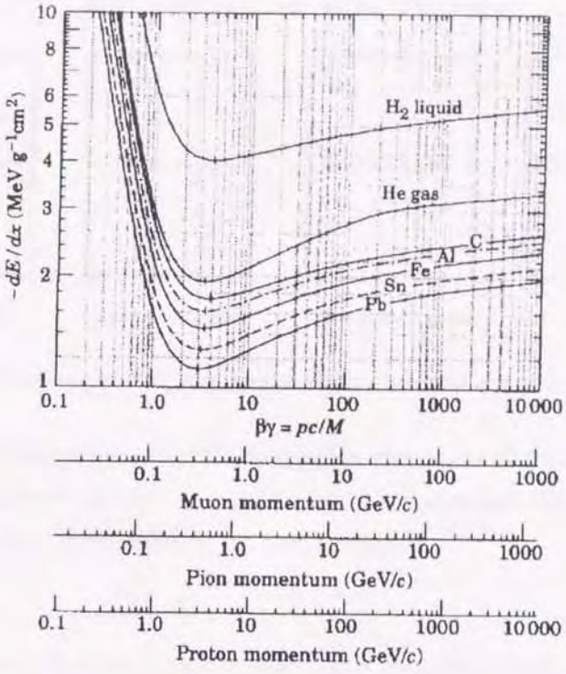

Figure 6.1: Energy loss rate.

chamber (MUO) layers (Fig. 6.2) covering $|\cos\theta| < 0.74$. To reduce backgrounds from hadron fakes, we require that the matching distance between the hits and the extrapolated track be less than twice the mean deviation expected from multiple Coulomb scattering (Fig. 6.3). Most cosmic ray events are rejected by requiring that the muon scintillation counter time relative to the beam crossing is in the range $0 < t_\mu < 35$ ns. The remaining cosmic ray events are rejected by a visual scan (Fig. 6.4). The efficiency of muon identification is estimated by a Monte Carlo simulation and found to be 40%.

A total of 32 events from the untag event sample satisfy the inclusive muon criteria. No events containing two or more muons were found.

6.3 Muon Backgrounds Estimation

Background from multihadronic single-photon annihilation is estimated to be 1.9±1.3 events from a Monte Carlo simulation of this process using the JETSET7.3 generator [32]. Contaminations from $e^+e^- \to e^+e^-\tau^+\tau^-$ and $e^+e^- \to e^+e^-b\bar{b}$ proceses are estimated to be 2.4±1.4 and 1.2±0.2 events, respectively, from Monte Carlo simulations of these processes.

In bonafide two-photon events, the fake muon signal arises principally from hadron

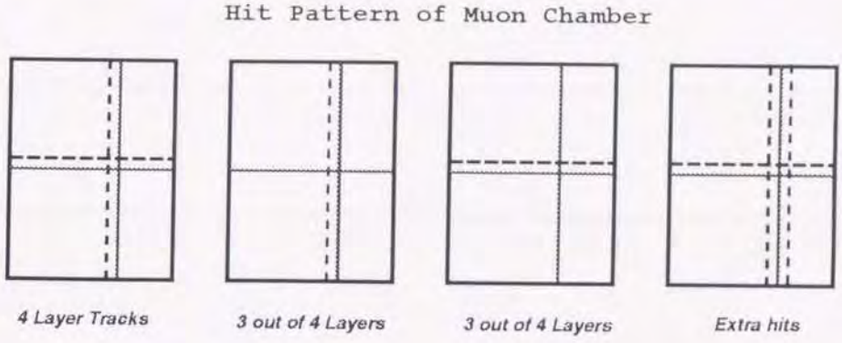

Figure 6.2: Combinations of wire layers which make track in muon chamber.

showers in the hadron filter, where the debris reaches the muon chamber ("punchthrough"), or from decay-in-flight of $\pi^{\pm}$ and $K^{\pm}$ mesons to muons that reach the muon chamber ("decay"). These backgrounds were studied by two methods.

1) Monte Carlo simulation

The backgrounds due to decay-in-flight and punchthrough of hadrons were estimated from Monte Carlo event samples for $e^+e^- \rightarrow e^+e^- +$ hadrons. The amount of background estimated by Monte Carlo was normalized to the data by demanding that the number of Monte Carlo tracks match the number of observed tracks in the untag event sample. We assumed following relation,

$$N^{FAKE} = N_{trk}^{EXP} \cdot \sum \sigma_{MC}^{eff} R_{MC}^{fake} \tag{6.1}$$

where N_{trk}^{EXP} is the number of tracks in the untag event sample. σ_{MC}^{eff} and R_{MC}^{fake} are calculated from Monte Carlo events of two-photon processes. Those represent effective cross section of each processes and ratio of the fake lepton tracks to all tracks. The summation was performed for VMD, QPM, and Resolved photon processes.

2) Analytical calculation

The background level was also estimated by calculating the probabilities of decay and punchthrough for each charged particle in the untag event sample, using a momentum-dependent analytical formula for the decay and punchthrough probabilities.

The background from punchthrough is estimated with the emprical formula from the experiment of Ref. [45]. The results in Ref. [45] are extrapolated to our momentum region. The probability of punchthrough is written approximately as:

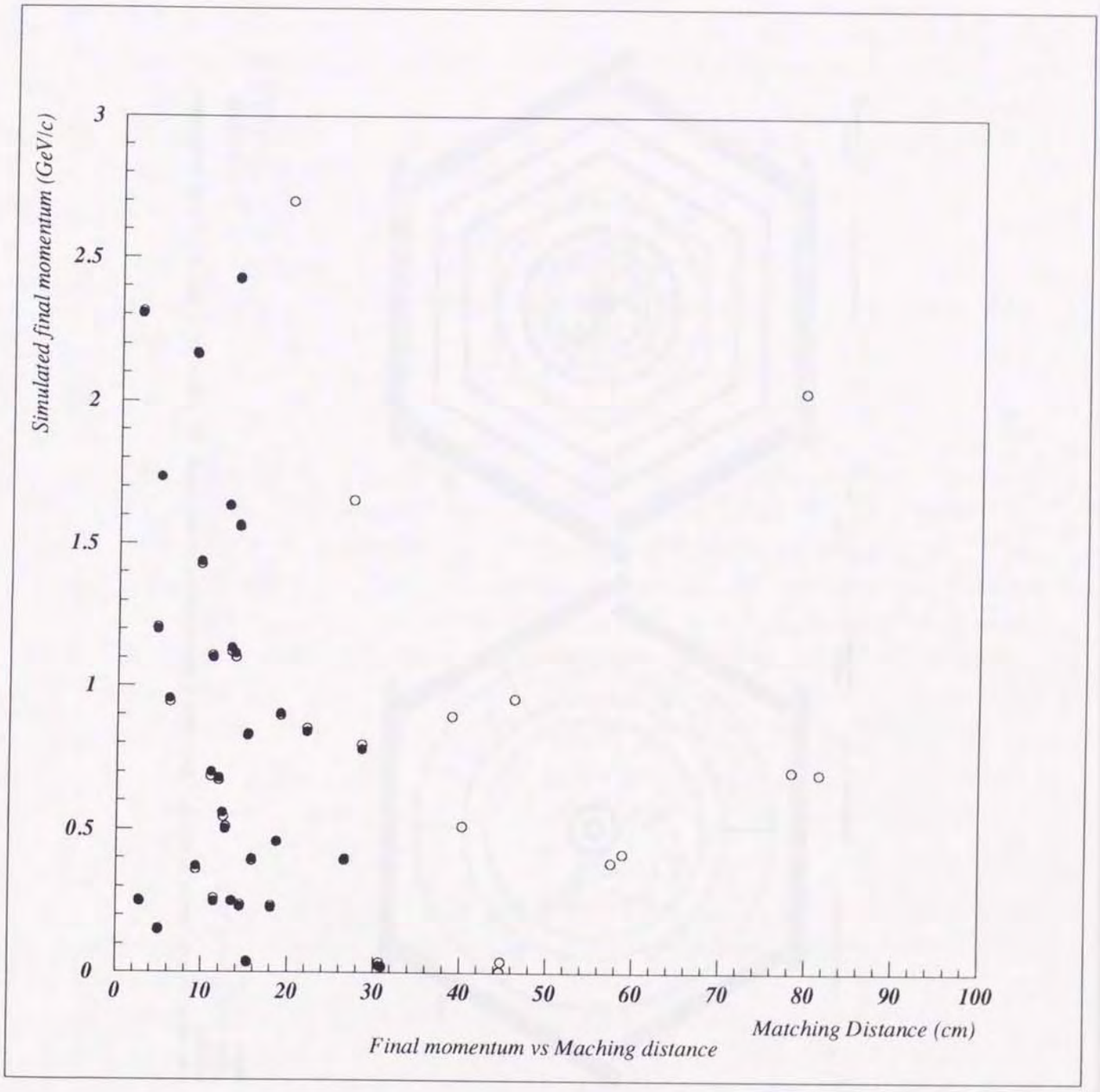

Figure 6.3: Maching destance versus simulated final momentum. The events shown in closed circles were candidates of muon track which passed 2σ matching distance cut.

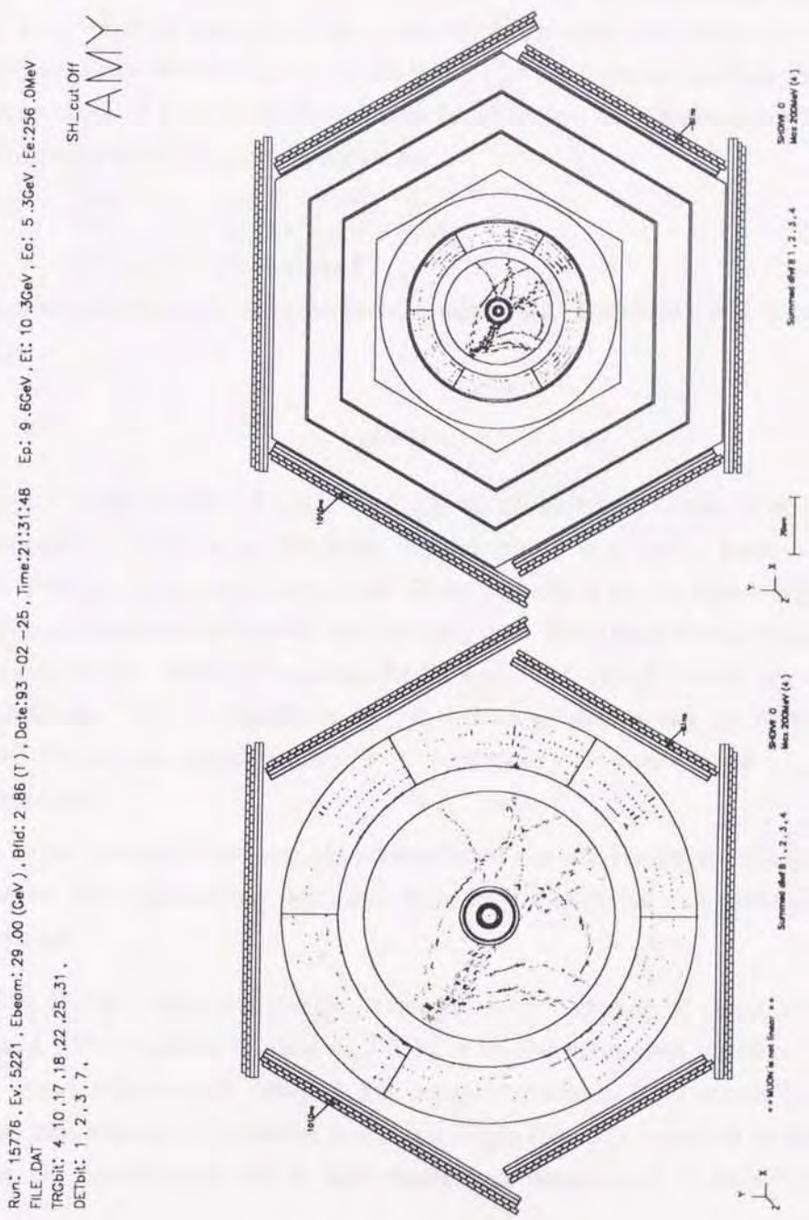

Figure 6.4: An event rejected as cosmic ray event by eye scanning.

$$P^{punch} = \left(p - \frac{P_{cut}}{\sin\theta}\right) e^{-0.046T} \tag{6.2}$$

where T is the thickness of iron absorber in cm. θ is the polar angle of the track and $P_{cut}/\sin\theta$ is the minimum momentum needed for muon to reach the muon chamber. Here we set $P_{cut} = 1.9$ GeV/c. The thickness of hadron absorber in AMY is equivalent to 1.65 m thickness iron in average. The dependency of the thickness to the polar angle is approximated as

$$\begin{aligned} T &= 155 && (\cos\theta < 0.48) \\ &= 175 && (0.48 < \cos\theta < 0.56) \\ &= 153/\sin\theta && (0.56 < \cos\theta) \ . \end{aligned}$$

The decay of π and K are estimated analyticaly. The decay will occur in the probability,

$$P^{Decay} = 1 - e^{-\lambda/\lambda_0} \tag{6.3}$$

where λ is the length of path through which hadron travels, and λ_0 is defined as $\lambda_0 = \gamma\beta c\tau$. The decay lifetimes ($\tau$) for pions and kaons have been used along with a decay path length equal to 73 cm, which is about inner edge of SHC. The branching ratios, kinematical limitations, and pion/kaon fraction are multiplied to the probability. Here we assume 82 % and 15 % of all tracks are pion and kaon, respectively. The probabilities of punchthrough and decay-in-flight are calculated for all the tracks which satisfy $2 \leq p \leq 5$GeV/c and $|\cos\theta| \leq 0.74$ and then summed up.

The decay probabilities are thus calculated for all tracks in untag event sample. However, this calculation does not include the effect of the matching distance requirement.

If, in the Monte Carlo simulation, the matching distance of the MUO hits with an extrapolated CDC track is relaxed to $|d| \leq 1$ m the estimated numbers of background events by these independent methods are consistent within their errors (Fig. 6.5). When the tighter, two standard deviation matching requirement is imposed in the Monte Carlo simulation, the background due to fake muons was determined to be 8.0±1.1 events.

6.4 Summary of Muon Analysis

After subtracting the background contributions, 18.5 ± 6.1 inclusive muon events remain. The examples of inclusive muon events are shown in Fig. 6.6~ 6.11. The results

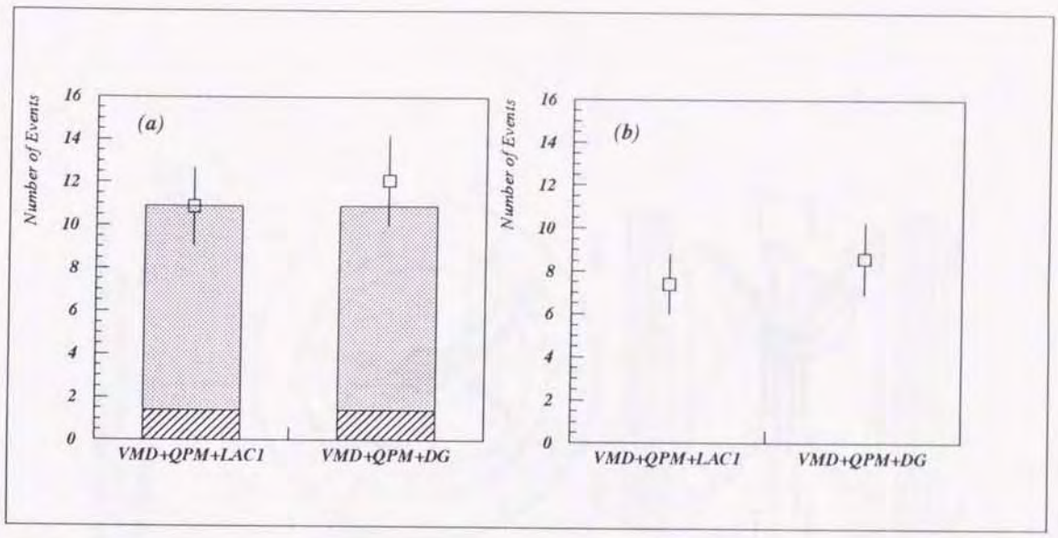

Figure 6.5: Fake muon estimation. (a) The maximum matching distance of the MUO hits with an extrapolated CDC track is set to 1 m in Monte Carlo simulation. The vertical bar shows the estimation of punchthrough (hatched area) and decay (shaded area) from analytical calculation and the open square shows the Monte Carlo prediction. (b) The maximum matching distance is set to two standard deviations. The open square shows the Monte Carlo prediction.

of the muon analysis is summarized in Fig. 6.12.

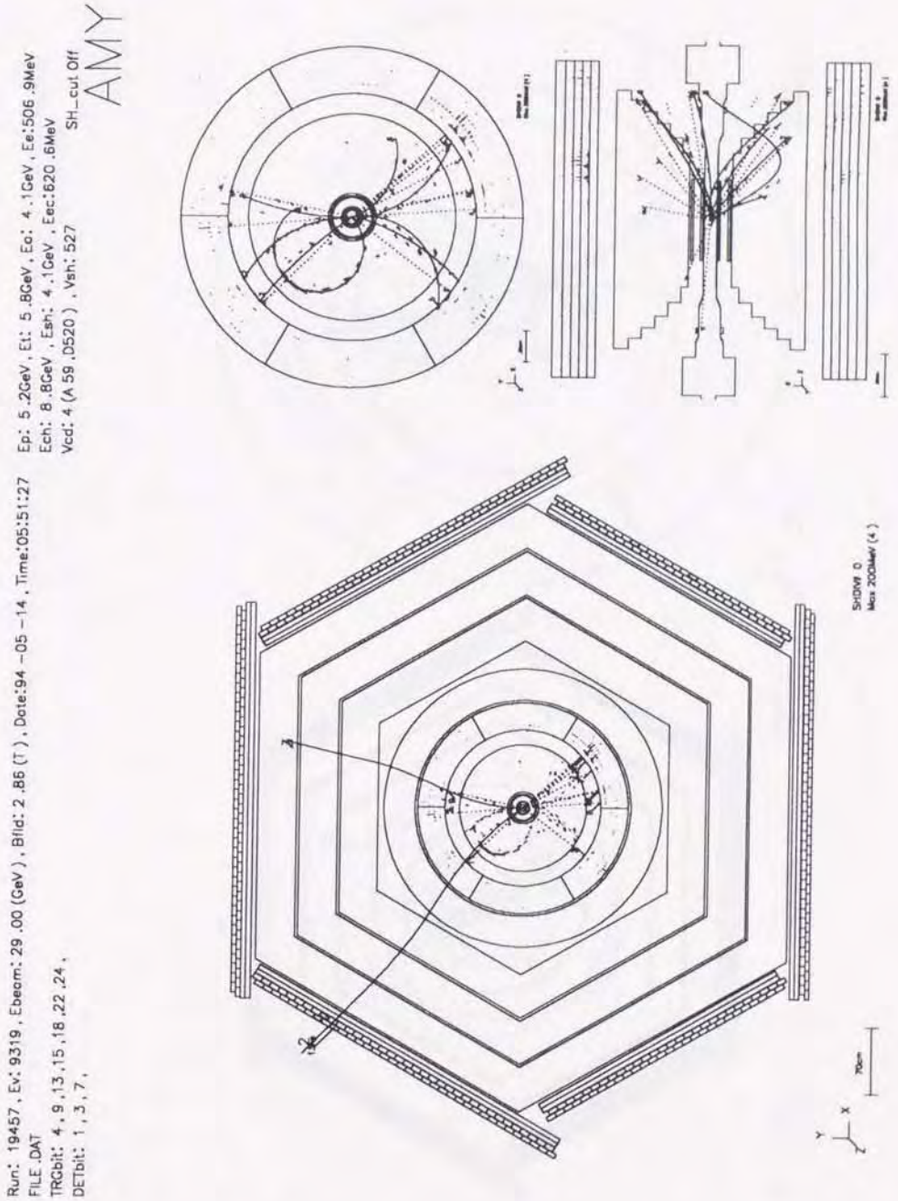

Figure 6.6: Example of inclusive muon event candidate.

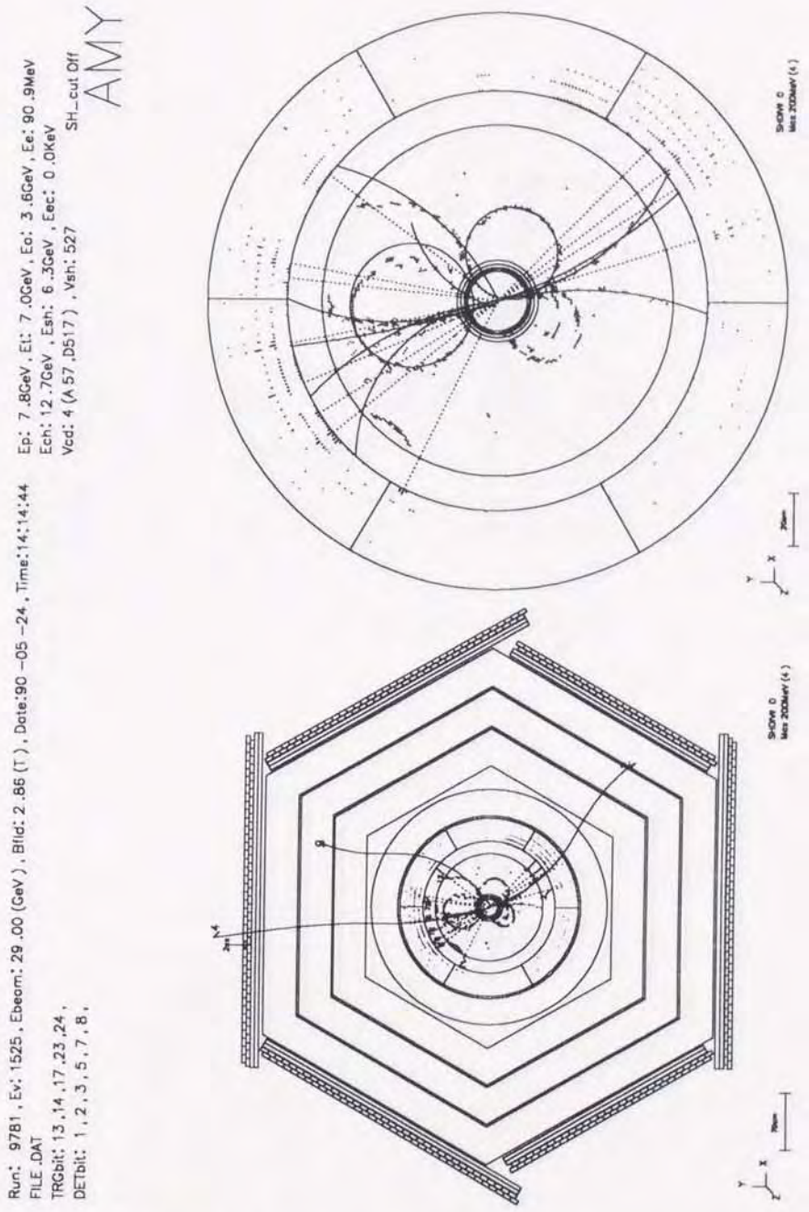

Figure 6.7: Example of inclusive muon event candidate.

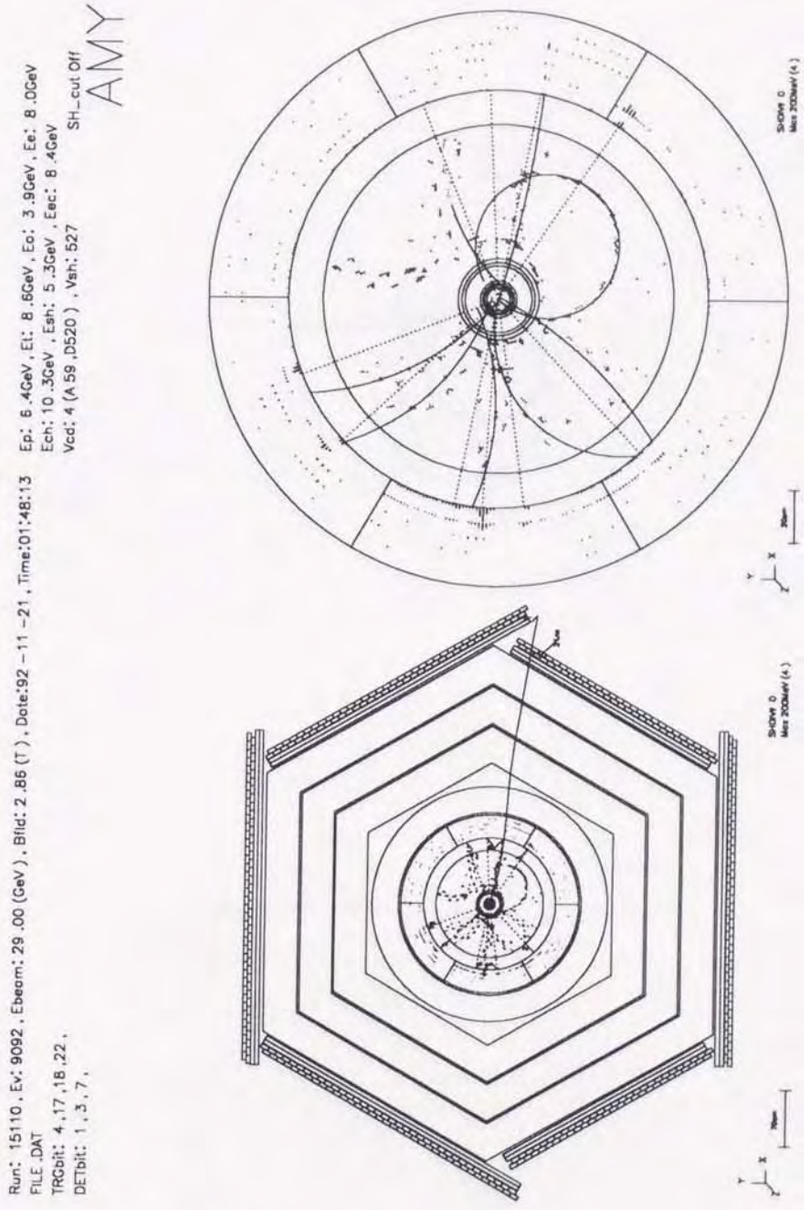

Figure 6.8: Example of inclusive muon event candidate.

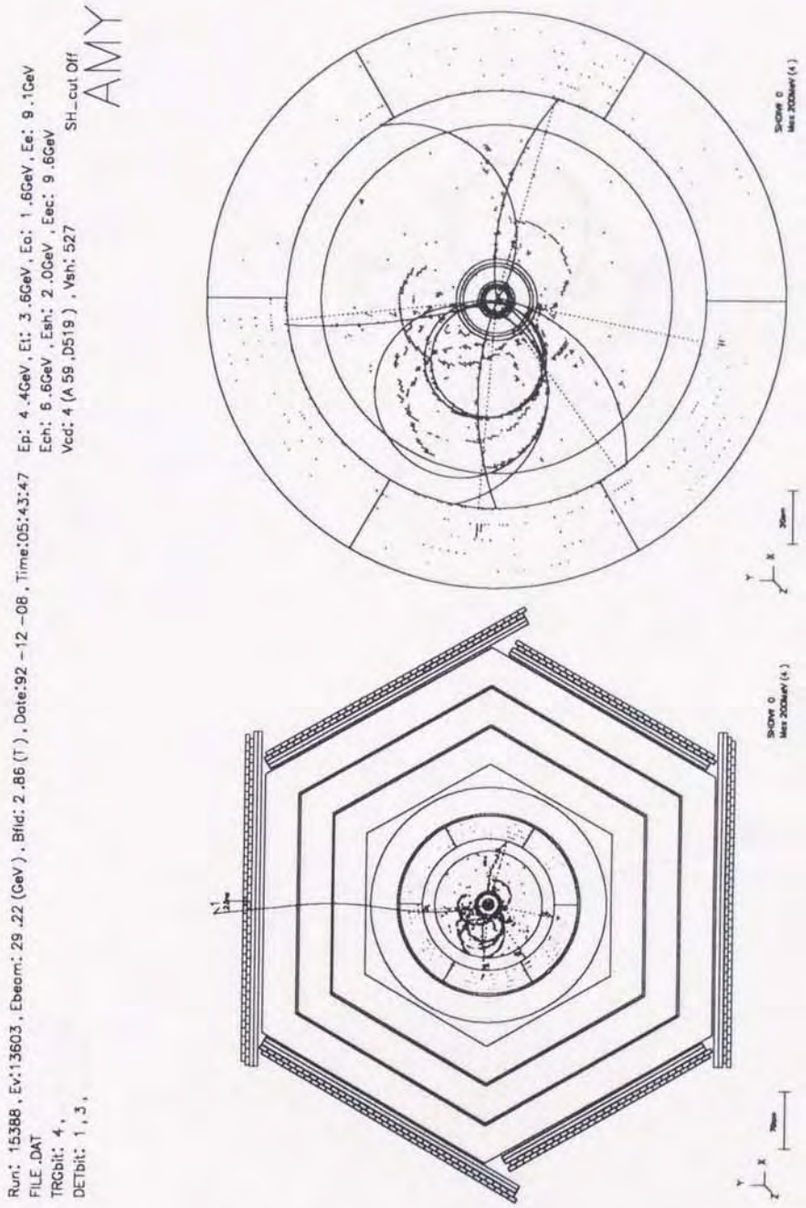

Figure 6.9: Example of inclusive muon event candidate.

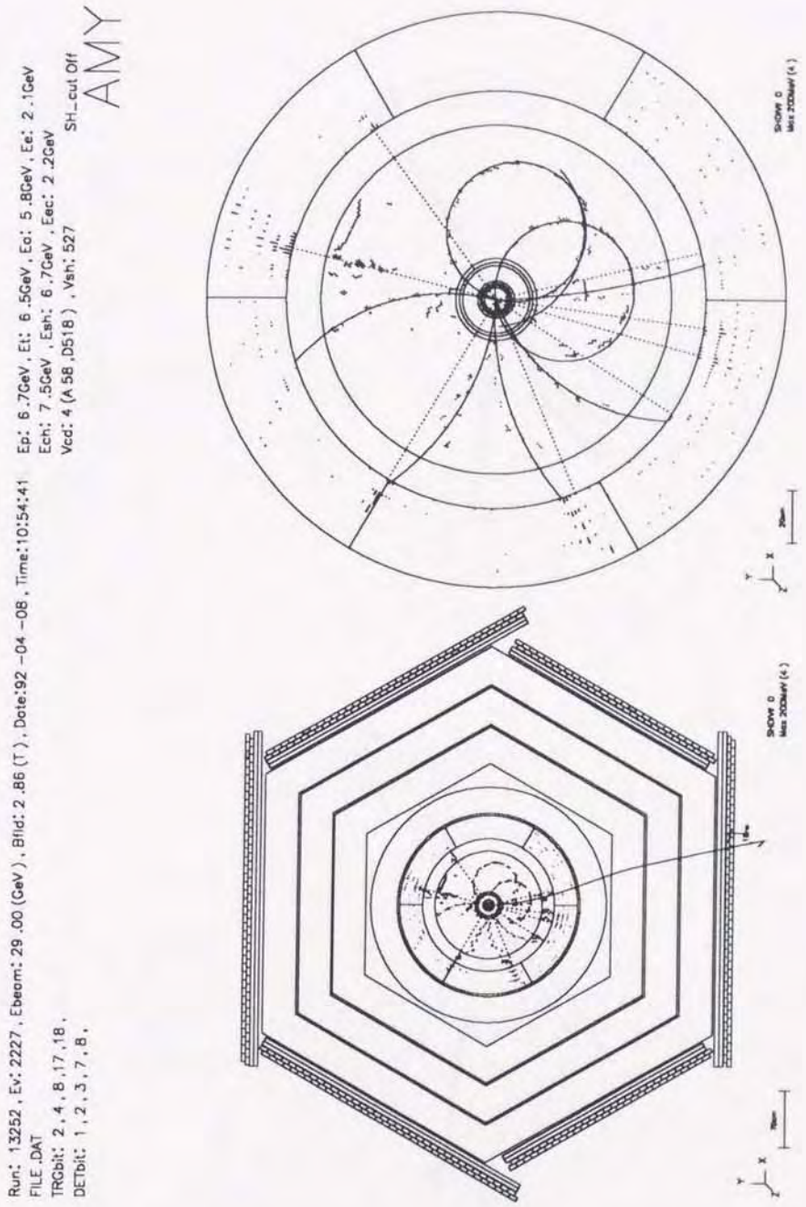

Figure 6.10: Example of inclusive muon event candidate.

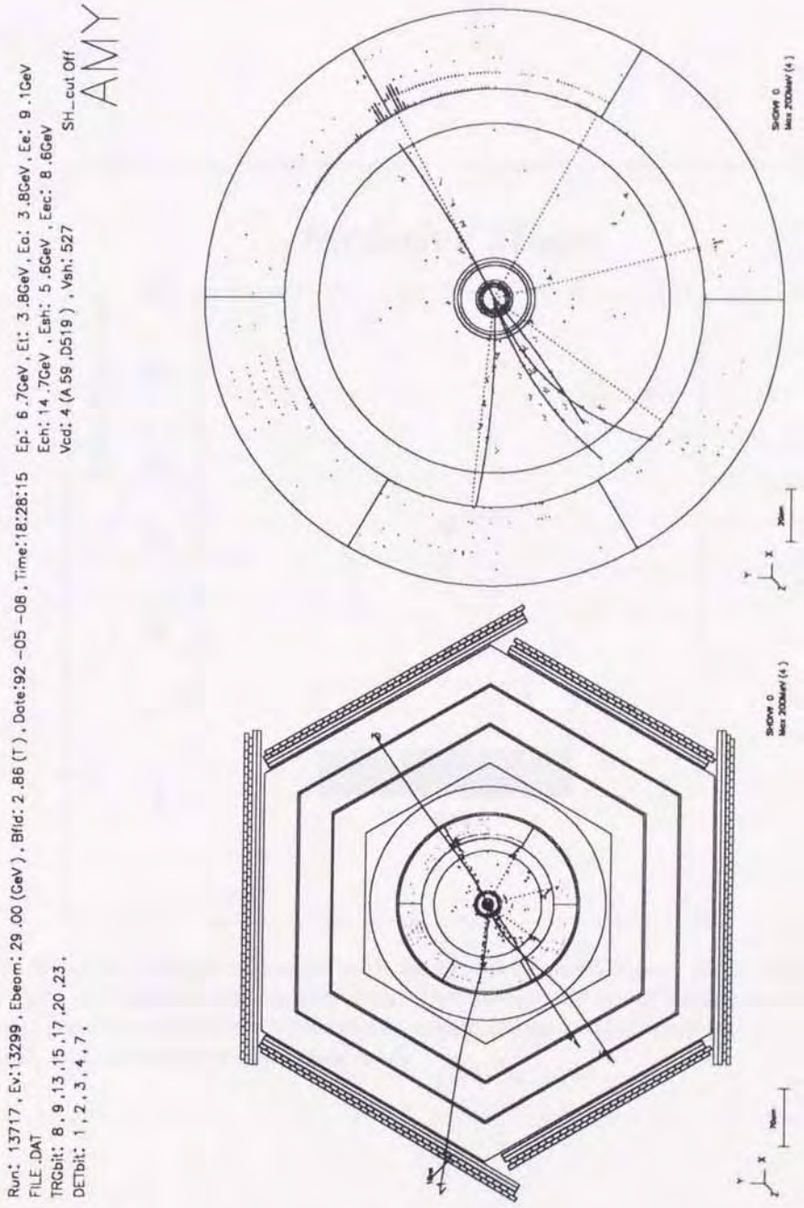

Figure 6.11: Example of inclusive muon event candidate.

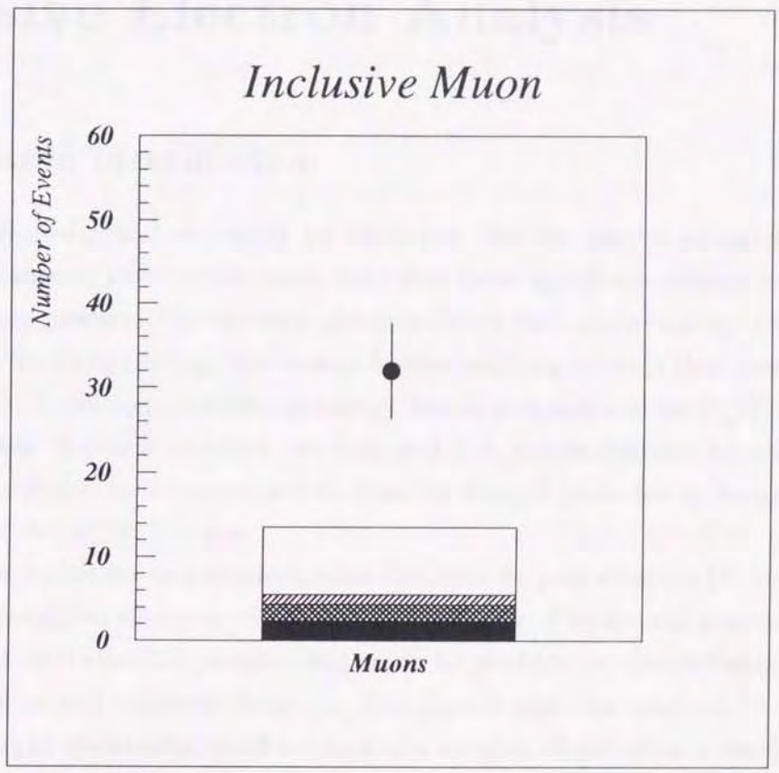

Figure 6.12: Observed number of muons with background contributions. Error bar is statistical only. The closed circle is from the experimental data. The background contributions are $e^+e^- \rightarrow e^+e^-\tau^+\tau^-$ (closed area), one γ annihilation multihadronic events (cross-hatched area), $e^+e^- \rightarrow e^+e^-b\bar{b}$ (singly-hatched area), and fake muon events (open area).

Chapter 7

Inclusive Electron Analysis

7.1 Electron Identification

Electrons and positrons lose energy by ionization like the heavier charged particles do. However, because of their small mass, they also have significant energy loss due to the bremsstrahlung process. For electron energies above the critical energy (E_c =7.2 MeV in lead), the fractional energy loss due to bremsstrahlung exceeds that due to ionization (Fig. 7.1 [40]). Since bremsstrahlung energy loss is proportional to $\left(\frac{zeZ}{m}\right)$, where m and ze are mass and charge of incident particle, and Z is atomic number of material, energy loss via bremsstrahlung is suppressed for heaveir charged particles by factor of $\propto \left(\frac{m_e}{m}\right)^2$, which is the order of 10^{-4} or less.

The radiated photons will create further electrons by pair creation ($E > 2m_e$) and will also transfer energy to electrons via Compton scattering. The second generation electrons will in turn generate further photons and so on to produce an electromagnetic shower of photons, positive and negative electrons. The shower particles continue to multiply and lose their energies eventually, until a maximum number of particles is reached when the average particle energy is no longer high enough to continue the multiplication process. Beyond this point, the electron energies dissipate their energy by ionization and excitation process. This is because with increasing depth, a larger fraction of the cascade energy is carried by photons. These process initiates an "electromagnetic cascade shower".

The longitudinal development is governed by the high-energy part of cascade, and therefore scales as the radiation length (X_0) in material. Therefore, if the material of the shower counter is thick enough, the full incident electron energy will be deposited. But the other all charged particles lose their energies by ionization process. The energy deposition of the other particles are the level of minimum ionization at energies above 1 GeV.

For hadrons about half of the incident hadron energy is dissipated by the ionization losses of scattered secondaries. It is consumed in multiparticle production of slow pions and in other processes. A typical secondary hadrons is produced with a transverse momentum of ~350 MeV/c, so that hadronic showers tend to be more spread out laterally than electromagnetic ones which deposit most of its energy in a narrow cone around the track projection with cylider radius of $R_M = (E_s/E_c)X_0$, where E_s is scale energy defined as $\sqrt{4\pi/\alpha}m_e c^2$, so that about 90% of the shower energy is contained within $\sim 3X_0$ ($\simeq 1.6$ cm) for Pb.

Our electron identification algorithm use these characteristics of shower, its shape and energy deposition.

A first step of electron identification using SHC is to calculate a energy of shower clusters, using only three strips around the center of shower cluster position. The total widthes of three strips are about 3.5 cm and 4.3 cm for θ and ϕ-strips, respectively. The caluclated energy is then compared with the momentum of charged tracks, of which extrapolated direction have to be inside of $2^\circ \times 2^\circ$ window in θ and ϕ from center of the shower cluster. When taking the energy to momentum ratio E/p between them, the electrons tend to be $E/p \simeq 1$, and hadrons would have $E/p \ll 1$. Because the electrons lose all their energies inside SHC, but hadrons do not, as mentioned above. The shower cluster energies calculated with narrow width are expected to contain all deposited energies from electrons, but not to contain from interacting hadrons. The requirement for the value of E/p are imposed to select the tracks with $E/p \simeq 1$.

The another approach to separate electrons from hadrons is to use the profile of longitudinal energy deposition of the cascade showr. Since SHC has longitudinal segmentation, we can evaluate the longitudinal shower development of an incident particle whether it is consistent with electron or not. The fraction of energy deposition in a segment to the total energy deposition was checked for each segment. Looking at the longitudinal development of shower, especially for first segment, we can distinguish electrons from hadrons.

The cuts used in this analysis consists of E/p and longitudinal shower profile cuts. The cut values are shown in Table 7.1.

The validity of our cuts for electron identification in the experimental conditions was confirmed using $e^+e^- \rightarrow e^+e^-e^+e^-$ events sample. The events are selected by requiring 1)two charged tracks, 2)momentum of both tracks are in the range from 2 GeV/c to 5 GeV/c, and 3)one of two tracks have to be identified as an electron, then the evaluation of our shower selection criteria have been tested for another track. The E/p distributions and fraction of energy in a segment to total shower are shown in Fig. 7.2~ 7.4, for different

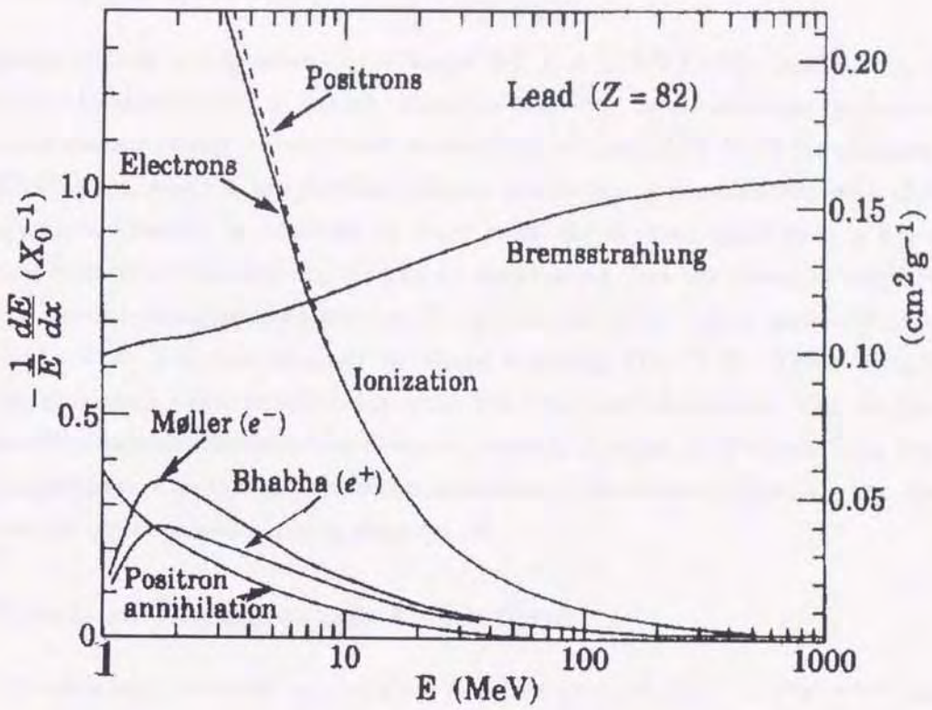

Figure 7.1: Fractional energy loss for electrons and positrons.

	2.0≤p<2.5		2.5≤p<4.0		4.0≤p<5.0	
	min	max	min	max	min	max
E/p	0.77	–	0.78	–	0.78	–
E_1/E_{tot}	0.01	0.60	0.02	0.35	0.01	0.22
E_2/E_{tot}	0.03	0.68	0.03	0.55	0.05	0.50
E_3/E_{tot}	0.01	0.51	0.05	0.51	0.03	0.50
E_4/E_{tot}	0.01	0.40	0.03	0.40	0.04	0.40
E_5/E_{tot}	0.00	0.30	0.00	0.30	0.00	0.30

Table 7.1: The cut values for electron identification, where E_i/E_{tot} represents the fraction of energy deposition in a segment to the total shower cluster energy.

different momentum ranges. The cut values are also shown visually in these figures.

7.2 Electron Selection

A charged track in the momentum range $2.0 \leq p \leq 5.0$ GeV/c and within $\pm 2°$ (in ϕ and θ) of the direction of a shower cluster is classified as an electron candidate if the ratio of the shower energy to the track momentum exceeds 0.78 (0.77 for charged tracks below 2.5 GeV/c), and the longitudinal shower development is consistent with that of an electromagnetic shower. In addition to these cuts, the electron candidate is required to be isolated from the nearest charged track by demanding that the isolation angle between it and the nearest charged track exceeds 6°. Events from the higher-order-QED process, $e^+e^- \rightarrow e^+e^-e^+e^- + \gamma$, are rejected by visual scanning (Fig. 7.7). These criteria were chosen to give good electron efficiency with low pion contamination. The Monte Carlo estimate of the electon identification efficiency is 60%. A total of 49 events from the untag event sample survive as inclusive electron candidates. No events containing two electrons or more or an electron and a muon were found.

7.3 Electron Backgrounds Estimation

Backgrounds from hadronic annihilation (2.8±1.6 events), $e^+e^- \rightarrow e^+e^-\tau^+\tau^-$ (4.0±1.8 events), and $e^+e^- \rightarrow e^+e^-b\bar{b}$ (1.4±0.2 events) are estimated with the Monte Carlo techniques used for the inclusive muon sample.

The backgrounds in bonafide two-photon events originating from γ-conversion and π^0 Dalitz decay ($\pi^0 \rightarrow e^+e^-\gamma$) were estimated by using a Monte Carlo event sample for $e^+e^- \rightarrow e^+e^-$+ hadrons. Again, we normalize to the same number of tracks for the Monte Carlo event sample and the untag event sample. The combined estimated contribution was 2.8±0.7 events.

The backgrounds due to fake electrons were evaluated for the following two possibilities:

1) γ-hadron overlap

If an electromagnetic shower produced by a γ or π^0 is close to a charged track, the charged track could be mistaken as an electron.

An estimate of the background due to overlaps was done using the full untag event sample. A shower cluster in an event was moved artificially to within a 2 degree cone around a charged track and combined with the cluster produced by the track itself (Fig. 7.5). Then the criteria for an electron candidate were applied to the combined cluster (Fig. 7.6). After accounting for the probability that a cluster falls within a

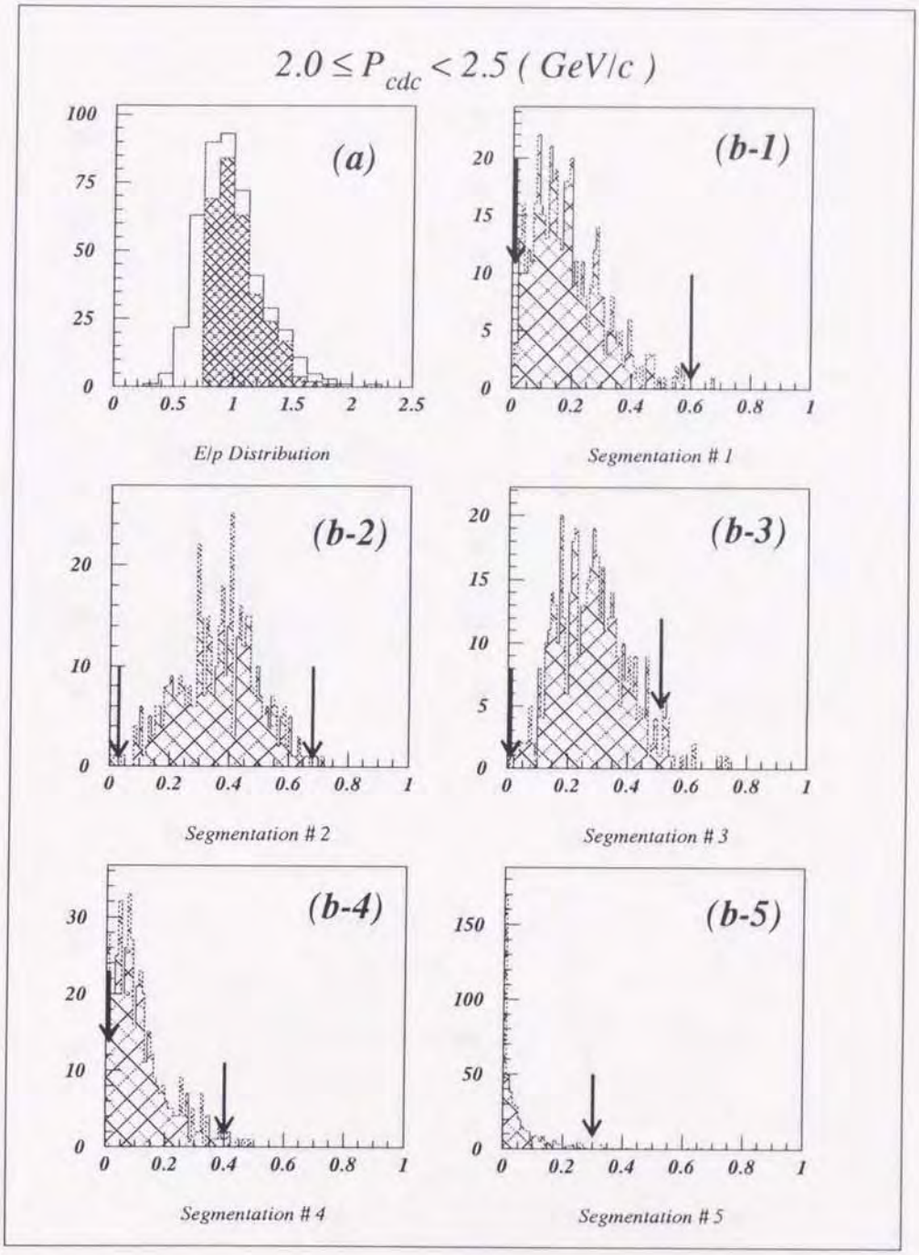

Figure 7.2: The evaluation of electron selection criteria for momentum range $2.0 \leq p < 2.5$ GeV/c . The distribution of (a) E/p where open and shaded histgrams show before and after the longitudinal shower profile cuts, respectively, and (b) fractional energy deposition of each segemet to the total shower energy for electron from $e^+e^- \rightarrow e^+e^-e^+e^-$ process. Downward arrows show cut values.

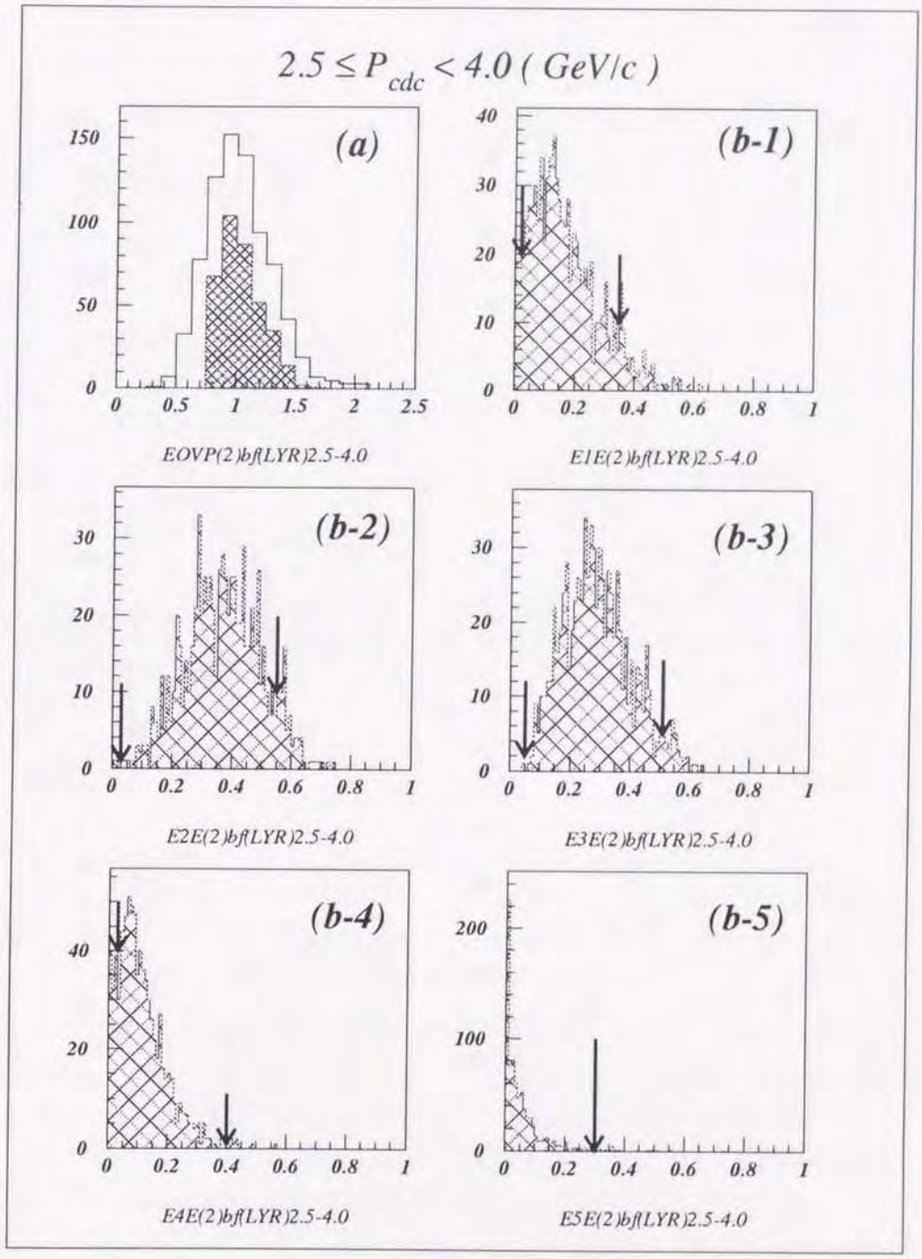

Figure 7.3: The evaluation of electron selection criteria for momentum range $2.5 \leq p < 4.0$ GeV/c . The distribution of (a) E/p where open and shaded histgrams show before and after the longitudinal shower profile cuts, respectively, and (b) fractional energy deposition of each segemet to the total shower energy for electron from $e^+e^- \rightarrow e^+e^-e^+e^-$ process. Downward arrows show cut values.

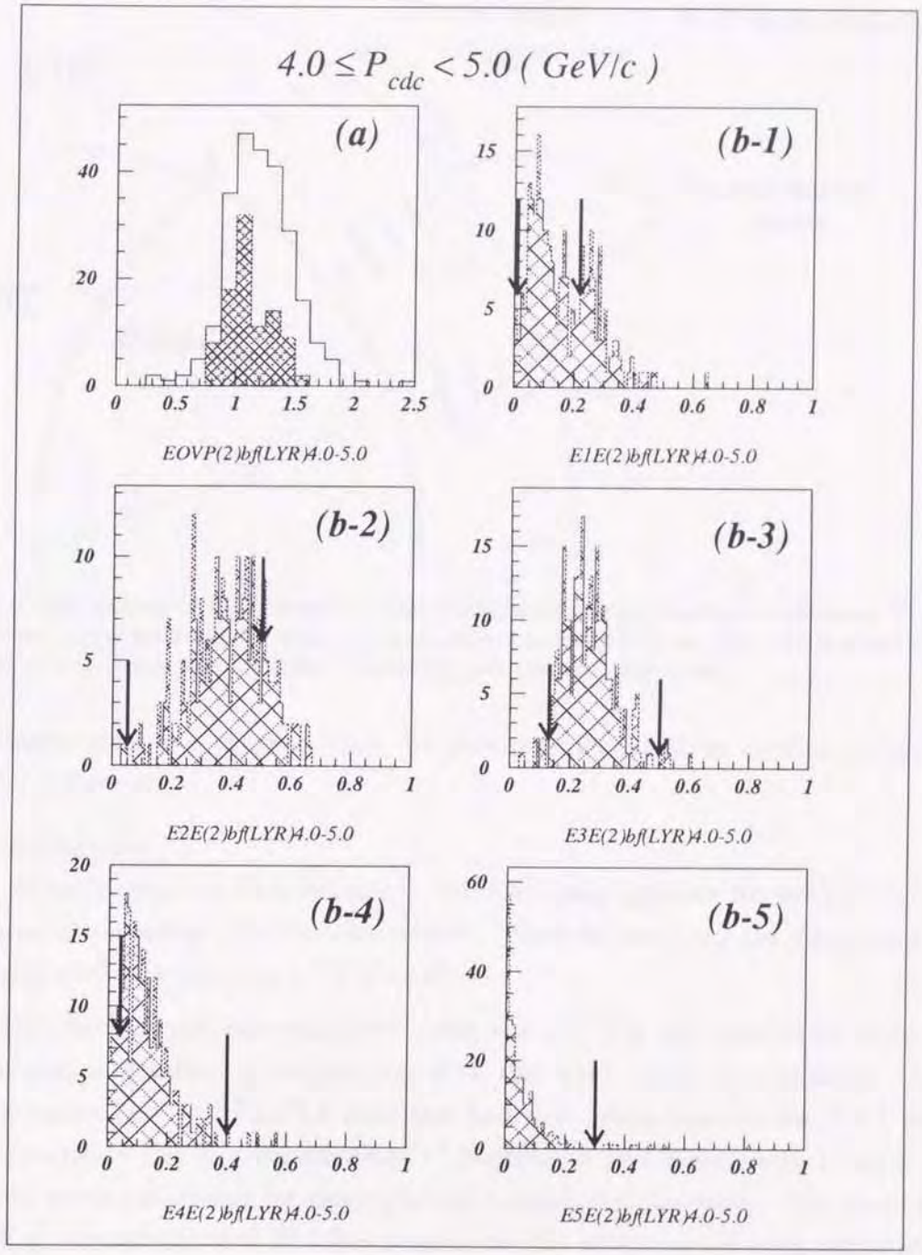

Figure 7.4: The evaluation of electron selection criteria for momentum range $4.0 \leq p < 5.0$ GeV/c . The distribution of (a) E/p where open and shaded histgrams show before and after the longitudinal shower profile cuts, respectively, and (b) fractional energy deposition of each segemet to the total shower energy for electron from $e^+e^- \rightarrow e^+e^-e^+e^-$ process. Downward arrows show cut values.

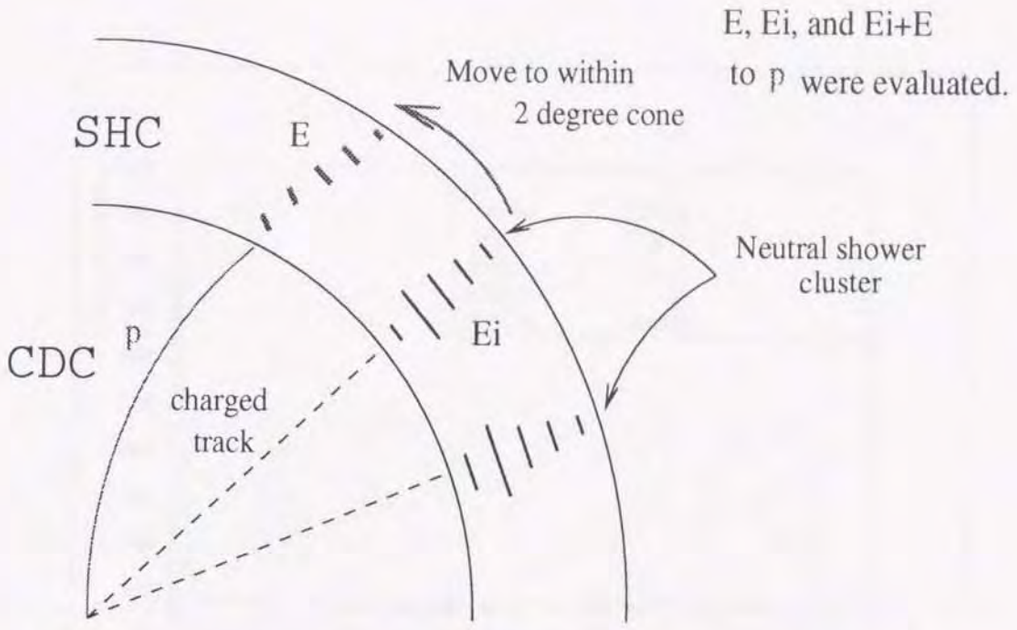

Figure 7.5: The method of the estimation of the background due to γ-hadron overlapping. The neutral clusters were moved artificially to within 2 degree cone of a charged tracks. The combinations of charged track and shower cluster were evaluated whether it pass electron cuts or not.

2 degree cone of a charged track, we obtained the γ-hadron overlap background of 0.5 ± 0.2 events.

2) Interacting pion

Pions interacting hadronically in the SHC may produce an energy cluster that passes the electron identification criteria. Such interactions are dominated by the charge exchange reaction $\pi^- + \mathrm{p} \rightarrow \pi^0 + \mathrm{n}$.

This background was estimated using the FLUKA [46] simulation code for the hadronic interaction in conjunction with the AMY detector simulation. In order to examine how well FLUKA simulates hadronic interactions in the AMY detector, we compared the E/p distributions of hadrons in real events with those in Monte Carlo simulated events for single-photon annihilation processes. The results shown in Fig. 7.8 indicate that FLUKA reproduces the experimental data rather well.

We generated pions with the same momentum and angular distributions as those of the hadrons in the untag event sample (Fig. 7.9) and simulated their interactions in the SHC with FLUKA. From these we determine a probability of 4.2% for a pion to be identified as an electron. Assuming all charged particles in the untag

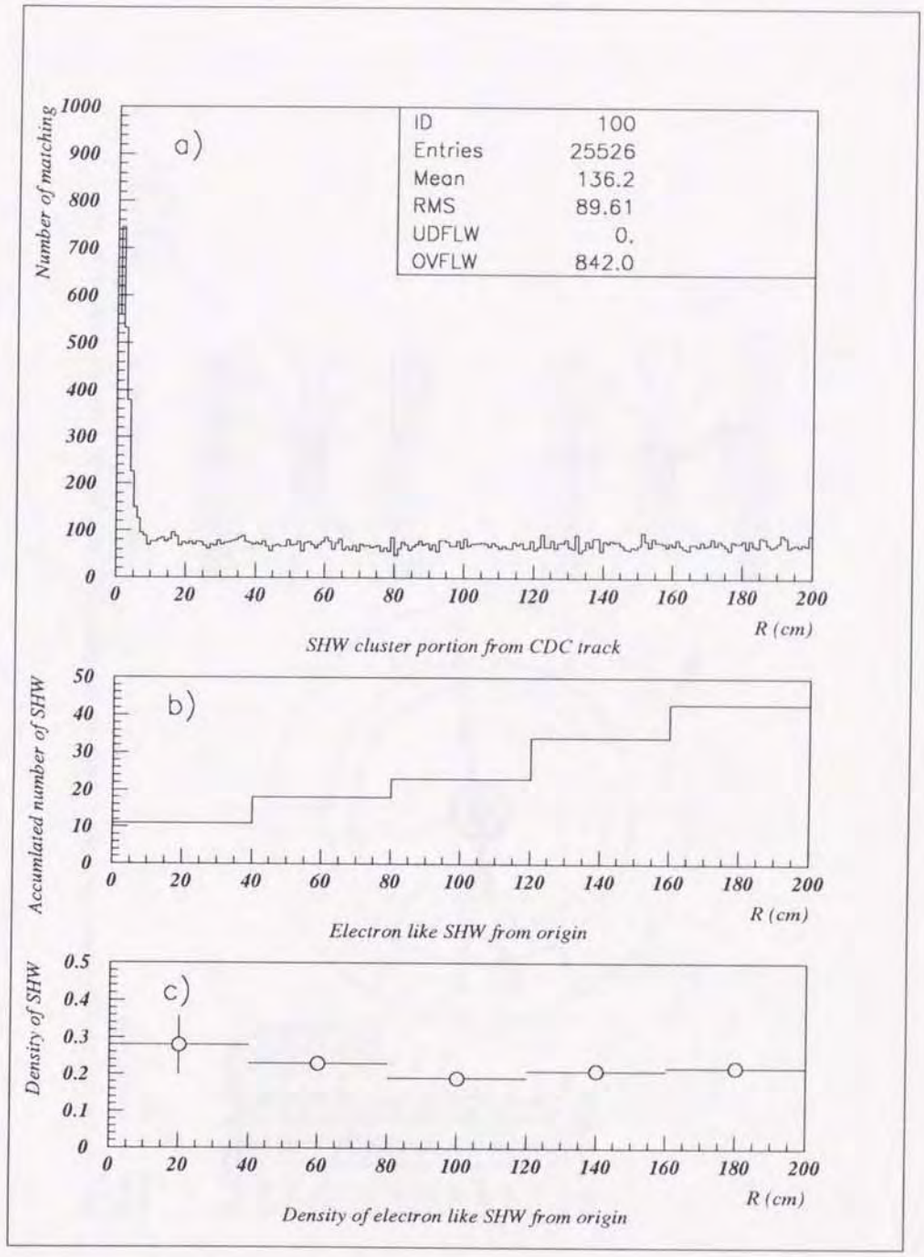

Figure 7.6: The SHW cluster position around one track. a)The SHW cluster positions for all the clusters. b)One of the clusters is combined with nearest SHW clusters and evaluated whether it pass electron criteria or not. The plot shows accumlated number of electron like SHW clusters as a function of R. c)The density of misidentified electron due to overlapping inside R.

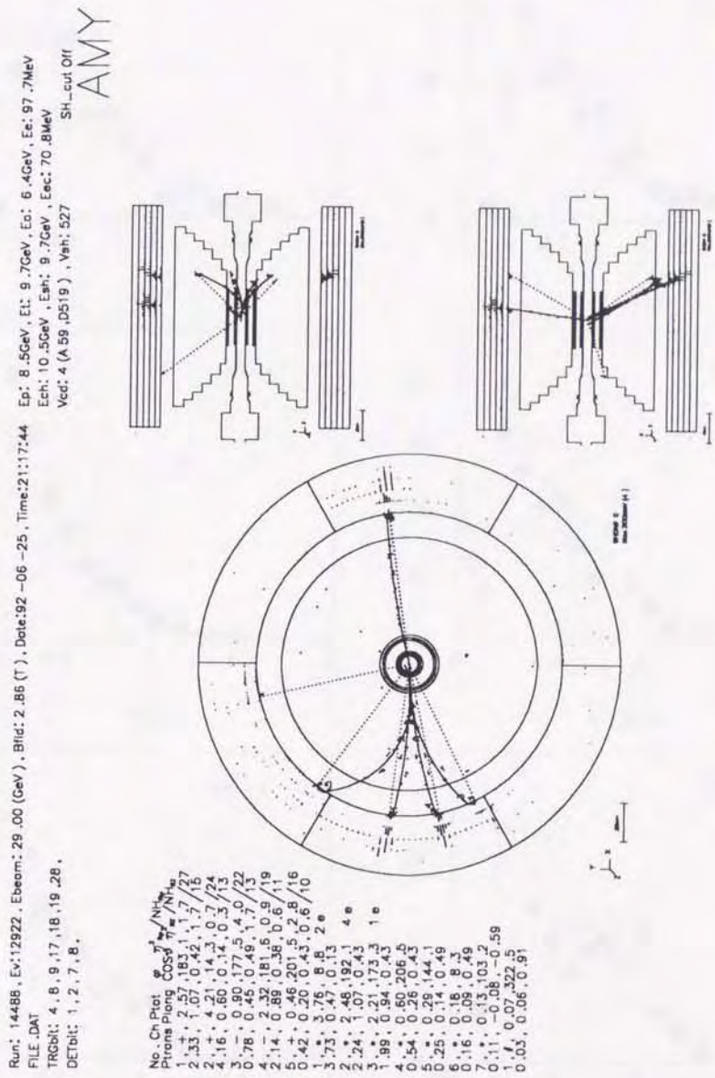

Figure 7.7: One of the rejected events by the visual scan.

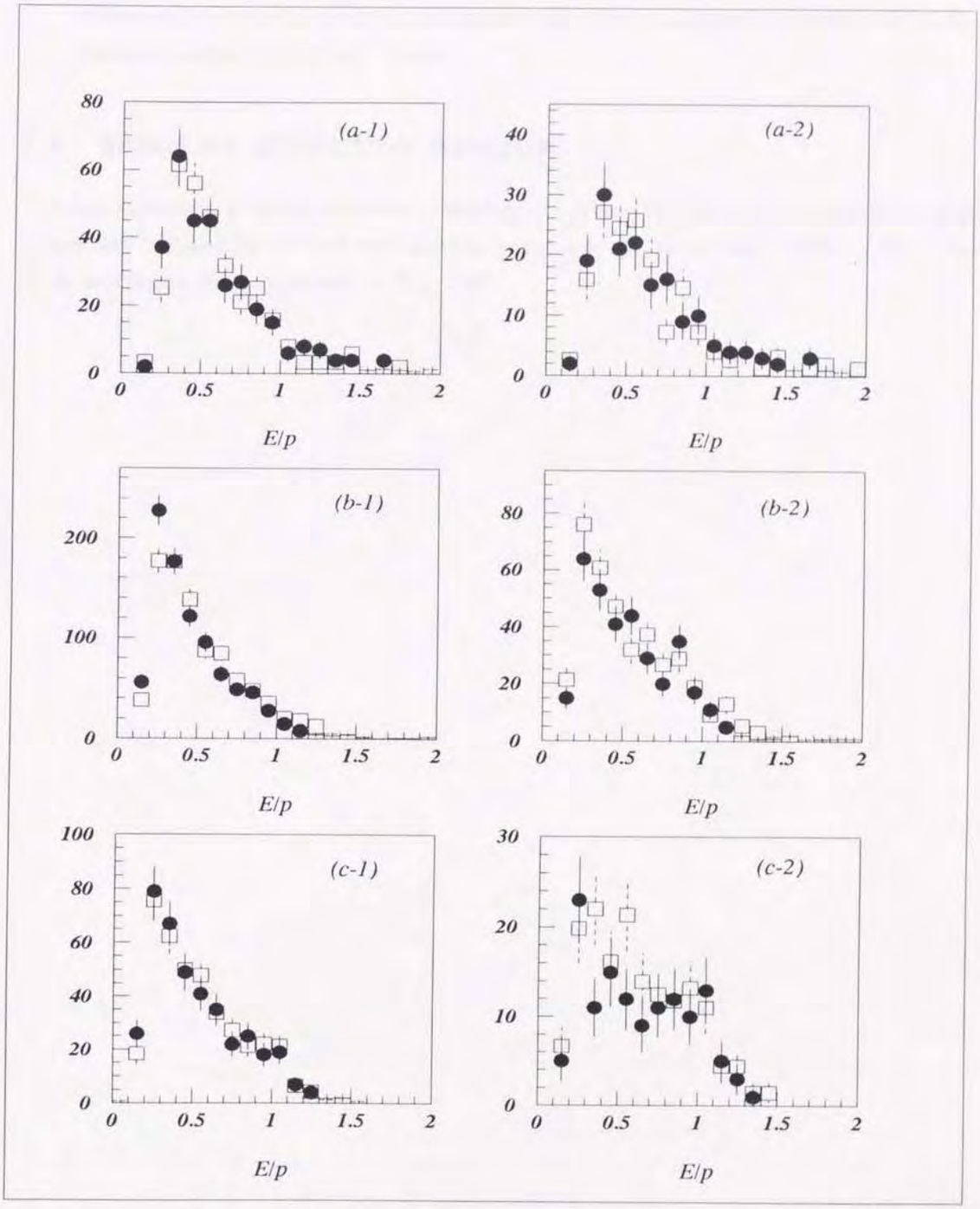

Figure 7.8: Comparison of FLUKA Monte Carlo with experimental data for E/p distributions of different momentum region in annihilation process. The closed circle shows the experimental data and the open square shows the FLUKA prediction. The left and right sides show before and after the shower profile cuts, respectively. The momentum regions are (a) $2.0 \leq p < 2.5$ GeV/c, (b) $2.5 \leq p < 4.0$ GeV/c, and (c) $4.0 \leq p \leq 5.0$ GeV/c.

event sample are pions gives an estimate of the interacting pion contamination of the electron sample of 15.4 ± 0.7 events.

7.4 Summary of Electron Analysis

After subtracting the background contributions, there are 22.1 ± 7.5 inclusive electron events left. Examples of inclusive electon event are shown in Figs. 7.10$\sim$ 7.15. The electron analysis is summarized in Fig. 7.16.

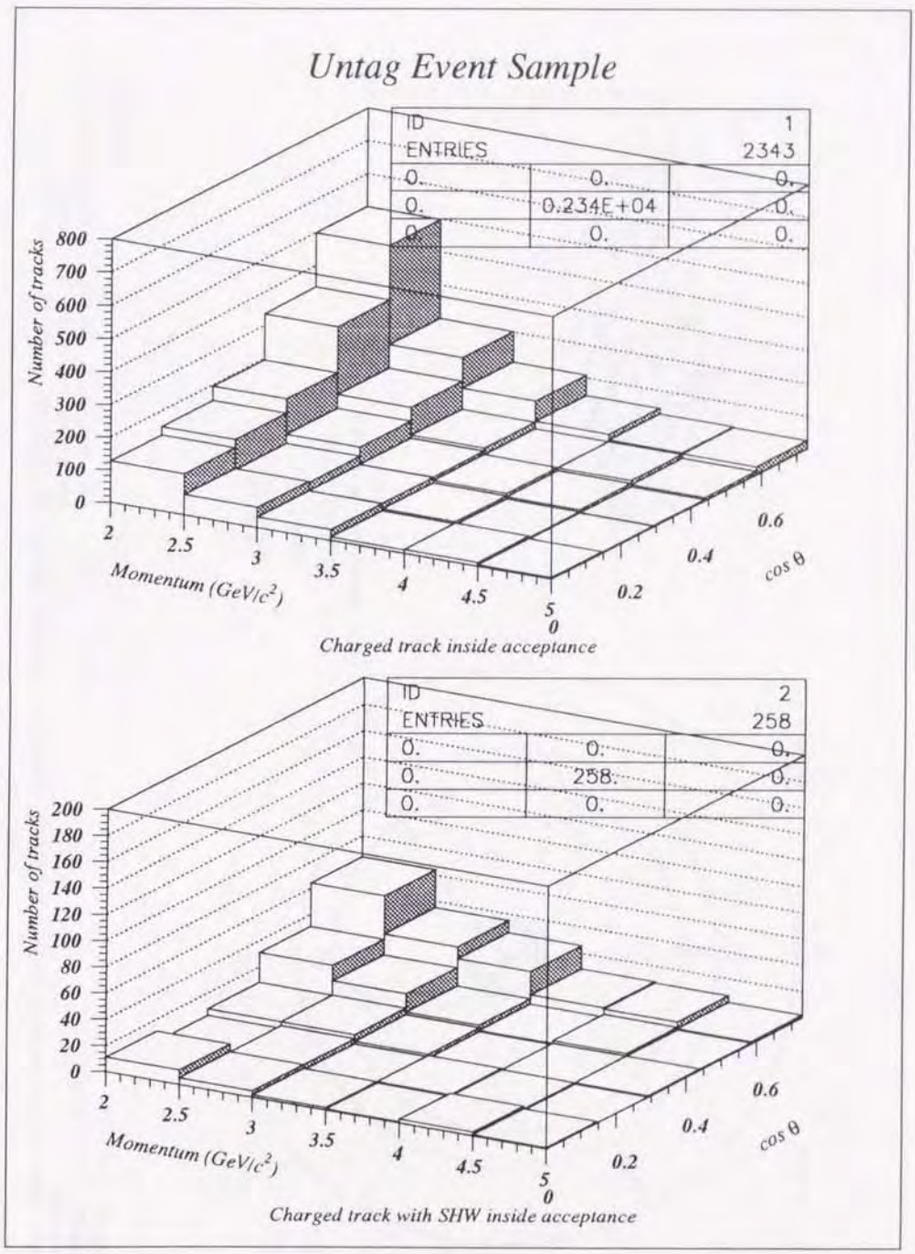

Figure 7.9: Momentum distribution of charged tracks. a)All tracks inside acceptance for electron selection. b)The tracks with associating SHW cluster of energy more than 1.0 GeV.

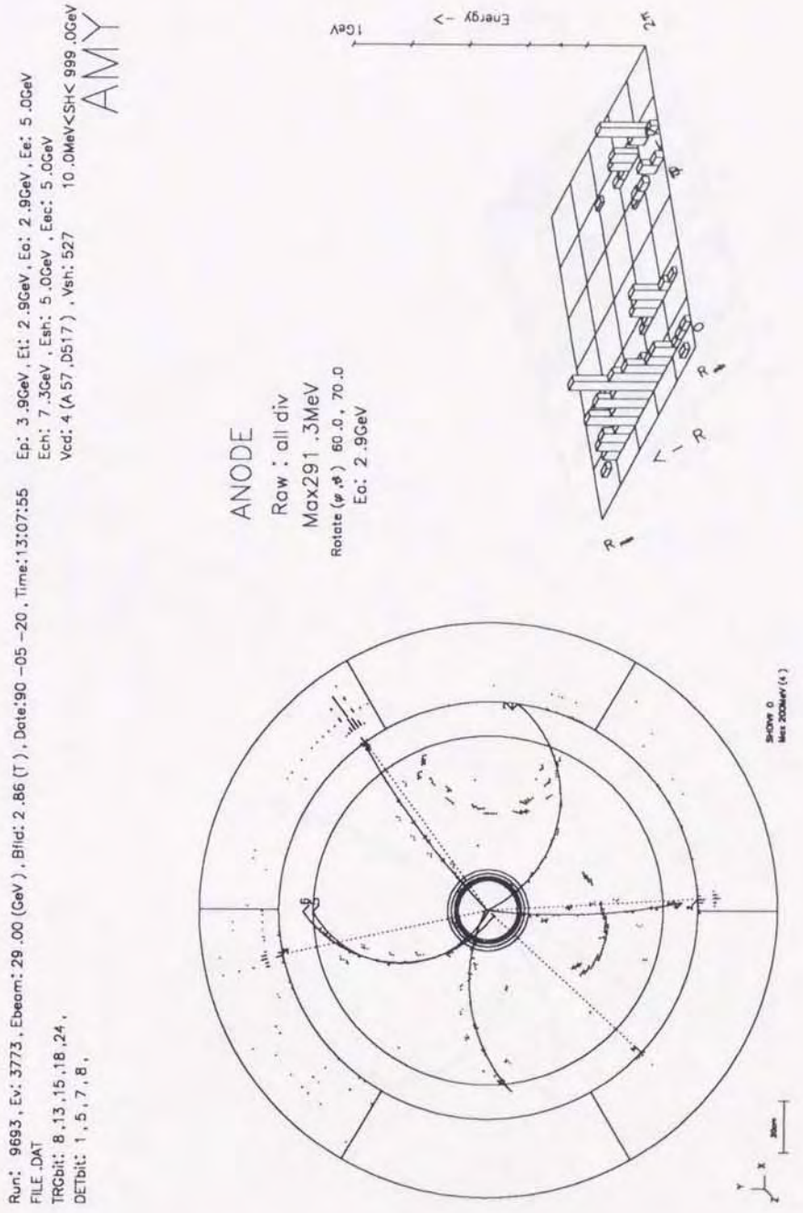

Figure 7.10: Example of inclusive electron event candidate.

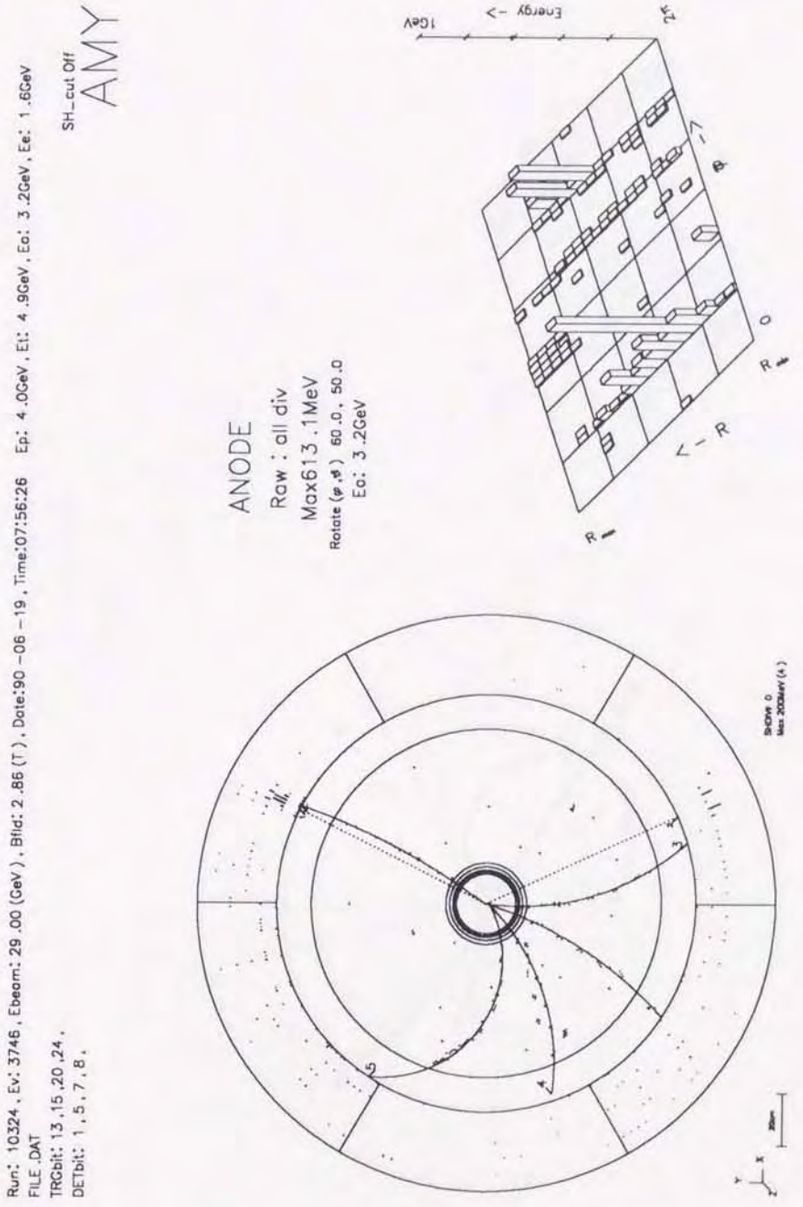

Figure 7.11: Example of inclusive electron event candidate.

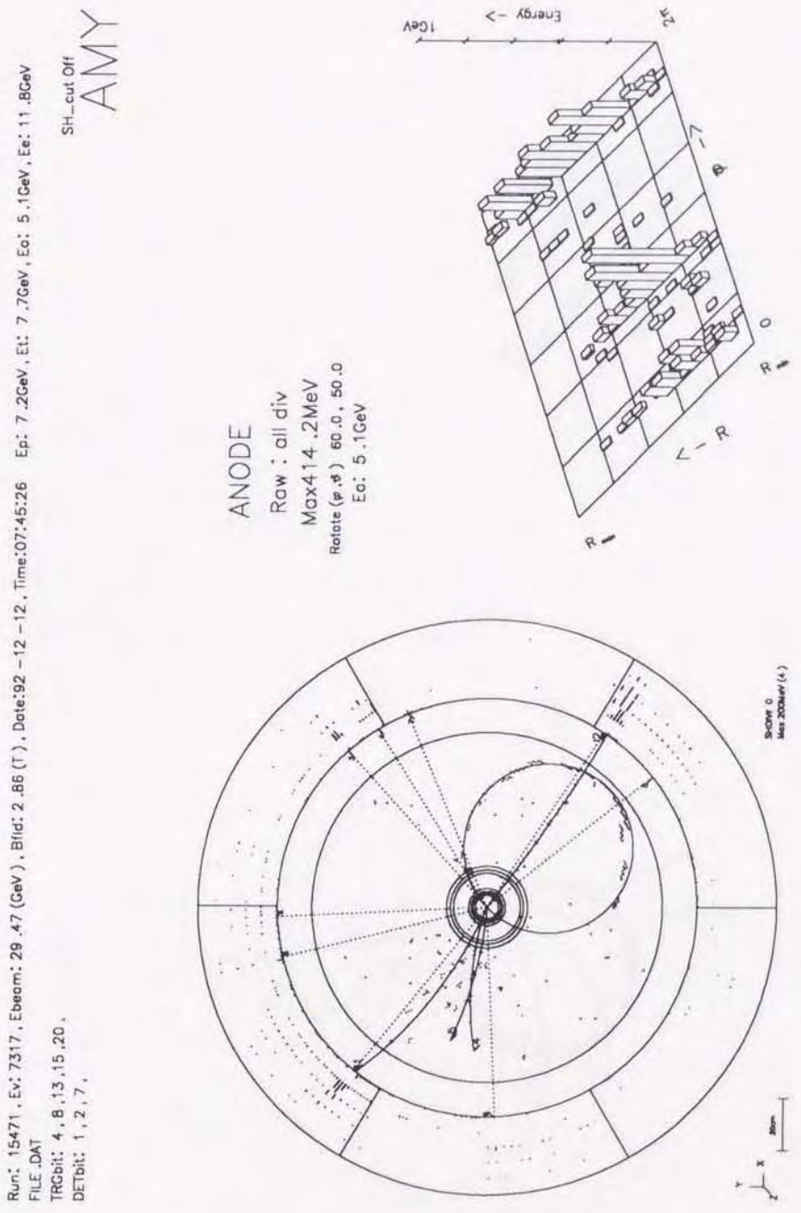

Figure 7.12: Example of inclusive electron event candidate.

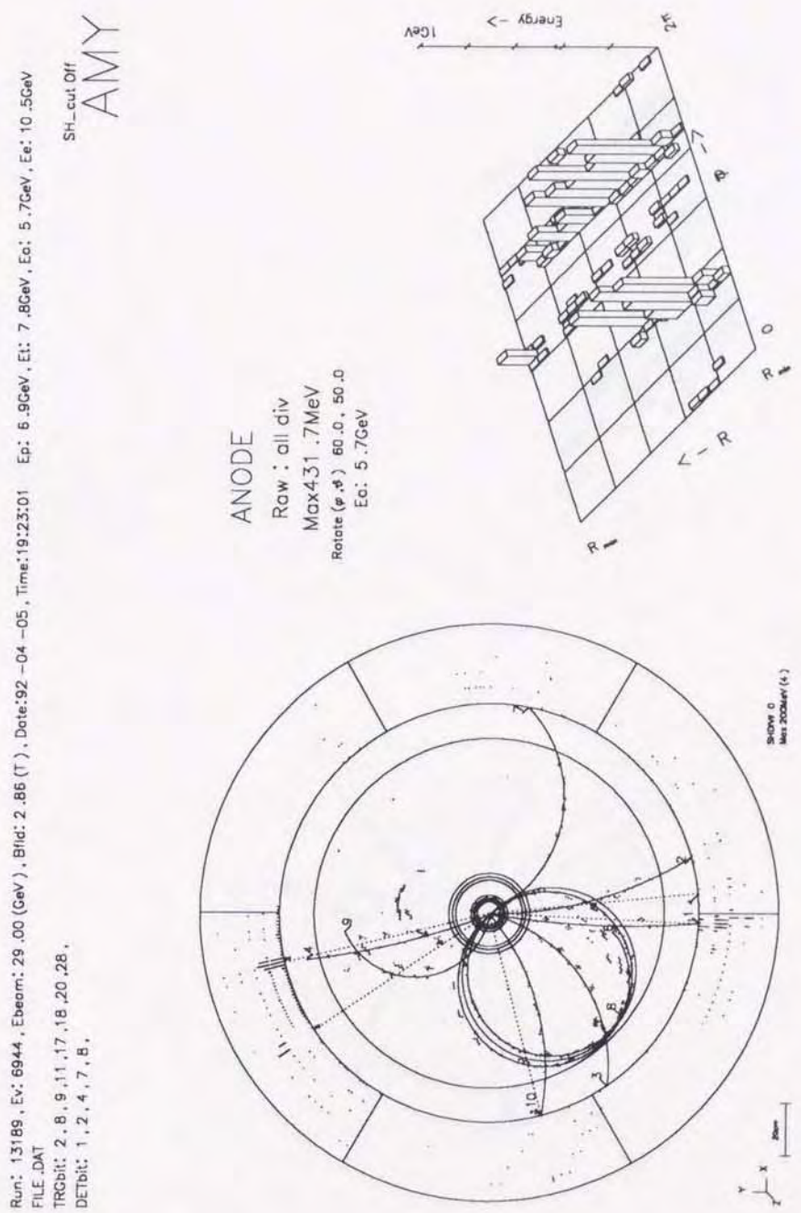

Figure 7.13: Example of inclusive electron event candidate.

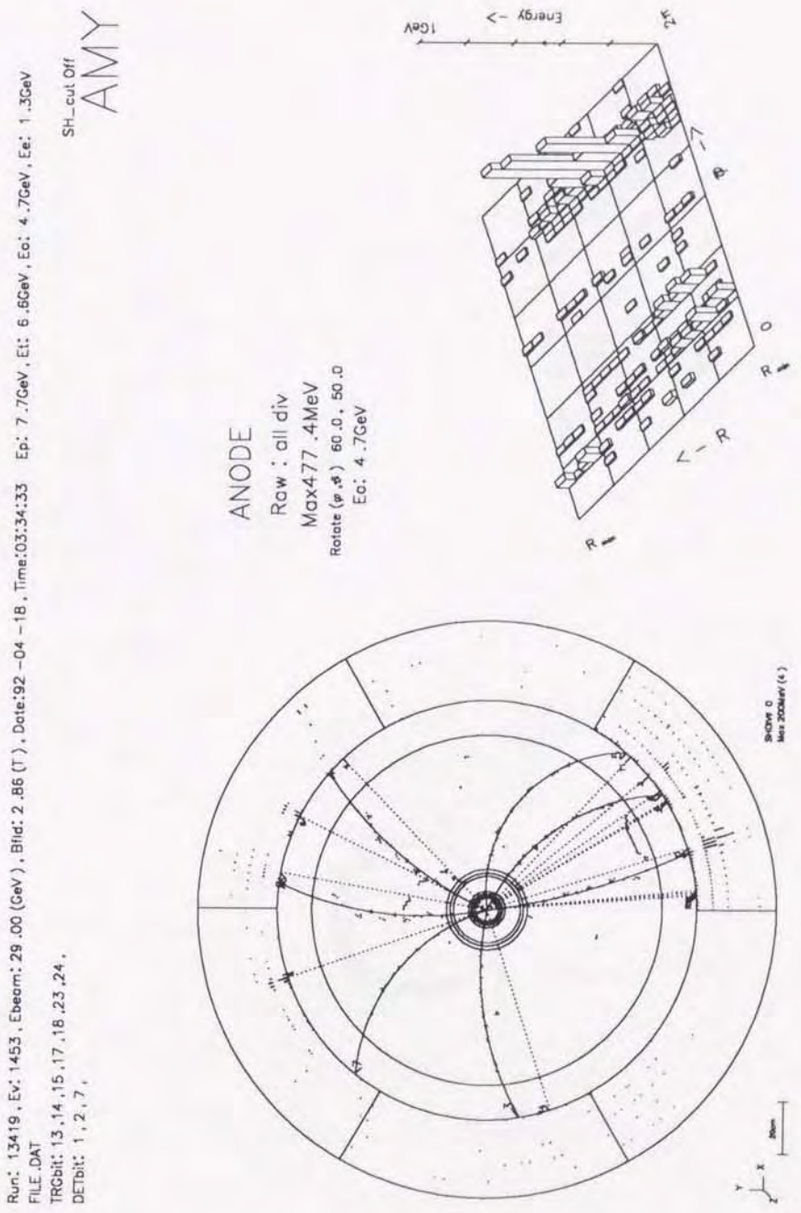

Figure 7.14: Example of inclusive electron event candidate.

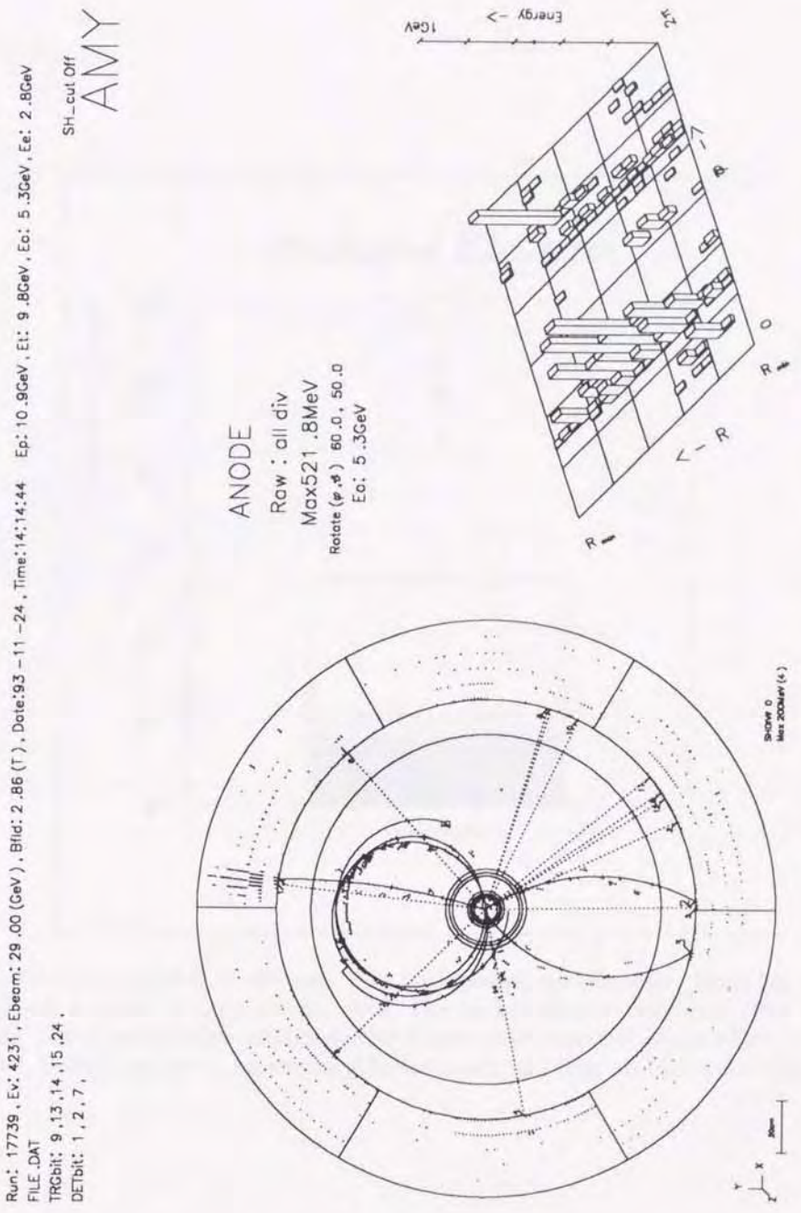

Figure 7.15: Example of inclusive electron event candidate.

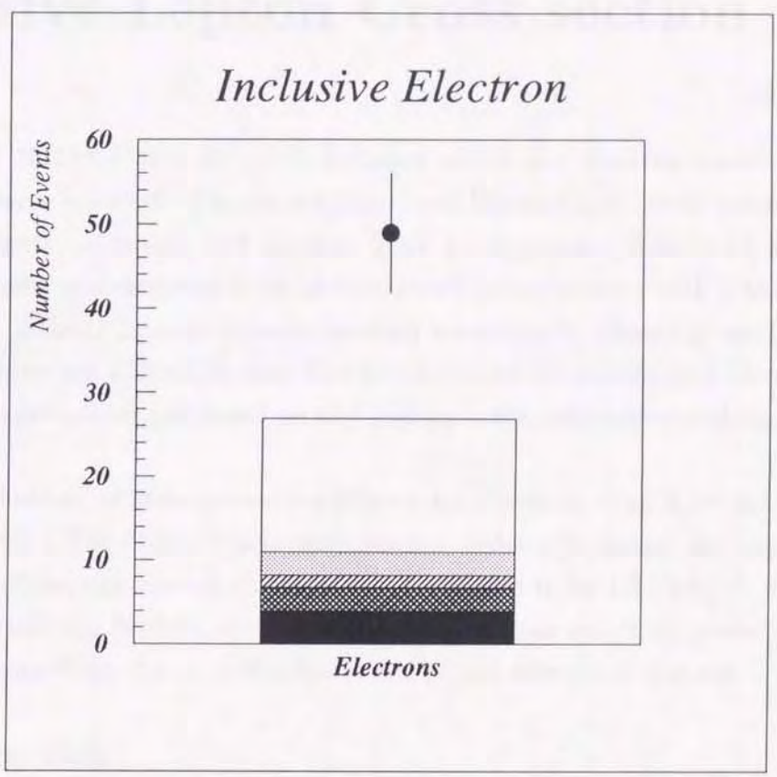

Figure 7.16: Observed number of electrons with background contributions. Error bar is statistical only. The closed circle is from the experimental data. The background contributions are $e^+e^- \rightarrow e^+e^-\tau^+\tau^-$ (closed area), one γ annihilation multihadronic events (cross-hatched area), $e^+e^- \rightarrow e^+e^-b\bar{b}$ (singly-hatched area), Dalitz pair and γ conversion (shaded area), and fake electron events (open area).

Chapter 8

Inclusive Lepton Cross section

The total of 18.5±6.1 and 22.1±7.5 inclusive muon and electron events, respectively, from charm were selected. The expectation from Monte Carlo study are 6.18±0.26 and 7.90±0.29 events for muons and electons from direct process, 0.59±0.14 and 1.27±0.20 events for muons and electrons from photon-gluon fusion process with LAC1 parton density function. If the DG parton density function was taken for photon gluon-fusion process, the expectations are 0.28±0.06 and 0.65±0.10 events for muons and electrons, respectively. The expectations are based on the leading order calculation and m_c =1.6 GeV/c^2 was taken.

The distributions of the selected candidates are shown in Figs. 8.1∼ 8.4 where expectation form the QPM Monte Carlo with leading order caluclation are superimposed in these figures. Here, the mass of charm quark is assumed to be 1.6 GeV/c^2. Since our data sample is statistically limited, we have tried to correct our result as partial cross sections including leptons from charm in the limitation of our detectable regions.

8.1 Correction

In order to compare the results directly with theoretical predictions, we corrected the results for the limited acceptance to obtain cross sections for inclusive leptons from charm.

8.1.1 Acceptance Correction

To ensure good lepton identification, the experiment limits the momenta to $2.0 \leq p_\ell \leq 5.0$ GeV/c and the polar angles to $|\cos\theta| \leq 0.74$ (0.73) for muons (electrons) to ensure good performance of the lepton identification. Thus, the observed leptons have a minimum transverse momentum relative to the beam line of $p_t \geq 1.5$ GeV/c. According to the Monte Carlo simulations of the direct and resolved photon processes, this corresponds to

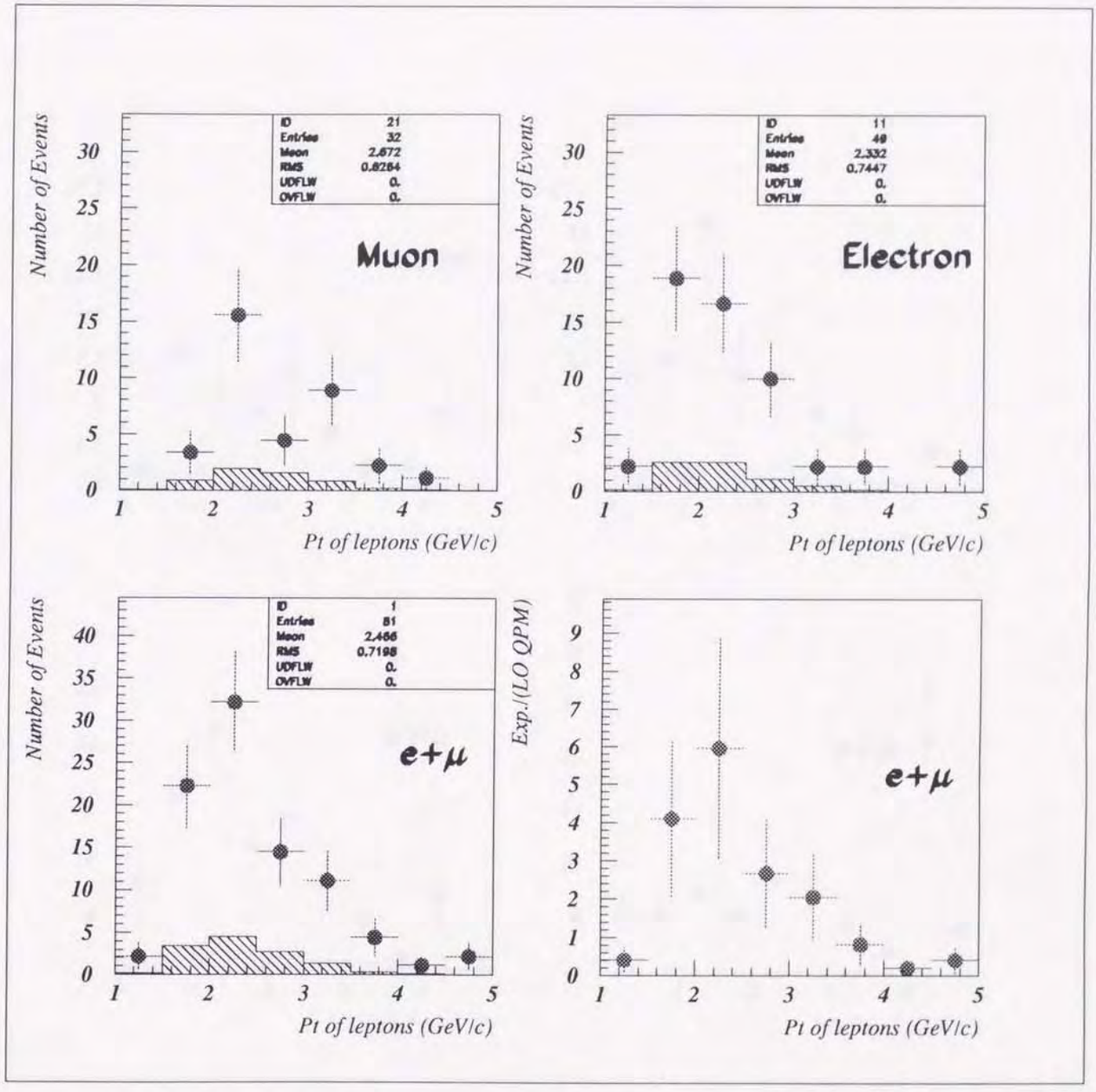

Figure 8.1: The p_t distribution of leptons, where histgram shows the LO QPM prediction with $m_c = 1.6$ GeV/c^2.

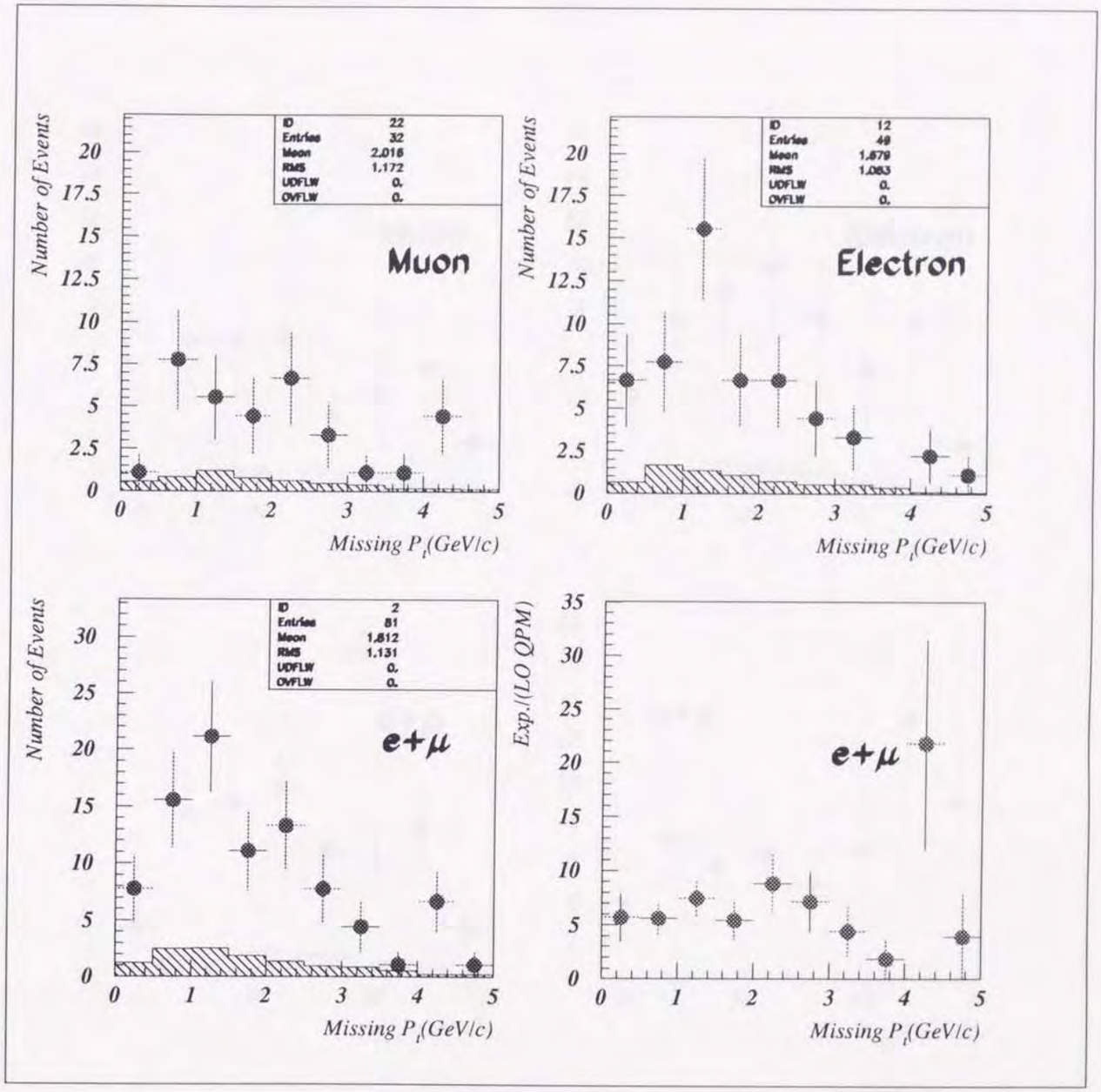

Figure 8.2: The missing p_t distribution of inclusive lepton events, where histgram shows the LO QPM prediction with $m_c = 1.6$ GeV/c^2.

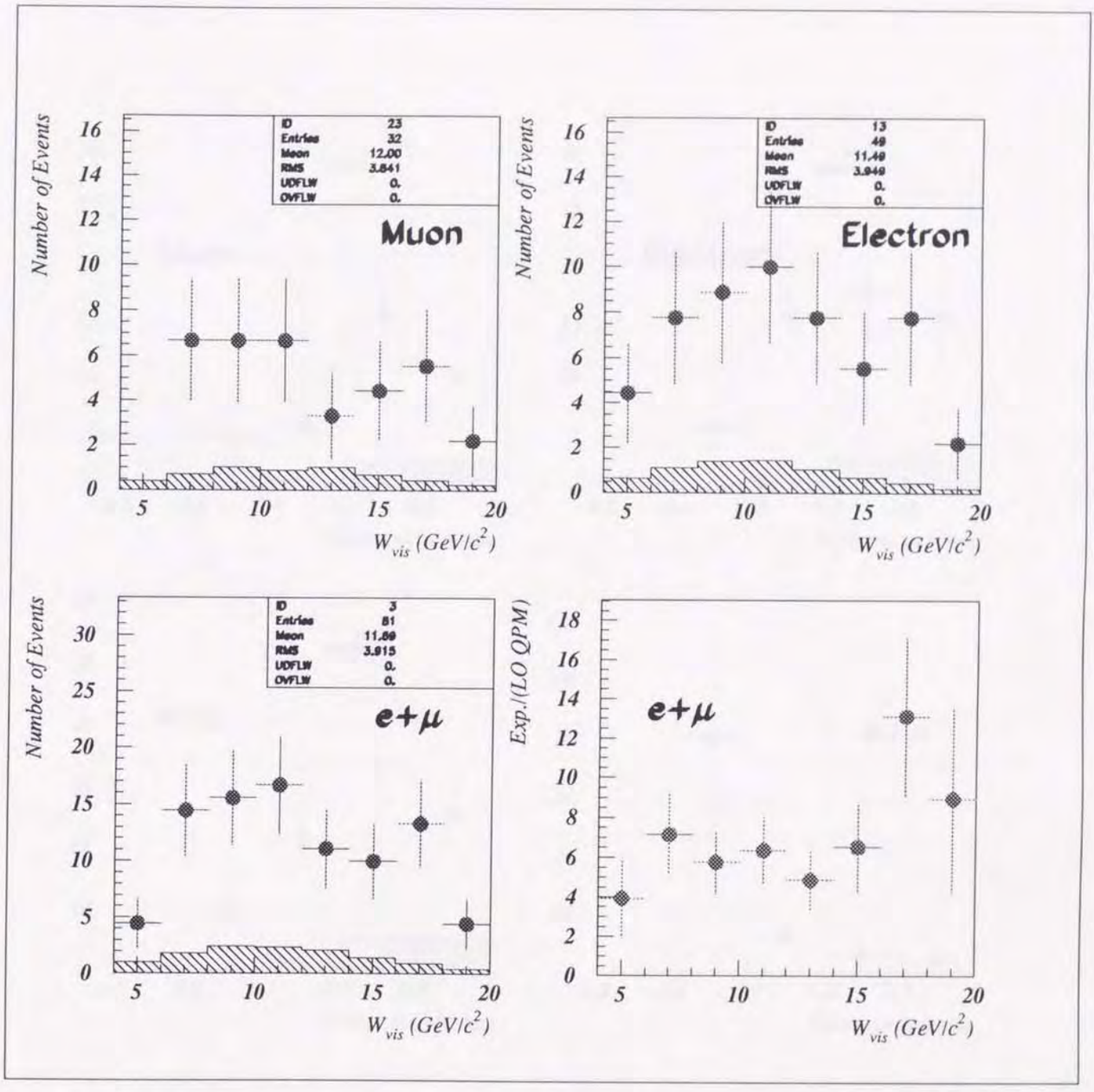

Figure 8.3: The visible invariant mass distribution of inclusive lepton events, where histgram shows the LO QPM prediction with $m_c = 1.6$ GeV/c^2.

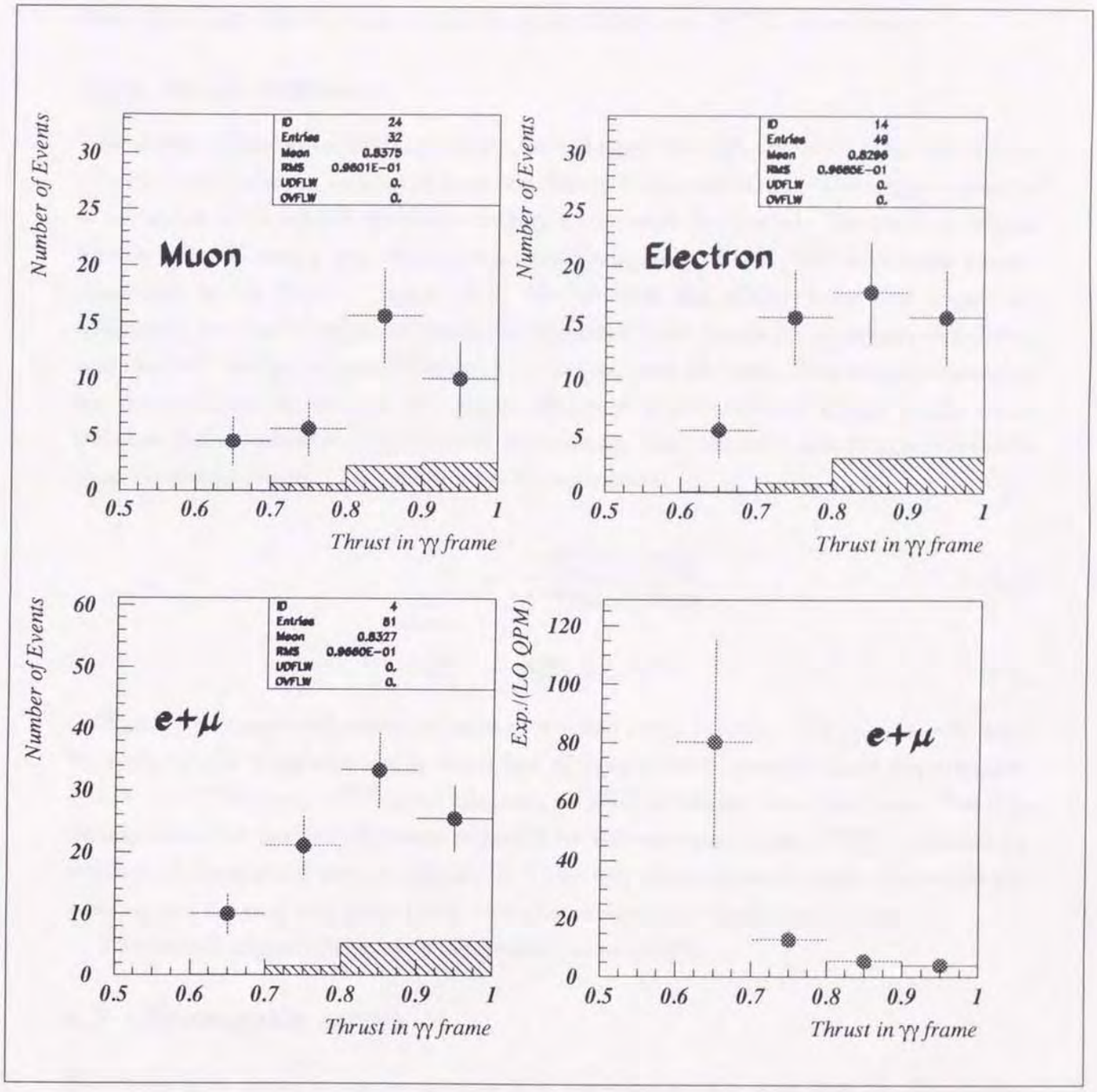

Figure 8.4: The thrust distribution of inclusive lepton events, where histgram shows the LO QPM prediction with $m_c = 1.6$ GeV/c^2.

a minimum transverse momentum of the parent D-meson (D^*,D,D_s^*, and D_s) of $P_t \geq 2.0$ GeV/c (see Fig. 8.5). The acceptances for inclusive muon and electron events, determined from these same Monte Carlo simulations, are 14.7% and 20.1%, respectively.

8.1.2 Trigger Efficiency

The detector has no redundant trigger for untagged two-photon events, so the trigger efficiency must also be estimated from the Monte Carlo simulation. The trigger patterns of the untag event sample are shown in Fig. 8.6 for each run period. The primary trigger for the selected events was derived from track segments in the CDC with some energy deposition in the SHC (Trigger 13). We estimate the efficiency for this trigger by combining the track trigger efficiency, as estimated from Monte Carlo trigger simulator, and the SHC energy trigger efficiency, as measured from the data. The trigger efficencies are derived from the ratio of the trigger efficiency of the reference trigger to the event fraction of the dominant trigger in the experiment. Here the reference trigger should be most dominant trigger. The relation for the estimation is,

$$R = \frac{N_{MC}^{Ref}}{\varepsilon^{trg} N_{MC}} = \frac{N_{EXP}^{Ref}}{N_{EXP}} \tag{8.1}$$

where

$$N_{MC}^{Ref} = N_{ITC+CDC}^{sim} \cdot \varepsilon^{SHC} \tag{8.2}$$

N_{MC} is the number of expected events for untag event sample. $N_{ITC+CDC}^{sim}$ is estimated by using trigger simulator and is a number of events which passed trigger requirements of ITC and CDC part. ε^{SHC} is the efficiency of SHC estimated from real data. The R is defined from the number of events triggered by the reference trigger (N_{EXP}^{Ref}), divided by number of untag event sample (N_{EXP}). In Table 8.1, the estimated trigger efficiencies are summarized for each run period and several combinations of reference trigger.

The overall trigger efficiency is determined to be 89.6%.

8.2 Systematic errors

The systematic errors in the measurement of the cross section arise from the luminosity determination, the trigger efficiency estimation, the background subtraction, and the determination of the acceptance correction.

The uncertainty in the luminosity determination was 1.5%.

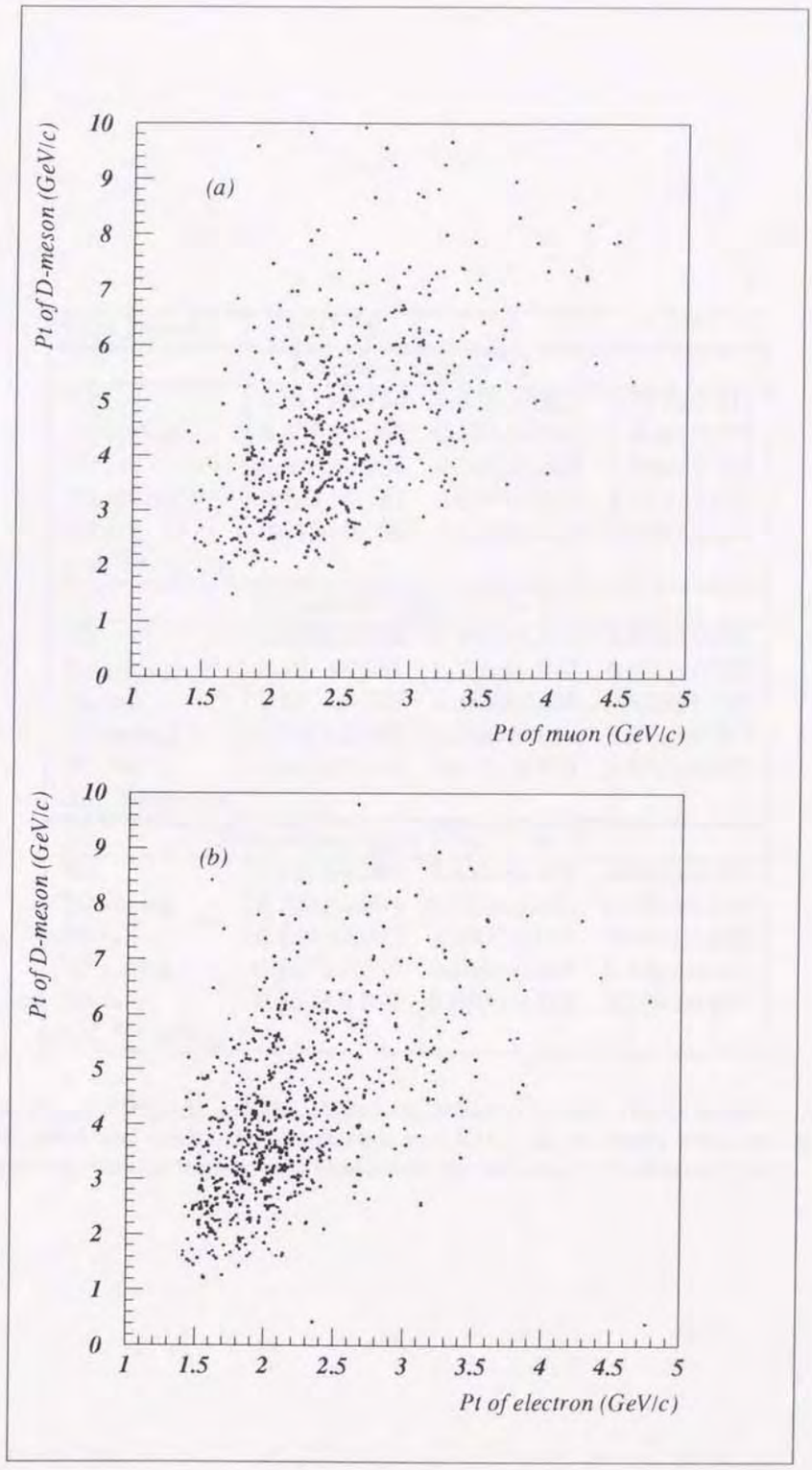

Figure 8.5: Correlation plot between the transverse momentum of selected leptons and that of D-mesons(D^*,D,D_s^*, and D_s) for (a) muons and (b) electrons. These plots were made by using Monte Carlo simulation of the direct and resolved photon processes; LAC1 parametarization was used for the gluon density.

Run Period	SHC Eff.	R	$\varepsilon^{\mathrm{trg}}$
Reference trigger 13			
'90	0.911±0.100	0.833±0.027	0.997±0.114
'92 spring	0.850±0.057	0.532±0.012	1.000±0.082
'92 fall	0.898±0.096	0.746±0.023	1.000±0.117
'93 spring	0.796±0.037	0.804±0.016	0.927±0.047
'93 fall and '94 spring	0.815±0.030	0.806±0.012	0.893±0.036
Reference trigger 13 or 18			
'90	0.824±0.059	0.845±0.027	0.895±0.079
'92 spring	0.791±0.034	0.735±0.015	0.689±0.033
'92 fall	0.877±0.072	0.860±0.025	0.910±0.080
'93 spring	0.833±0.039	0.856±0.017	0.914±0.047
'93 fall and '94 spring	0.860±0.033	0.871±0.013	0.897±0.038
Reference trigger 13 or 18 or 22			
'90	0.827±0.060	0.856±0.027	0.889±0.070
'92 spring	0.792±0.034	0.773±0.015	0.837±0.039
'92 fall	0.879±0.072	0.880±0.026	0.900±0.079
'93 spring	0.837±0.039	0.865±0.017	0.912±0.047
'93 fall and '94 spring	0.863±0.033	0.880±0.013	0.899±0.038

Table 8.1: The trigger efficiencies and SHC efficiencies estimated by using trigger simulator, where Monte Carlo of VMD, QPM, and resolve photon processes with LAC1 parton density were used for estimation. The combination of reference triggers were changed for the estimation of systematic errors.

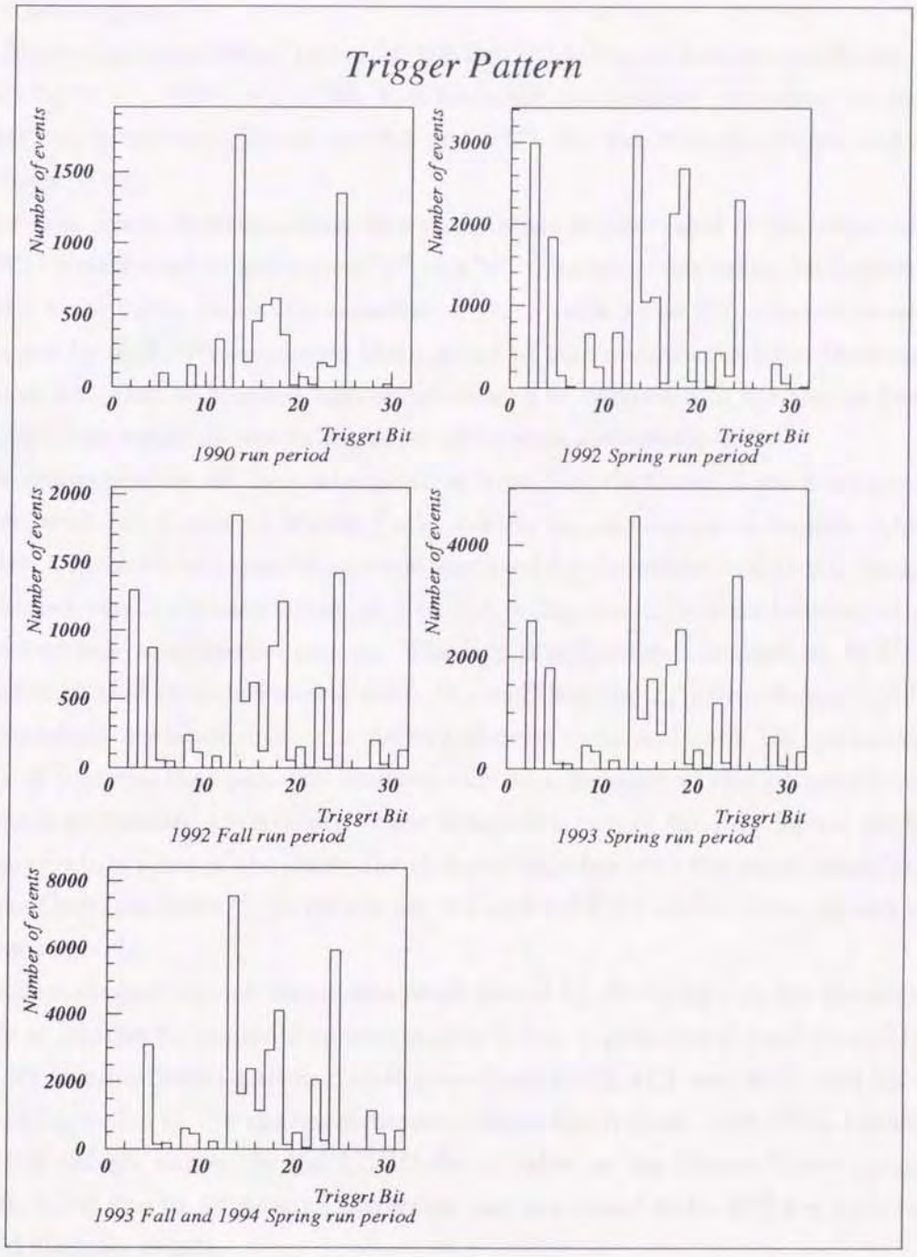

Figure 8.6: Trigger pattern of untag event sample, where both of inclusive and exclusive triggers are counted.

The error in the trigger efficiency was estimated to be 4.9% by observing the variation in the trigger efficiency when changing the criteria of the most dominant trigger by combining several track triggers.

The Monte Carlo statistical errors for the determination of background levels from the $e^+e^- \rightarrow e^+e^-\tau^+\tau^-$, $e^+e^- \rightarrow e^+e^-b\bar{b}$, and hadronic annihilation processes are treated as systematic uncertainties. These are 8.9 and 9.6% for the inclusive muon and electron events, respectively.

In the fake muon determination, the uncertainty in the value of the cross section in the GVMD model used to generate $e^+e^- \rightarrow e^+e^-$ + hadrons was taken into account. The systematic error taken to be the variation of the results when the value of cross section was changed by 50%. We compared the number of fake muons estimated from analytical calculation with that of Monte Carlo simulation. The difference in the results from these independent two methods was taken as an additional systematic error.

In the determination of the contamination from fake electrons, there is an uncertainty associated with the choice of Monte Carlo models for simulation of hadron interaction. The FLUKA Monte Carlo simulation code was used for the estimation of this background. We evaluated the systematic error of FLUKA using the E/p distributions of charged tracks in hadronic annihilation process. The E/p distributions obtained by FLUKA were compared with that of experimental data. We modified the E/p distributions of FLUKA by one standard deviation from the default distributions and took the variation of the efficiency of hadrons that pass our electron cuts as a measure of this systematic error.

The total systematic uncertainty in the determinations of the fake lepton background are the quadrature sums of the above-listed errors together with the errors associated with the Monte Carlo statistics. The results are 8.1 and 8.0% for inclusive muon and electron events, respectively.

The acceptance correction factor was recalculated by changing cuts for the acceptance boundary of leptons by amounts corresponding to the experimental resolutions (Figs. 8.7 $\sim$ 8.10), by using different parton distribution function (LAC1 and DG), and by varying the branching ratios of the charmed mesons, either the August 1994 PDG tables or the JETSET7.3 default values, in the LUND decay table as the Monte Carlo inputs. The systematic error due to acceptance correction was estimated to be 12% for both inclusive muon and electron events.

The quadratic sum of the systematic errors are 17 and 19% for inclusive muon and electron events, respectively; about half of the statistical errors.

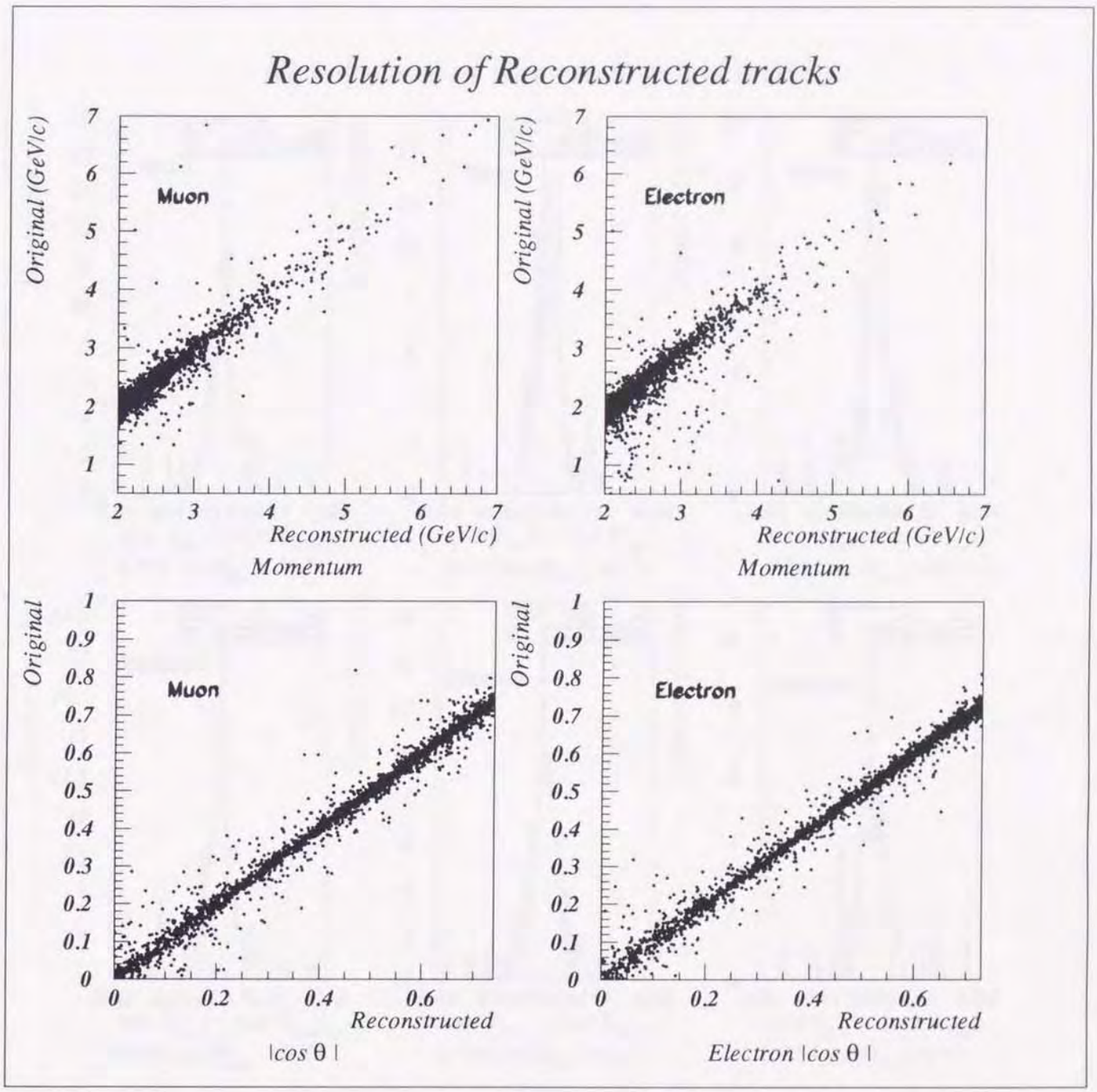

Figure 8.7: Comparison of reconstructed lepton tracks with thoes of generator level in the QPM Monte Carlo events.

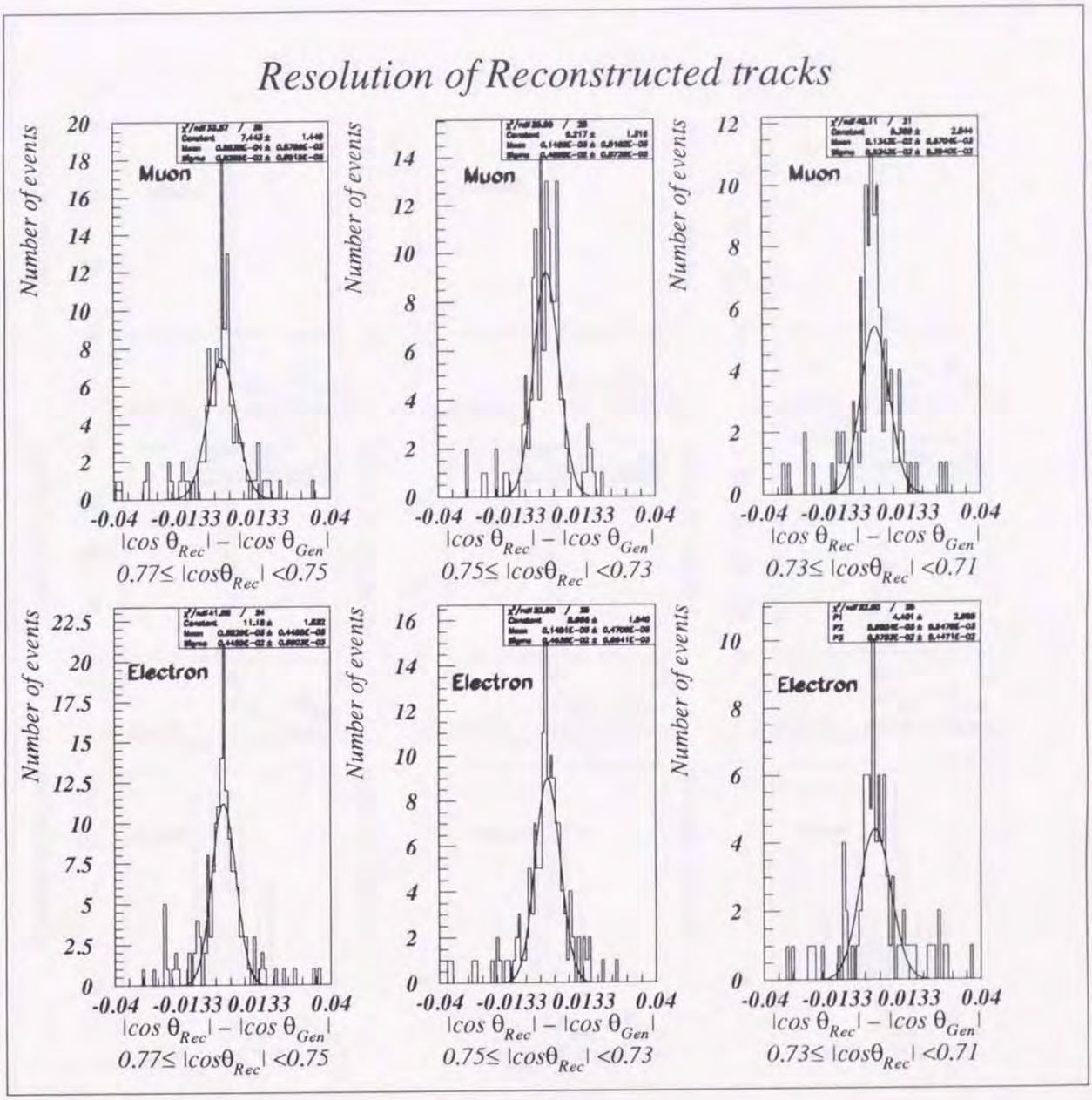

Figure 8.8: The difference between reconstructed angle and generated one for muons(top) and electrons(bottom).

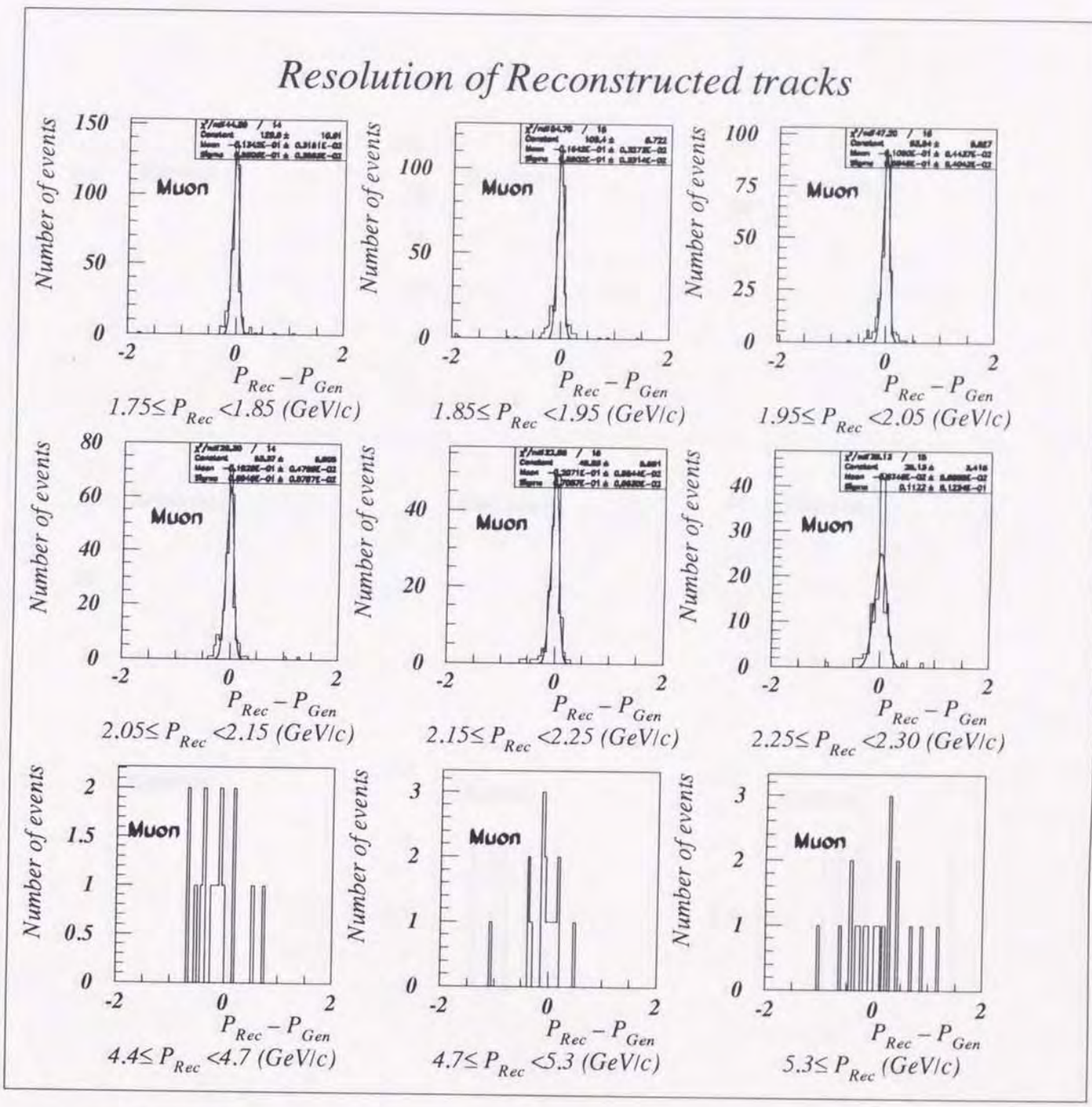

Figure 8.9: The difference between reconstructed muon momentum and generated one for various momentum ranges.

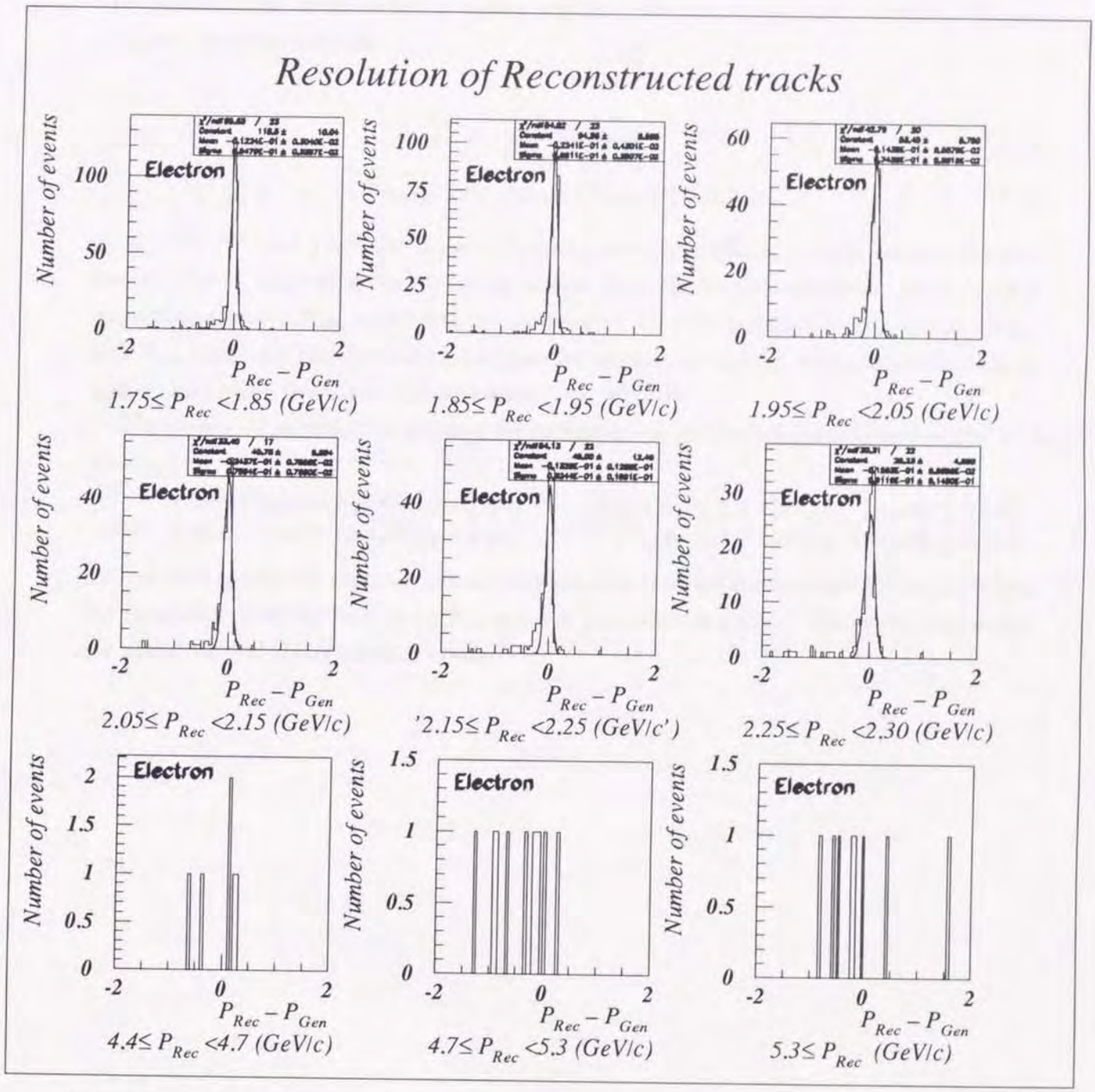

Figure 8.10: The difference between reconstructed electron momentum and generated one for various momentum ranges.

8.3 Cross section

The partial cross sections for inclusive leptons from charm $\sigma(e^+e^- \rightarrow e^+e^-\ell^{\pm}X)$ are obtained from the relation

$$\sigma_\ell = \frac{N_{prompt}}{\varepsilon^{trg}\varepsilon^{det}\int Ldt} \tag{8.3}$$

$$N_{prompt} = N_{obs} - (N_{fake} + \varepsilon^{trg}N_{oth}), \tag{8.4}$$

where ε^{trg}, ε^{det}, and $\int Ldt$ are trigger efficiency, detection efficiency, and integrated luminosity. The number of inclusive lepton events from charm are calculated using Eq. 8.4 respectively, where N_{obs} represents the number of selected inclusive lepton events. N_{fake} and N_{oth} stand for the number of background events, caused by wrong identification of leptons and come from the other processes, respectively.

The measured partial cross sections for inclusive leptons from charm $\sigma(e^+e^- \rightarrow e^+e^-\ell^{\pm}X)$ are:

$0.53\pm0.16(stat.)\pm0.09(syst.)$ pb $\quad (2.0 \leq p_\mu \leq 5.0$ GeV/c, $|\cos\theta| \leq 0.74)$

and $0.46\pm0.14(stat.)\pm0.09(syst.)$ pb $\quad (2.0 \leq p_e \leq 5.0$ GeV/c, $|\cos\theta| \leq 0.73)$

for inclusive muon and electron events, respectively. The total errors are 35% and 36% of the measured cross sections for inclusive muon and electron events. The systematic errors are about 60% of the statistical errors.

Chapter 9

Results and Discussion

9.1 Comparison with theoretical predictions

The measured cross sections and theoretical predictions are summarized in Table 9.1. Fig. 9.1 shows our measurements and theoretical predictions of the incoherent sum of the direct and photon-gluon fusion processes. In these calculations, we used the LAC1, DG, and WHIT4 model calculations for the gluon density.

The results of the calculations in Table 9.1 indicate that the resolved photon contribution process is only 10 to 30% of the direct process, depending on the parton density function used for the photon. In these calculations, resolved photon processes give a softer charm-quark momentum distribution than that of direct process, which correspondingly leads to a softer lepton momentum distribution. This reduces the contribution of the resolved photon process for the lepton momentum region covered by this experiment. Consequently, the sum of the direct and the resolved photon process does not change significantly for the quite different gluon distribution functions of LAC1, DG, and WHIT4. The sum of the muon and electron results is 1.8 standard deviation larger than the prediction with the WHIT4 distribution function; this excess becomes somewhat larger if the LAC1 or DG densities are used.

We have examined the effects of the mass and fragmentation parameter of the charm quark on the theoretical prediction of the cross sections.

9.1.1 Charm mass

A lower mass gives a higher cross section and vice versa. The effect is more pronounced in the low momentum region. In the high momentum region covered by this measurement, the effect of lowering the charm quark mass from 1.6 to 1.3 GeV/c^2 is about a 10% increase in the cross section. The cross section calculations using a charm quark mass of

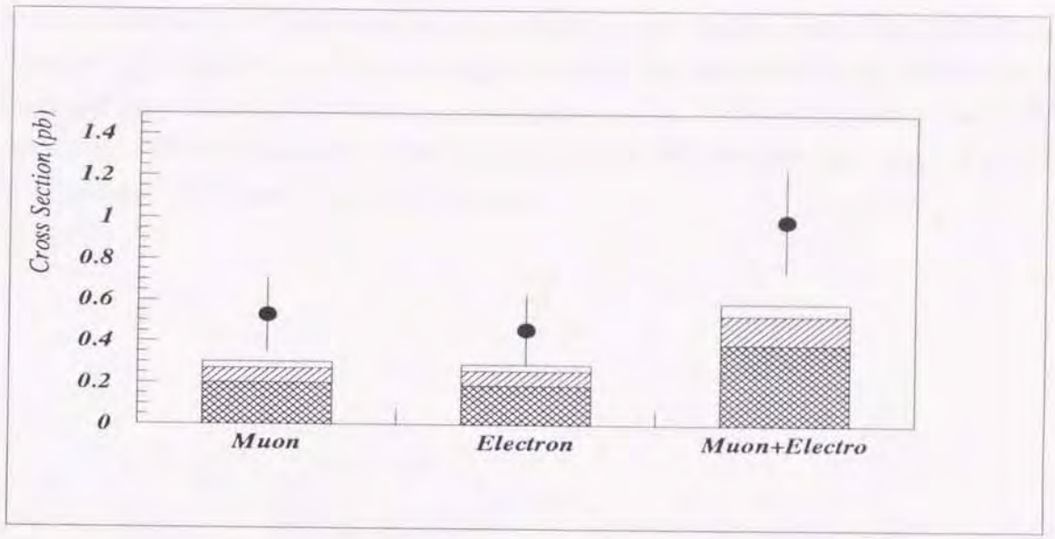

Figure 9.1: Cross section of inclusive leptons from charm. The closed circle shows the experimental data. The cross-hatched area shows the prediction for direct process. The singly-hatched area shows the prediction for the photon-gluon fusion process with WHIT4 parton density, where the charm quark mass is assumed to be 1.6 GeV. The open area shows the increase of cross section due to the lighter charm quark mass of 1.3 GeV. The NLO QCD correction is included in these predictions. The error bar is the combined statistical and systematic uncertainty.

1.3 GeV/c^2 are summarized in Table 9.2.

9.1.2 Fragmentation parameter

Using a harder fragmentation function for the transition of the charm quark to hadrons, which corresponds to a smaller fragmentation parameter ε_c, makes the predicted cross sections larger at high transverse momentum region, since the transverse momenta of the parent D meson is correlated with that of the lepton. The variation of fragmentation function for several parameters are shown in Fig. 9.2.

We changed the value of fragmentation parameter to 0.028 from the chosen value of 0.047, according to the ALEPH group's measurement [39]. This increases the cross sections by 15 and 12% for the inclusive muons and electrons, respectively.

9.2 Comparison with TOPAZ measurement

The TOPAZ group has measured the inclusive electron cross section as a function of the electron transverse momentum [7]. Since the momentum range and solid angle acceptance of the two experiments differ, the results can not be compared directly. We extrapolate

our cross section for inclusive electron from charm to the region covered by TOPAZ using a Monte Carlo simulation of the direct process. For this comparison, the transverse momenta and polar angles of electrons are limited to $1.5 \leq p_t \leq 3.0$ GeV/c and $|\cos\theta| \leq 0.77$, respectively. Our extrapolated cross section is about 30% smaller than that of TOPAZ, but consistent within one standard deviation.

Mode		Muons (pb)	Electrons (pb)
Measured		0.53 ± 0.16 ± 0.09	0.46 ± 0.14 ± 0.09
Direct			
QPM	LO	0.149 ± 0.002	0.145 ± 0.002
	NLO	0.198 ± 0.003	0.194 ± 0.003
Resolved			
LAC1	LO	0.021 ± 0.002	0.019 ± 0.001
	NLO	0.044 ± 0.003	0.041 ± 0.003
DG	LO	0.010 ± 0.001	0.011 ± 0.001
	NLO	0.024 ± 0.002	0.028 ± 0.002
WHIT4	LO	0.030 ± 0.002	0.028 ± 0.002
	NLO	0.072 ± 0.004	0.065 ± 0.004
Direct+Resolved			
QPM+LAC1	LO	0.170 ± 0.003	0.164 ± 0.002
	NLO	0.242 ± 0.004	0.235 ± 0.004
QPM+DG	LO	0.159 ± 0.002	0.156 ± 0.002
	NLO	0.222 ± 0.004	0.222 ± 0.004
QPM+WHIT4	LO	0.179 ± 0.003	0.173 ± 0.003
	NLO	0.270 ± 0.005	0.259 ± 0.005

Table 9.1: Cross sections for inclusive leptons from charm $\sigma(e^+e^- \rightarrow e^+e^-\ell^{\pm}X)$ measured by this experiment and theoretical predictions with a charm quark mass of 1.6 GeV/c^2. The first and second errors denote the statistical and systematic errors, respectively.

Mode		Muons (pb)	Electrons (pb)
Direct			
QPM	LO	0.163 ± 0.004	0.152 ± 0.004
	NLO	0.227 ± 0.005	0.213 ± 0.005
Resolved			
LAC1	LO	0.0259 ± 0.0004	0.028 ± 0.003
	NLO	0.058 ± 0.008	0.062 ± 0.008
WHIT4	LO	0.034 ± 0.002	0.032 ± 0.002
	NLO	0.076 ± 0.004	0.076 ± 0.005
Direct+Resolved			
QPM+LAC1	LO	0.189 ± 0.004	0.180 ± 0.005
	NLO	0.285 ± 0.009	0.275 ± 0.009
QPM+WHIT4	LO	0.197 ± 0.004	0.184 ± 0.004
	NLO	0.303 ± 0.006	0.289 ± 0.007

Table 9.2: Cross sections for inclusive leptons from charm $\sigma(e^+e^- \rightarrow e^+e^-\ell^{\pm}X)$ predicted theoretically with a charm quark mass of 1.3 GeV/c^2.

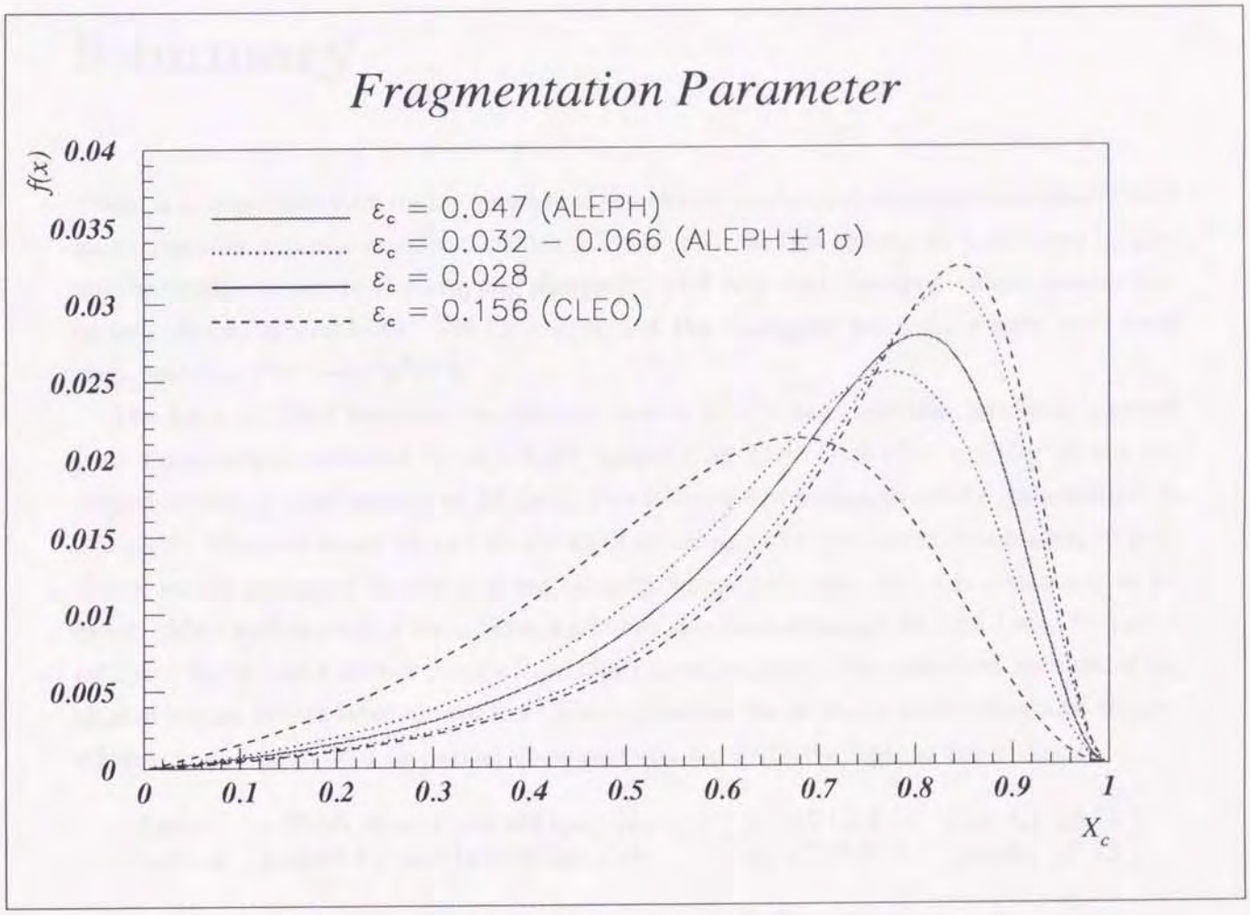

Figure 9.2: The Peterson fragmentation function for various ε_c values. The a couple of dotted lines shows the value when the ε_v was varied one standard deviation from ALEPH value.

Chapter 10

Summary

There is a long history on measurements of the charm production cross section which claim an excess over expectations, but statistically limited. In this thesis, we have tried to give another contribution to the ongoing discussion and reported the open charm production in two-photon interactions. We have analyzed the untagged hadronic events with final state leptons, $e^+e^- \rightarrow e^+e^-\ell^{\pm}X$.

The total of 25820 hadronic two-photon events with untag condition has been selected from data sample collected by the AMY detector at TRISTAN e^+e^- collider at the averaged center of mass energy of 58 GeV. The integrated luminosity of the data sample is 275 pb^{-1}. We have found 32 and 49 inclusive muon and electron event candidates, respectively, in the untagged hadronic event sample, where only one lepton is contained in an event. After subtraction of various backgrounds, we have obtained 18.5±6.1 and 22.1±7.5 inclusive muon and electron events from charm, respectively. The observed number of inclusive lepton events from charm have been corrected for detector acceptance and trigger efficiency, and presented as partial cross sections for inclusive leptons from charm:

Muon	$0.53\pm0.16(stat.)\pm0.09(sys.)$ pb	($2\leq p_\mu \leq 5$ GeV/c, $\lvert\cos\theta_\mu\rvert \leq 0.74$)
Electron	$0.46\pm0.14(stat.)\pm0.09(sys.)$ pb	($2\leq p_e \leq 5$ GeV/c, $\lvert\cos\theta_e\rvert \leq 0.73$)

The measurements are compared with various predictions of quark parton model and resolved photon process including next-to-leading order QCD corrections. The measured cross section is 1.8 standard deviations higher than the theoretical prediction based on the direct and photon-gluon fusion processes with WHIT4 parton density function, where the mass of charm quark is assumed to be 1.6 GeV/c^2, and next-to-leading order QCD corrections are taken into account. However by choosing lighter mass of charm quark (m_c=1.3 GeV/c^2) and harder fragmentation parameter (ε_c=0.028), the deviation of measurement from expectation becomes small, and is 1.3 standard deviations.

Our result of inclusive electron analysis has been also compared with the electron inclusive cross section measured by TOPAZ [7]. Our cross section is about 30% smaller than that of TOPAZ, but consistent within one standard deviation.

Although we have measured the cross section for inclusive lepton form high transvers momentum charm with better precision than the previous experiments, we still can not ultimately clarify the existence of an excess due to the limited statistical precision. However our measurement indicates some excess over theoretical predictions at high transverse momenta.

Bibliography

[1] TASSO Collab., W.Braunschweig et al., *Z. Phys.* **C47** (1990) 499.

[2] TPC/2-Gamma Collab., M.Alston-Garnjost et al., *Phys. Lett.* **B252** (1990) 499.

[3] JADE Collab., W.Bartel et al., *Phys. Lett.* **B184** (1987) 288.

[4] M.Drees, M.Krämer, J.Zunft, and P.M.Zerwas, *Phys. Lett.* **B306** (1993) 371.

[5] S.J.Brodsky, T.A.DeGrand, J.F.Gunion, and J.H.Weis, *Phys. Rev. Lett.* **41** (1978) 672; *Phys. Rev.* **D19** (1979) 1418;
H.Terazawa, *J. Phys. Soc. Jpn.* **47** (1979) 355;
K.Kajantie and R.Raitio, *Nucl. Phys.* **B159** (1979) 528;
M.Drees and R.M.Godbole, *Nucl. Phys.* **B339** (1990) 355.

[6] VENUS Collab., S.Uehara et al, *Z. Phys.* **C63** (1994) 213.

[7] TOPAZ Collab., M.Iwasaki et al, *Phys. Lett.* **B341** (1994) 99.

[8] TOPAZ Collab., R.Enomoto et al, *Phys. Rev.* **D50** (1994) 1879;
TOPAZ Collab., R.Enomoto et al, *Phys. Lett.* **B328** (1994) 535.

[9] ALEPH Collab., D.Buskulic et al., *Phys. Lett.* **B355** (1995) 595.

[10] B.Margolis, *Phys. Rev.* **D17** (1978) 1310;
I.F.Ginzburg and V.G.Selbo, *Phys. Lett.* **B109** (1982) 231.

[11] N. Arteaga-Romero, A.Jaccarini, and P. Kesser, *C.R. Acad. Sci.* **B269** (1969) 153 ;
V.E. Balakin, V.M. Bundev, and I.F. Ginzgurg, *Zh. Eksp. Teor. FIz. Pis'ma Red.* **11** (1970) 559 ;
S.J. Brodsky, T. Kinoshita, and H. Terazawa, *Phys. Rev. Lett.* **25** (1970) 972.

[12] T.F. Walsh, *Phys. Lett.* **B36** (1971) 121;
S.Brodsky, T.Kinoshita, and H.Terazawa, *Phys. Rev. Lett.* **27** (1971) 280 ;

S.M.Berman, J.D.Bjorken, and J.B.Kogut, *Phys. Rev.* **D4** (1971) 3388;
P.Zerwas and T.F.Walsh, *Phys. Lett.* **B44** (1973) 195.

[13] E.Witten, *Nucl. Phys.* **B120** (1977) 189.

[14] V.M.Budnev et al., *Phys. Rep.* **15** (1974) 181.

[15] Ch. Berger et al., *Phys. Rep.* **146** (1987) 1.

[16] J.H.Field et al., *Nucl. Phys.* **B168** (1980)477;
J.H.Field et al., *Nucl. Phys.* **B176** (1980)545.

[17] J.J.Sakurai and D.Schildknecht, *Phys. Lett.* **B41** (1972)489.

[18] TPC/Two-Gamma Collab. H.Aihara et al, *Phys. Rev.* **D42** (1990)2667.

[19] S.J.Brodsky, T.Kinoshita, and H.Terazawa, *Phys. Rev.* **D4** (1971) 1532.

[20] M.Drees and R.M.Godbole, MADPH-95-898.

[21] Private communication with M.Drees, M.Krämer, and J.Zunft.

[22] TRISTAN Project Group, KEK Report 86-14 (1987).

[23] AMY Collab., T.Kumita et al., *Phys. Rev.* **D42** (1990) 1339;
AMY Collab., F.Liu et al., *Phys. Rev.* **D49** (1994) 4339.

[24] Y.Doi et al, *Nucl.Instr.Methods* **A274** (1989) 95.

[25] F.Kajino,A.Abashian and K.Gotow, *Nucl.Instrum.Methods* **A245**,507(1986).

[26] S.S.Myung,Ph.D thesis, *Korea Univ.*,(1988).

[27] Y.Sakai, *Proceeding of the Workshop on Triggering and Data Acquisition for Experiments at the Supercollider.*,**SSC-SR-1039** (1989).

[28] S.Lusin, *Proceeding of Symposium on Data Acquisition and processing for Next Generation Experiments.*,**KEK Report 89-26** (1989).

[29] W.R.Nelson et al., SLAC-Report-265(1985).

[30] H. Fesenfld., *Aachen Univ.* **PHITHA 85/O2**,(1975).

[31] S.Kawabata, *Comput. Phys. Commun.* **41** (1986) 127.

[32] T.Sjöstrand, CERN-TH-6488-92 (May 1992);
T.Sjöstrand and M.Bengtsson, *Comput. Phys. Commun.* **43** (1987) 367.

[33] M. Kuroda, Meiji Gakuen Univ. *Research J.* **27** (1988) 424.

[34] H.Abramowicz, K.Charchula, and A.Levy, *Phys. Lett.* **B269** (1991) 458.

[35] M.Drees and K.Grassie, *Z. Phys.* **C28** (1985) 451.

[36] K.Hagiwara, M.Tanaka, I.Watanabe, and T.Izubuchi, *Phys. Rev.* **D51** (1995) 3197.

[37] M.Glück, E.Reya, and A.Vogt, *Phys. Rev.* **D46** (1992) 1973;
M.Glück, E.Reya, and A.Vogt, *Phys. Rev.* **D45** (1992) 3986.

[38] C.Peterson, D.Schlatter, I.Schmitt, and P.M.Zerwas, *Phys. Rev.* **D27** (1983) 105.

[39] ALEPH Collab., D.Decamp et al., *Phys. Lett.* **B266** (1991) 218.

[40] Review of Particle Properties, *Phys. Rev.* **D50** (1994) 1172.

[41] AMY Collab., R.Tanaka et al., *Phys. Lett.* **B277** (1992) 215.

[42] AMY Collab., B.J.Kim et al., *Phys. Lett.* **B325** (1994) 248.

[43] T.Mori, *Ph.D. Thesis, University of Rochester*, **UR-1104** (1988).

[44] D.G.Cassel and M.Ogg, *"DUET-A Track-Finding Program for Cylindrical Geometries"*, **CLEO Internal Report** (1983).

[45] F.A.Harris et al., *Nucl. Instrum. Methods.* **103** (1972) 345.

[46] A.Fassò et al., *Nucl. Instrum. Methods.* **A332** (1993) 459;
P.A.Aarnio et al., *Proceedings of MC93* (1993) 88.

Appendix A

Cross sections

- The cross sections for the di-lepton production are given as follows,
  - Two-photon process:

$$\sigma(e^+e^- \to e^+e^-\mu^+\mu^-) = \frac{28\alpha^4}{27\pi m_\ell^2}\left(\ln\frac{s}{m_e^2}\right)^2 \ln\frac{s}{m_\ell^2} \tag{A.1}$$

  - Annihilation process:

$$\sigma(e^+e^- \to \mu^+\mu^-) = \frac{4\pi\alpha^2}{3s} \tag{A.2}$$

- Deep inelastic electron scattering on a real photon target:

$$\left.\frac{d\sigma}{dE_{tag}\,d\cos\theta_{tag}}\right|_{e\gamma\to eX} = \frac{4\pi\alpha^2 E_{tag}}{Q^4 y}[1+(1-y)^2F_2(x,Q^2)-y^2F_L(x,Q^2)] \tag{A.3}$$

with (A.4)

$$y = 1-\frac{E_{tag}}{E_{beam}}\cos^2\left(\frac{\theta_{tag}}{2}\right) \tag{A.5}$$

$$x = \frac{Q^2}{Q^2+W^2} \tag{A.6}$$

$$Q^2 = 4E_{tag}E_{beam}\sin^2\left(\frac{\theta_{tag}}{2}\right) \tag{A.7}$$

(A.8)

where E_{beam} is the beam energy and W is the center-of-mass energy in photon-photon frame. E_{tag} and θ_{tag} are scattered electron energy and its theta angle, respectively. F_2 and F_L are structure functions of photon which are strictly related to the parton density of the inside of photon. The variable x and y are Bjorken variable.

Appendix B

Subprocess Cross Sections

The subprocess cross sections are given in this appendix.

- The direct process:
  1) $\gamma\gamma \to q\bar{q}$;

$$\frac{d\hat{\sigma}}{d\hat{t}} = 3e_q^4 \frac{2\pi\alpha^2}{\hat{s}^2}\left(\frac{\hat{t}}{\hat{u}} + \frac{\hat{u}}{\hat{t}}\right) \tag{B.1}$$

- A couple of types of subprocess for three jets in two-photon processes:
  1) $\gamma g \to q\bar{q}$;

$$\frac{d\hat{\sigma}}{d\hat{t}} = \frac{\pi\alpha\alpha_s e_q^2}{\hat{s}^2}\left(\frac{\hat{u}}{\hat{t}} + \frac{\hat{t}}{\hat{u}}\right) \tag{B.2}$$

  2) $\gamma q \to qg$;

$$\frac{d\hat{\sigma}}{d\hat{t}} = -\frac{8\pi\alpha\alpha_s e_q^2}{3\hat{s}^2}\left(\frac{\hat{t}}{\hat{s}} + \frac{\hat{s}}{\hat{t}}\right) \tag{B.3}$$

- 8 different types of subprocess producing four jets in two-photon process:
  1) $q_1q_2 \to q_1q_2$ or $q_1\bar{q}_2 \to q_1\bar{q}_2$;

$$\frac{d\hat{\sigma}}{d\hat{t}} = \frac{\pi\alpha_s^2}{\hat{s}^2}\left\{\frac{4}{9}\left(\frac{\hat{s}^2 + \hat{u}^2}{\hat{t}^2}\right)\right\} \tag{B.4}$$

  2) $q_1q_1 \to q_1q_1$;

$$\frac{d\hat{\sigma}}{d\hat{t}} = \frac{\pi\alpha_s^2}{\hat{s}^2}\left\{\frac{4}{9}\left(\frac{\hat{s}^2 + \hat{u}^2}{\hat{t}^2} + \frac{\hat{s}^2 + \hat{t}^2}{\hat{u}^2}\right) - \frac{8}{27}\left(\frac{\hat{s}^2}{\hat{u}\hat{t}}\right)\right\} \tag{B.5}$$

3) $q_1\bar{q}_1 \to q_2\bar{q}_2$;

$$\frac{d\hat{\sigma}}{d\hat{t}} = \frac{\pi\alpha_s^2}{\hat{s}^2}\left\{\frac{4}{9}\left(\frac{\hat{t}^2+\hat{u}^2}{\hat{s}^2}\right)\right\} \tag{B.6}$$

4) $q_1\bar{q}_1 \to q_1\bar{q}_1$;

$$\frac{d\hat{\sigma}}{d\hat{t}} = \frac{\pi\alpha_s^2}{\hat{s}^2}\left\{\frac{4}{9}\left(\frac{\hat{s}^2+\hat{u}^2}{\hat{t}^2}+\frac{\hat{u}^2+\hat{t}^2}{\hat{s}^2}\right)-\frac{8}{27}\left(\frac{\hat{u}^2}{\hat{s}\hat{t}}\right)\right\} \tag{B.7}$$

5) $q\bar{q} \to gg$;

$$\frac{d\hat{\sigma}}{d\hat{t}} = \frac{\pi\alpha_s^2}{\hat{s}^2}\left\{\frac{32}{27}\left(\frac{\hat{u}^2+\hat{t}^2}{\hat{u}\hat{t}}\right)-\frac{8}{3}\left(\frac{\hat{u}^2+\hat{t}^2}{\hat{s}^2}\right)\right\} \tag{B.8}$$

6) $gg \to q\bar{q}$;

$$\frac{d\hat{\sigma}}{d\hat{t}} = \frac{\pi\alpha_s^2}{\hat{s}^2}\left\{\frac{1}{6}\left(\frac{\hat{u}^2+\hat{t}^2}{\hat{u}\hat{t}}\right)-\frac{3}{8}\left(\frac{\hat{u}^2+\hat{t}^2}{\hat{s}^2}\right)\right\} \tag{B.9}$$

7) $qg \to qg$;

$$\frac{d\hat{\sigma}}{d\hat{t}} = \frac{\pi\alpha_s^2}{\hat{s}^2}\left\{-\frac{4}{9}\left(\frac{\hat{u}^2+\hat{s}^2}{\hat{u}\hat{s}}\right)+\left(\frac{\hat{u}^2+\hat{s}^2}{\hat{t}^2}\right)\right\} \tag{B.10}$$

8) $gg \to gg$;

$$\frac{d\hat{\sigma}}{d\hat{t}} = \frac{\pi\alpha_s^2}{\hat{s}^2}\left\{\frac{2}{9}\left(3-\frac{\hat{u}\hat{t}}{\hat{s}^2}-\frac{\hat{u}\hat{s}}{\hat{t}^2}-\frac{\hat{t}\hat{s}}{\hat{u}^2}\right)\right\} \tag{B.11}$$

Feynman diagrams of quark-gluon scattering and gluon-gluon are shown in the Fig. B.1.

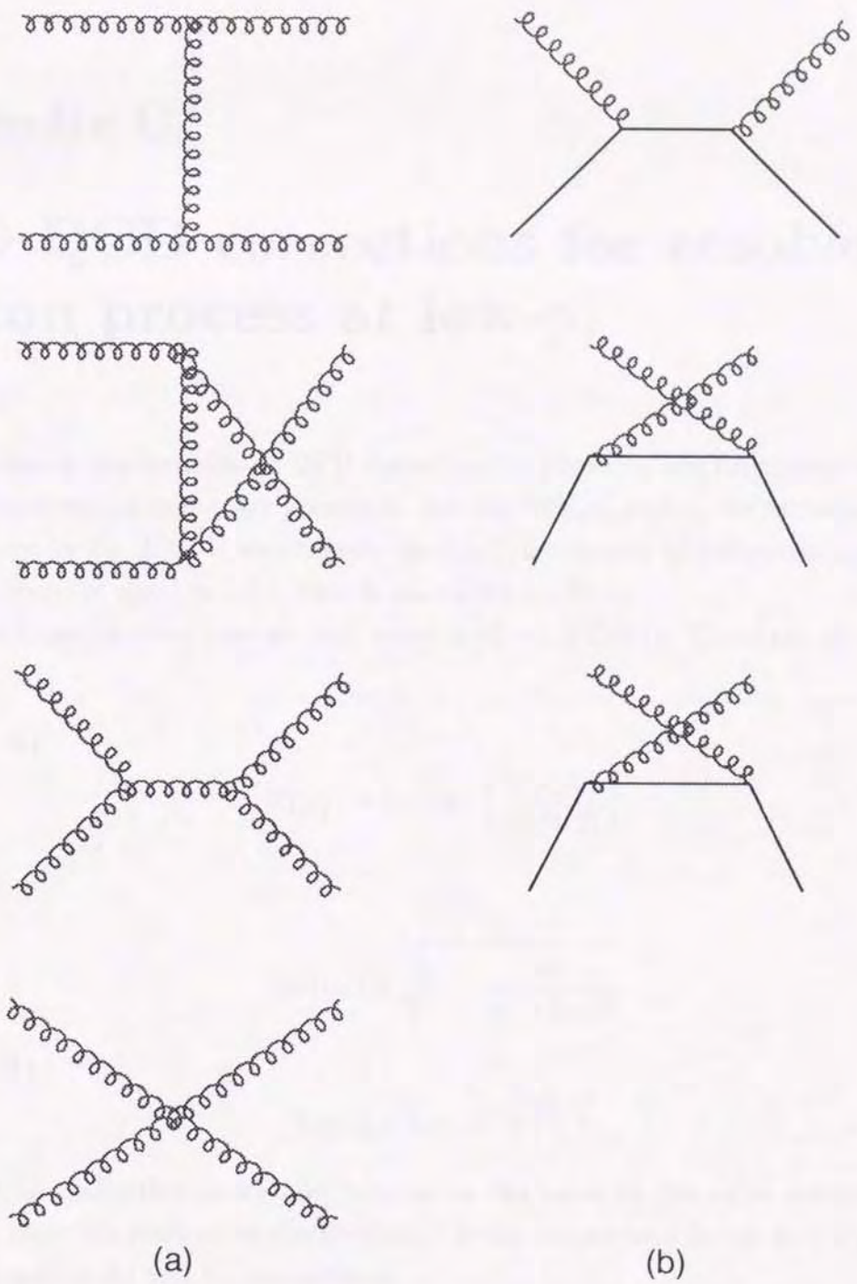

Figure B.1: The lowest-order diagrams contributing to (a) gluon-gluon scattering and (b) quark-gluon scattering.

Appendix C

NLO QCD corrections for resolved photon process at low-p_T^c

In this appendix, the formulae of QCD correction for photon-gluon fusion process at low transverse momentum region are presented. For the high-p_T^c region, the formula of $K(p_T^c)$ factor is given by Eq. 2.33. If we integrate the $K(p_T^c)$ factor over all transverse momentum regions, it becomes equal to 1.12. This is calculated by Drees.

The two formulae given here are only valid at p_T^c <1.2 GeV/c. There are two different forms,

Function A)

$$K(p_T^c) = 1.1 \cdot N \cdot \left(\frac{V_T(p_T^c)}{V_T(1.2)} \right)^f \tag{C.1}$$

where

$$V_T(p_T) = \sqrt{1 - \frac{m_c^2}{m_c^2 + (p_T)^2}} \tag{C.2}$$

Function B)

$$K(p_T^c) = 1.1 \cdot N \cdot \left(\frac{p_T^c}{1.2} \right)^f \tag{C.3}$$

N is the normalization factor and have to be the same as the value determined by Eq. 2.33 to maintain continuous distribution. f is the suppression factor and is about 10 and 7 for Function A) and B), respectively.

Appendix D

Name List of AMY Collaboration

T.Aso [a], H.Miyata [a], T.Sasaki [c], K.Miyano [a], N.Nakajima [a], K.Ohkubo [a], M.Oyoshi [a], M.Sato [a], M.Shirai [a], N.Takashimizu [a], Y.Yamashita [b], K.Abe [c], Y.Fujii [c], Y.Kurihara [c], M.H.Lee [c], F.Liu [c], A.Maki [c], T.Nozaki [c], T.Omori [c], H.Sagawa [c], Y.Sakai[c], Y.Sugimoto [c], Y.Takaiwa [c], S.Terada [c], P.Kirk [d], T.J.Wang [e], A.Abashian [f], K.Gotow [f], L.Piilonen[f], S.K.Choi [g], C.Rosenfeld [h], L.Y.Zheng [h], R.E.Breedon [i], Winston Ko [i], R.L.Lander [i], J.Rowe [i], J.R.Smith [i], S.Kanda [j], S.L.Olsen [j], K.Ueno [j], R.Tanaka [k], F.Kajino [l], S.Behari [m], H.Fujimoto [m], S.Kobayashi [m], A.Murakami [m], S.K.Sahu [m,t], M.Yang [m], S.Matsumoto [n], S.Schnetzer [o], A.Bodek [p], B.J.Kim [p], J.S.Kang [q], D.Y.Kim [q], K.B.Lee [q], H.S.Ahn [r], S.K.Kim [r], S.S.Myung [r], and D.Son [s]

[a] *Niigata University, Niigata 950-21, Japan*
[b] *Nihon Dental College, Niigata 951, Japan*
[c] *KEK, National Laboratory for High Energy Physics, Ibaraki 305, Japan*
[d] *Louisiana State University,Baton Rouge,LA 70803, USA*
[e] *Institute of High Energy Physics, Beijing 100039, China*
[f] *Virginia Polytechnic Institute and State University, Blacksburg,VA 24061, USA*
[g] *Gyeongsang National University, Chinju 660-701, South Korea*
[h] *University of South Carolina, Columbia, SC 29208, USA*
[i] *University of California, Davis, CA 95616, USA*
[j] *University of Hawaii, Honolulu, HI 96822, USA*
[k] *Japan Synchrotron Radiation Research Institute, Hyogo, 679-41, Japan*
[l] *Konan University, Kobe 658, Japan*
[m] *Saga University, Saga 840, Japan*
[n] *Chuo University, Tokyo 112, Japan*
[o] *Rutgers University, Piscataway, NJ 08854, USA*
[p] *University of Rochester, Rochester, NY 14627, USA*
[q] *Korea University, Seoul 136-701, South Korea*
[r] *Seoul National University, Seoul 151-742, South Korea*
[s] *Kyungpook National University, Taegu 702-701, South Korea*
[t] *National Taiwan University, Taipei,10764, Taiwan, R.O.C.*